University of Sussex

An atomchip gyro

Theory and experiment

Jean-Marc MARTIN

Submitted for the degree of Doctor of Philosophy

University of Sussex

October 2019

Declaration

I hereby declare that this thesis has not been and will not be submitted in whole or in part to another University for the award of any other degree.

Signature:

Jean-Marc MARTIN

UNIVERSITY OF SUSSEX

Jean-Marc MARTIN, Doctor of Philosophy

An atomchip gyro: theory and experiment

Summary

In the context of the second quantum revolution, the field of quantum sensors is in full expansion. One of the corner stones of this field is inertial sensing through cold-atom interferometry which provides sensors of high precision and stability. Size reduction is one of the main tasks in order to develop atomic inertial sensors that could apply to inertial navigation: this leads to the development of atom-chips. It is with this context in mind that this thesis investigates an atom-chip gyro in a collaboration between the University of Sussex and l'Observatoire de Paris (France). The experimental work is hosted at l'Observatoire de Paris where we worked on atom-chip fabrication, comparing metal deposition by evaporation and by electroplating, and paying attention on the wire's roughness as it impacts on the magnetic waveguide and therefore the atoms. But the wire's roughness is only one source of noise to the magnetic waveguide. Low noise current supplies are also studied and characterised. Furthermore, using the density operator and coherent state basis we develop a simple and elegant formalism under a 1D approximation. We use a new approach to show how temperature influences the propagation of a wavepacket by increasing the spatial spreading while decreasing the wavepacket coherence. We also built a model for the pumping dynamics of a cold-atom experiment in a single vacuum chamber which matches experimental data from l'Observatoire de Paris and is an important step to work on size and the dead time reduction of sensors. All these different steps present in this thesis take us towards a working inertial sensor. While working on noise characterisation which will always remain a fundamental issue in building an inertial sensor, this thesis presents new models and approaches that may benefit the development of quantum technologies.

Acknowledgements

It is an unique experience to achieve a PhD thesis. An experience that I do not regret at all, it improved me professionally and scientifically.

Therefore I want to acknowledge Prof. Barry M. Garraway and Dr. Carlos L. Garrido Alzar, for allowing me to work on this thesis and want to thank them for helping me to grow professionally and scientifically. Also, the experimental part of this thesis would have not been possible without all the people I worked with at l'Observatoire de Paris. William Dubosclard, Seungjin Kim, Marc-Antoine Buchet and Satyanarayana Bade who worked with me on the GyrAChip. I would also like to give special thanks to Konstantin Ott who helped way more than he can imagine by discussing with me of his electrodeposition for the atom-chip used in TACC. Members of the clean room: Faouzi Boussaha, Christine Chaumont, Josiane Firminy and Florent Reix. Members of MUTA: David Holleville and Bertrand Venon. Members of the electronics services in SYRTE: José Pinto and Michel LOURS. And of course, the members of the scientific team Atom Interferometry and Inertial Sensors. I would also like to give special thanks to Andrew Elbourn for his proof reading but also for his discussions on interference in ring traps. As well as Jesus Rubio Jimenez through his discussion on density matrices, Pierre-Henry Hanzard for the several discussion and the support. And far more others, at the University of Sussex and l'Observatoire de Paris, who are victims of my poor memory for names.

I would also like to thank all the people I met during my studies who led me to this PhD. Research team I have done internships in: the members of teams OIA (and SAI) from LPL at l'Université Paris 13, and particularly Paolo Pedri from the LPL who have been a source of good advice, the members of the team GFAL in Universidade Federal da Paraiba, Martine Chevrollier and Marcos Oriá who introduced me to atomic physics. Teachers who have impacted my studies course to who I am

grateful: Sara Ducci, Yann Gallais, Eric Carpentier and particularly Jean-François Bange.

Jean-François Bange have marked generations of students and will be remembered by them.

Even small things can have important outcomes, this is the logic of the butterfly effect. Therefore, I would also like to thank people who have not been small things and have played role in this outcome. My friends: Miguel, Bastien, Tristan, Ramon, Marion, David, Camille, José, Ivan, Jérémy, Dimitri, Audrey et Odette. The members of the Integrated Martial Arts club at Sussex.

And finally, to my parents and my family.

Contents

List of Tables

List of Figures

Chapter 1

Introduction

"We are currently in the midst of a second quantum revolution. The first quantum revolution gave us new rules that govern physical reality. The second quantum revolution will take these rules and use them to develop new technologies." This is a famous phrase in the abstract of *Quantum technology: the second quantum revolution* an article by Jonathan P. Dowling & al in 2003 [1]. In 2014 the UK Quantum Technology hubs were established and a few years after in May 2016 the Quantum Manifesto was published [2], a call to launch Europe's initiative in quantum technologies. Indeed the second quantum revolution is upon us, and it is in the context of a dynamic and effervescent European quantum community that this PhD thesis started (in November 2015). One of the main interests in quantum technology, and in this PhD thesis, is quantum sensing [3]. Within the vast, exciting and growing field of quantum sensing, this work focuses on inertial sensing using cold atom interferometry, and more specifically the atom-chip based atomic gyroscope. Gyroscopes, also referred to as just gyros, can be applied in geophysical studies and fundamental tests of physics like the geodetic effect. However, since the first gyro application with Anschutz's gyrocompass in 1906 [4], gyros had one major application, namely navigation. This is indeed the purpose of this study, to work towards a quantum gyroscope through cold atom interferometry on atom-chips with application to inertial navigation and was done in a collaboration between the Observatoire de Paris and the University of Sussex.

1.1 Gyroscopes and Sagnac effect

Gyros cover three applications, gyrocompass determining the earth's rotational axis and gyroscopes determining both the angular position (relatively to the gyroscope's angular momentum) and the angular velocity (where a distinction is made in French as a "*gyromètre*" gives the angular speed [5]). There are two types of gyroscope, mechanical gyroscopes and Sagnac effect gyroscopes. Mechanical gyroscopes are either based on spinning wheels and conservations of angular momentum, or based on vibrating structures and Coriolis effects. Coriolis vibrating gyroscopes [6] mainly take the form of microelectromechanical Systems (MEMS) and are found in everyday instruments such as smartphones. We will, however, be focusing on Sagnac effect [7] gyroscopes. Based on wave mechanics, they benefit from the incredible precision achievable through interferometry. There are two types of gyroscope that use the Sagnac effect: optical gyroscopes and atomic gyroscopes.

Over a century after George Sagnac's experiment, the Sagnac effect is today widely applied in gyroscope to measure an angular velocity Ω [8]. In the Sagnac effect, two coherent waves, conter-propagating in an enclosed area A will build a phase difference ϕ_{Sagnac} due to the rotation of the different paths, as you can see in Fig. 1.1. We can write the following relation between the phase difference ϕ_{Sagnac} and Ω:

$$\phi_{\text{Sagnac}} = \frac{4\pi E}{hc^2}\vec{A}.\vec{\Omega}, \tag{1.1}$$

where E is the energy of the particle, $E = h\nu$ for a photon of frequency ν and $E = mc^2$ for a particle of rest mass m.

With the rise of atomic matter-wave interferometry in the 1990s [9, 10, 11], Sagnac effect with atomic matter-wave was first demonstrated in Ref. [12]. This first demonstration opened the path for more than 20 years of development in atomic Sagnac interferometers [13]. The biggest interest of using atomic matter-waves rely on E from Eq. (1.1), indeed if we compare the phase difference generated by an optical photon to the phase difference generated by an atomic matter-wave, we see that for a same area A the phase difference generated by the atomic Sagnac interferometer will be $\simeq 10^{11}$ times higher. Therefore, for a same sensitivity to a rotation velocity, atomic gyroscopes allow for more compact setups in contrast to optical gyroscopes.

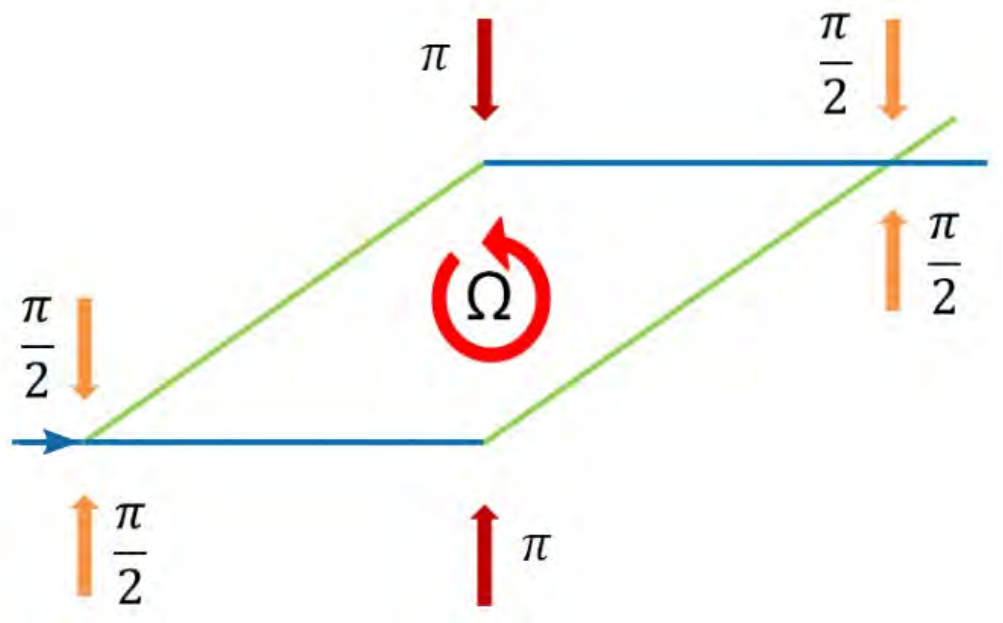

Figure 1.1: Schematic of a Sagnac interferometer in a Mach-Zender configuration. The atoms come from the left (blue arrow), and is split into two clouds by a $\pi/2$ pulse (50/50 beam splitter pulse). The two clouds, with different momenta, will follow different paths (colored lines, colors illustrate different momenta). A π-pulse (mirror pulse) will then change the clouds momenta, their paths will then form a sensing area A, sensitive to an angular velocity $\vec{\mathbf{\Omega}}$ which is perpendicular to the area A. A second $\pi/2$-pulse will act as a second beam splitter, mixing the clouds for an interference pattern. The interference will been seen in terms of population ratio of the two clouds after the second $\pi/2$ pulse. The Sagnac phase shift in Eq. (1.1) will give a population ratio different to the expected 50/50 beam splitter.

Moreover, in Ref. [13], it is shown that within Sagnac atomic interferometers, it is the experiment based on cold atoms which show the best predisposition to compactness. Therefore cold atom gyroscopes are suitable for our project to create an atomic inertial sensor, but further investigation into size efficiencies are required. For instance, the SYRTE's gyrometer setup (at l'Observatoire de Paris) [13, 14] uses an atomic fountain not compatible with our compact sensor, since it adds considerable length through free fall motion of the clouds.

1.2 Towards the use of waveguides

Beside our goal to achieve a portable navigation device, gyroscopes need to be as compact as possible in order to reduce systematic error. Indeed, in addition to being sensitive, a gyroscope needs to be accurate. By reducing the size of the gyroscope, we reduce systematic phase shifts due to stray fields and mechanical vibrations.

However, according to Eq. (1.1) the Sagnac phase shift ϕ_{Sagnac}, which determine the sensitivity of the gyroscopes, is proportional to the sensing area A. Therefore reducing the size of the device, which generally leads to reducing the sensing area, leads to a reduction the device's sensitivity. However, there is margin to reduce an atomic gyroscope size without reducing the sensing area by just addressing the interferometer configuration. For example, the gyroscope at SYRTE, with a fountain configuration, presents a surface area of 11 cm^2 for a height (between the Raman beams) of 59 cm [14], which translates to a geometry with a high perimeter length for a given area. We can then address the size reduction of atomic gyroscope reducing the perimeter of the sensing area. It is then natural to aim for a circular configuration of the atomic interferometer as it is the geometry that minimizes the perimeter for a given area. The use of a magnetic atom waveguide then becomes the obvious solution in order to manipulate the atoms through a circular path. Furthermore, while using waveguides, we can partially compensate a physical reduction of the sensing area by making the atoms go through multiples revolutions, virtually increasing the effective sensing area as it is done for Fibre Optic Gyroscope (FOG) [15]. Moreover, a waveguide would allow us to obtain longer interrogation times than atomic fountains which are limited by free fall paths. The interrogation time would then be determined by the initial kick transferred to the atoms. It would also give us a better interferometric contrast due to low velocity scattering of the guided cold atoms.

Several works in the cold atom field are aiming towards the production of circular waveguides (i.e. ring/toroidal traps). We can note three major techniques to produce them: magnetic traps [16, 17, 18], optical potentials [19, 20, 21, 22], and Radio-Frequency (RF) dressing potentials [23, 24, 25, 26, 27, 28]. Between those three techniques, RF dressing potentials are well adapted to atom-chip technology and miniaturisation.

1.3 An atom-chip gyro

This thesis is a collaboration project between the University of Sussex and SYRTE (at l'Observatoire de Paris) with the ambition to work, by both theory and experiment, towards the realisation of an atom-chip gyroscope compatible for inertial navigation. Atomic inertial sensors have the hope to revolutionise the precision of inertial measurements in the same way that atom-clocks have revolutionised time measurement. There is, however, a huge obstacle to over-come before such a revolution: the miniaturisation of atomic sensors. It is by addressing the miniaturisation of cold atom experiments that devices such as atom-chips have been intensively pursued. Twenty years after the demonstration of the first atom-chips [29] by Jakob Reichel, atom-chip have spread and grown in the field of cold atoms, both in terms of technological devices and fundamental physics [30]. Atom-chips have even reached space, in the International Space Station, where NASA's Cold Atom Lab (CAL) is performing cold atom experiments using atom-chips [31]. Furthermore, with regards to technical applications in vehicles, atom-chips show that they are robust and can operate through important stresses. For example a Bose-Einstein Condensate (BEC) was realized and used to perform atomic interferometry with an atom-chip in a sounding rocket: the MAIUS project [32].

In our specific case, an "atom-chip" experiment for rotation sensing was demonstrated in Ref. [33] by Mara Prentiss' team. Their "atom-chip" is made using wires and permalloy foils of mm scale, such devices are often called mesoscopic atom-chips [34] as they are not produced by microfabrication processes. Mara Prentiss' team demonstrated a moving linear guide based atom interferometer with an '8 loop' shaped sensing area of 0.2 mm^2. Unfortunately their device showed a standard deviation of the phase readout $\simeq 0.4$ rad. There is still a long way to go to before achieving a working atom-chip gyro used in inertial navigation.

An ongoing experimental project, GyrAChip, aims to develop a **Gyr**oscope on an **A**tom-**Chip**. It is with this project, hosted by SYRTE, that the University of Sussex have collaborated for the work presented in this thesis. The project is built on a design proposal for a GyrAChip [35, 36], capable of reaching a sensitivity of the order of 10^{-7} rad $\cdot\, \mathrm{s}^{-1}/\sqrt{\mathrm{Hz}}$. The proposal considers the realization of a microwire pattern using three wires in a circular geometry capable of creating a circular non-

dissipative magnetic guide as you can see in Fig. 1.2. With a radius of 500 μm for the central wire, the parallel outer wires have a 13 μm separation from the central wire. The outer wires provide a bias magnetic field with a current of -123 mA whereas the central wire has a current of 121 mA, this pattern would generate a confining potential for the atoms. This potential would confine atoms 13 μm above the chip substrate. These currents would be modulated, reducing the induced decoherence during the propagation of the cloud due to the roughness of the wires [37].

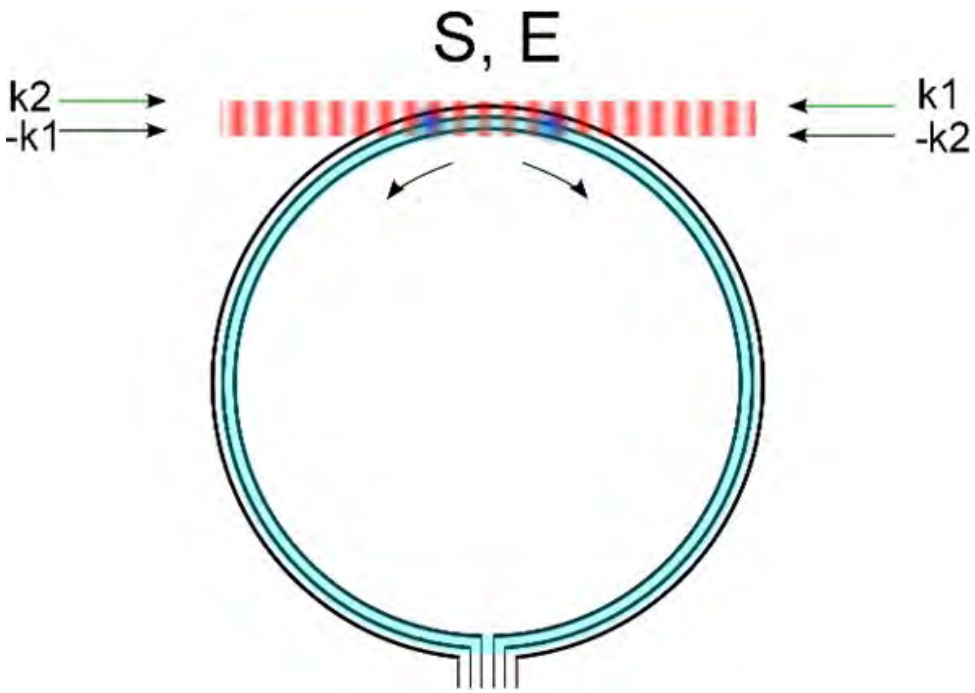

Figure 1.2: Three wire design (for a GyrAChip prototype, taken from [36]) in order to create a circular waveguide (light blue). The entry point E and the exit point S are physically at the same point. The effect of the matter-wave beam splitter is represented by the wavevectors $\mathbf{k_1}$ and $\mathbf{k_2}$.

In this ring waveguide, a cold atom cloud of N atoms would be split at the point E (entry) (Fig. 1.2), by Bragg or Raman beam splitters, into two clouds propagating in opposite directions. After a time $2T$ (which depends on the launch velocity) the two clouds reach the exit point S, located at the same place of the ring as E (Fig. 1.2), where another beam splitter is applied. The outcome of the interferometer would be two conter-propagating clouds, with a probability $P_{\pm}$ for a atom to be in one of those clouds, plus a static cloud, with a probability P_0 for the atoms to be in this

cloud, written as follows:

$$P_{\pm} = \frac{1}{2}[1 - \eta \cos(\phi_{Sagnac} + \phi)], \tag{1.2}$$

$$P_0 = \frac{1}{2}[1 + \eta \cos(\phi_{Sagnac} + \phi)], \tag{1.3}$$

where η is the contrast of the interferometer and ϕ is an additional phase which would arise from the experimental parameters as is discussed in Ref. [38]. After a time smaller than T the population difference between the clouds is measured, carrying a signature of the rotation Ω through ϕ_{Sagnac} as showed in Eq. 1.3.

There is still a lot of work in this thesis before the first rotation measurement with a GyrAChip will be made. For example, there is a discussion on the use of thermal atom clouds instead of BECs, on how they would propagate in a ring waveguide and if we would be able to use them for inertial sensing. We then address in Chapter 2 the effect of temperature on a wavepacket propagation. We address in Chapter 3 the effect of temperature on the interference fringes. Moreover, a GyrAChip with a wire pattern for a *ring* waveguide is still to be manufactured. Therefore atom-chip fabrication at l'Observatoire de Paris is presented in Chapter 4 where we focus on how to build thick wires with the smallest surface roughness possible. The aspect of the current noise is also addressed in Chapter 5 where we study low noise current generators. And finally, the vacuum system is also addressed in Chapter 6 in order to study the question of an atomic sensor dead-time, due to the loading of atoms in traps. The work presented in Chapter 6 was published in Ref. [39] in July 2019.

Chapter 2

Thermal wavepacket

In the previous chapter, we have presented the idea of using atom-chip based gyrometers for inertial navigation by generating waveguides in form of a 500 μm radius ring. However, there is a major concern as to how atoms will spread on such scales, knowing that atoms in ring waveguides tends to spread and occupy all the ring [22, 28, 17]. A key question is: what are the required conditions for an atom, represented by wavepacket, to do one or more turns in the ring waveguide, while, still being able to produce interference fringes?

There are, of course, different parameters to take into account such as the launching speed, the size of the ring, the matter-wave properties and so on; most of these parameters have already been studied [38]. One parameters that is of interest to us is the temperature and its effect on the propagation of atoms. With this purpose in mind, we will study the propagation of a 1D free wavepacket as an approximation of the ring waveguide, which can be considered as a 2D trap in the radial direction and a 1D free space on the azimuthal direction. Our approach is to use the formalism of density operators with the Glauber-Sudarshan P-representation, where we can write the phase-space thermal distribution of our quantum system in the coherent state basis. This would then be equivalent to consider our density operator as a mixed state, a superposition, of coherent wavepackets $\psi_\alpha(x,t)$:

$$\begin{aligned}\rho_{\bar{n}}(x,x',t) &= \langle x|\hat{\rho}_{\bar{n}}|x'\rangle \\ &= \iint \mathcal{P}(\alpha)\,\langle x|\alpha\rangle\,\langle\alpha|x'\rangle\,\mathrm{d}^2\alpha \\ &= \iint \mathcal{P}(\alpha)\psi_\alpha(x,t)\psi^\dagger_\alpha(x',t)\,\mathrm{d}^2\alpha \end{aligned} \tag{2.1}$$

With $|\alpha\rangle$ being the coherent state, α being the eigenvalue of $|\alpha\rangle$ and $\mathcal{P}(\alpha)$ being the Glauber-Sudarshan P-function, defined as follows (Appendix A):

$$\mathcal{P}(\alpha) = \frac{1}{\pi\bar{n}}\exp\left(-\frac{|\alpha|^2}{\bar{n}}\right). \tag{2.2}$$

Where $\bar{n}$ is the expected value of the number operator, $\bar{n}$ contains the temperature information according to the following formula:

$$\bar{n} = \frac{1}{\exp\left(\frac{\hbar\omega}{k_\mathrm{B}T}\right) - 1}. \tag{2.3}$$

From this, we will first consider a pure-state wavepacket and calculate its density operator. This calculation will be followed by the calculation of the density operator of a mixed state: a superposition of coherent wavepackets with a $\mathcal{P}(\alpha)$ distribution.

2.1 The pure-state density operator

Before applying the P-function we will study our system as a pure state: a Gaussian solution to the 1D free space Schrödinger equation, ψ_0. Therefore, let's take a look at a Gaussian wavepacket ψ_0 for an atom of mass m, initially positioned at $x_0 = 0$ and with an initial momentum $\hbar k_0$. The initial momentum spread, Δk, is defined as the Gaussian variance in the momentum space. Therefore we have for ψ_0 (from Appendix B):

$$\begin{aligned}\psi_0(x,t) =& \left(\sqrt{2\pi}\,\Delta x(t)\right)^{-1/2}\exp\left[-\frac{(x-v_0t)^2}{4\Delta x(t)^2}\right] \\ &\times\exp\left[i\frac{v_\Delta t}{\Delta x(0)}\frac{(x-v_0t)^2}{4\Delta x(t)^2} + i(k_0x-\omega_0t) - \frac{i}{2}\cos^{-1}\left(\frac{1}{2\Delta x(t)\Delta k}\right)\right]\end{aligned} \tag{2.4}$$

Where we define the following quantities:

$$\omega_0 = \frac{\hbar k_0^2}{2m} \qquad v_0 = \frac{\hbar k_0}{m} \tag{2.5}$$

$$v_\Delta = \frac{\hbar \Delta k}{m} \qquad \Delta x(t=0) = \frac{1}{2\Delta k} \tag{2.6}$$

$$\Delta x(t)^2 = \Delta x(0)^2 + (v_\Delta t)^2 \tag{2.7}$$

Therefore the density operator for a pure state 1D free propagating wavepacket is:

$$\rho_0(x, x', t) = \langle x | \, |\psi_0\rangle\langle\psi_0| \, | x' \rangle \tag{2.8}$$

$$= \psi_0(x,t) \times \psi_0^\dagger(x',t) \tag{2.9}$$

$$= \frac{1}{\sqrt{2\pi}\,\Delta x(t)} \exp\left[-\frac{(x - v_0 t)^2 + (x' - v_0 t)^2}{4\Delta x(t)^2} \right] \times \exp\left[i k_0 (x - x') + \frac{i v_\Delta t}{4\Delta x(t)^2 \Delta x(0)} \left([x - v_0 t]^2 - [x' - v_0 t]^2 \right) \right] \tag{2.10}$$

$$= \frac{1}{\sqrt{2\pi}\,\Delta x(t)} \exp\left[-\frac{([x - v_0 t] + [x' - v_0 t])^2}{8\Delta x(t)^2} \right] \times \exp\left[-\frac{([x - v_0 t] - [x' - v_0 t])^2}{8\Delta x(t)^2} \right] \times \exp[i k_0 ([x - v_0 t] - [x' - v_0 t])] \times \exp\left[2i \frac{v_\Delta t}{\Delta x(0)} \frac{([x - v_0 t] + [x' - v_0 t])([x - v_0 t] - [x' - v_0 t])}{8\Delta x(t)^2} \right] \tag{2.11}$$

We can then plot $\hat{\rho_0}$ and see the propagation of a pure-state wavepacket in a (x, x') space which represents the density matrix elements in a spatial basis. The real physical 1D space is then the diagonal of the density matrix, when $x = x'$. Using Eq. (2.11) we can plot $|\rho_0(x, x', t)|$ and $\arg(\rho_0(x, x', t))$, in Fig. 2.1, as they are directly expressed. Let us note that when $x = x'$, we have $\rho_0(x, x, t) = |\psi_0(x, t)|^2$, we can then directly see the probability density as a Gaussian distribution. Also, $|\rho_0(x, x', t)|$ in Fig. 2.1 appear as a perfectly symmetric 2D Guassian, which can also be seen in Eq. (2.11). The parameter used in Fig. 2.1 can be seen in Table. 2.1 using the data present in Ref. [40] for the D_2 optical transition of ^{87}Rb.

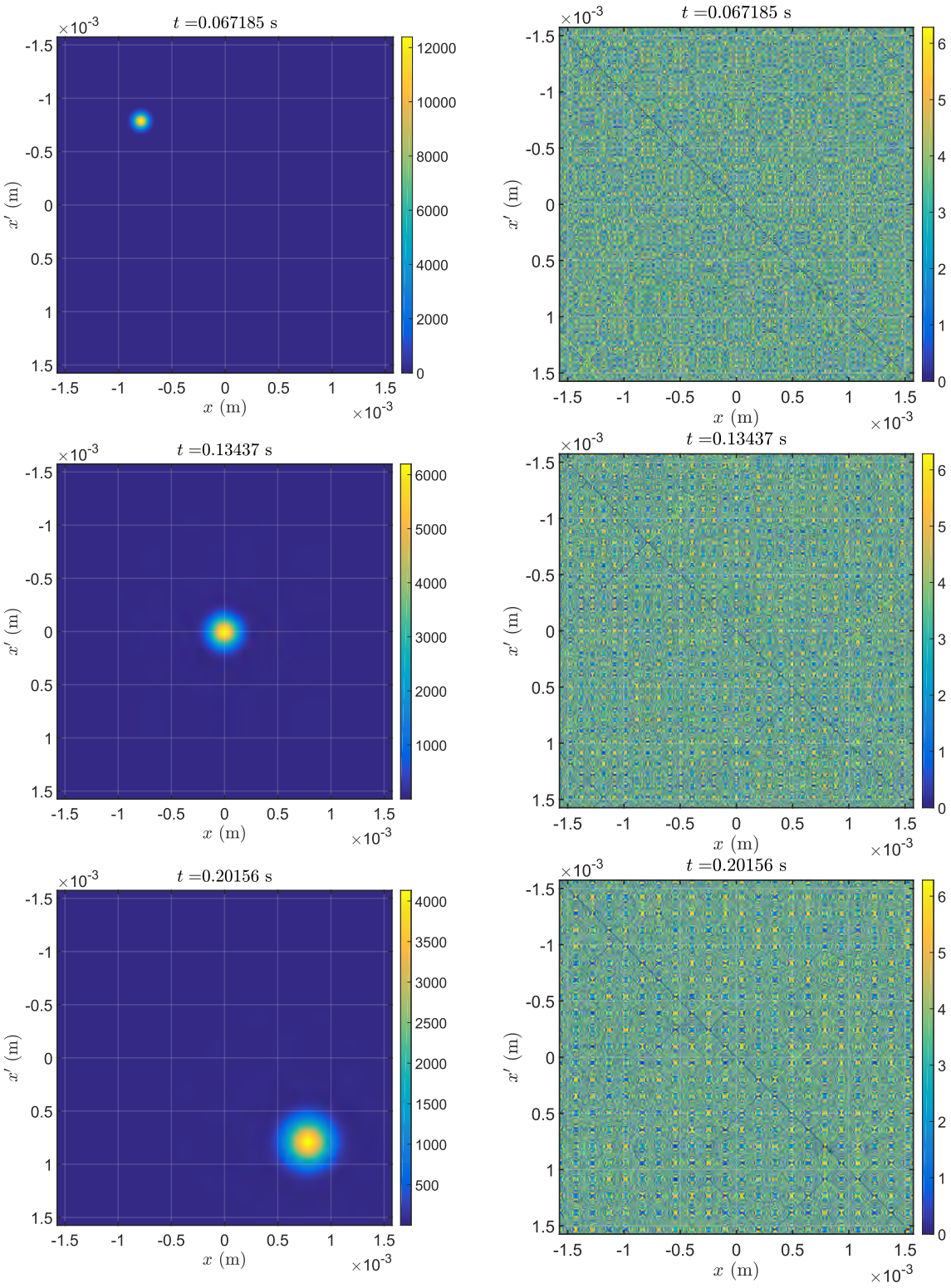

Figure 2.1: Plot of $\rho_0(x, x', t)$ at three different times. Left column, plots of $|\rho_0(x, x', t)|$, we see a 2D Gaussian propagating on the diagonal and spreading on (x, x'). Right Column, plots of $\arg(\rho_0(x, x', t))$, we can see nodes of values $(0, \pi, 2\pi)$ increasing in size as t increase. Let us note that on the diagonal $(x = x')$, $\arg(\rho_0(x, x', t)) = 0$.

Our parameter	Value used	Reference
v_0	$2v_\mathrm{r} = 2 \times 5.8845 \times 10^{-3}$ m $\cdot$ s^{-1}	[40]
ω	$2\pi \times 100$ Hz	arbitrary
m	$1.44316060 \times 10^{-25}$ Kg	[40]
$\hbar$	1.054571×10^{-34} J $\cdot$ s	[40]
k_B	1.380650×10^{-23} J $\cdot$ K^{-1}	[40]

Table 2.1: Table of parameters used in Fig. 2.1 for the D_2 optical transition of ^{87}Rb.

The formalism used to present $\rho_0(x, x', t)$ was specifically chosen as it will be useful to see intuitively the impact of temperature on a propagating wavepacket, as well as, making the calculation relatively straight-forward. In this formalism, we can separate $\rho_0(x, x', t)$ into different terms with a direct physical meaning:

$$\mathrm{N}_0(t) = \frac{1}{\sqrt{2\pi}\Delta x(t)}, \tag{2.12}$$

$$\mathrm{G}_0^+(x, x', t) = \exp\left[-\frac{([x - v_0 t] + [x' - v_0 t])^2}{8\Delta x(t)^2}\right], \tag{2.13}$$

$$\mathrm{G}_0^-(x, x', t) = \exp\left[-\frac{([x - v_0 t] - [x' - v_0 t])^2}{8\Delta x(t)^2}\right], \tag{2.14}$$

$$\begin{aligned}\phi_0(x, x', t) =& k_0([x - v_0 t] - [x' - v_0 t]) \\ &+ 2\frac{v_\Delta t}{\Delta x(0)} \frac{([x - v_0 t] + [x' - v_0 t])([x - v_0 t] - [x' - v_0 t])}{8\Delta x(t)^2}.\end{aligned} \tag{2.15}$$

These terms are: the normalisation factor $\mathrm{N}_0(t)$, the diagonal Gaussian $\mathrm{G}_0^+(x, x', t)$, the anti-diagonal Gaussian $\mathrm{G}_0^-(x, x', t)$ and the phase $\phi_0(x, x', t)$. We can then write $\rho_0(x, x', t)$, using these terms as follows:

$$\boxed{\rho_0(x, x', t) = \mathrm{N}_0(t)\mathrm{G}_0^+(x, x', t)\mathrm{G}_0^-(x, x', t)\exp(i\phi_0(x, x', t))}. \tag{2.16}$$

2.2 A mixed state: superpositions of coherent wavepackets

Let us remind that our approach is to simplify the study of atoms propagating in a waveguide by the propagation of a single wavepacket in a 1D free space. However, instants before atoms are freed in the waveguide (at $t = 0$), they are trapped (and cooled) in a standard 3D harmonic potential. The harmonic potential will not only determine the initial conditions of the wavepacket but also the coherent states basis. Indeed, if we define ω as the initial harmonic potential frequency (not to be confused with ω_0 from Eq. (2.4)), then we can link $\{\hat{a}^\dagger, \hat{a}\}$ to $\{\hat{x}, \hat{p}\}$ as follows:

$$\hat{a} \equiv \sqrt{\frac{1}{2m\omega\hbar}}\,(m\omega\hat{x} + i\hat{p}) \qquad \hat{a}^\dagger \equiv \sqrt{\frac{1}{2m\omega\hbar}}\,(m\omega\hat{x} - i\hat{p})\,, \tag{2.17}$$

Therefore, giving new definition to the position and momentum operators:

$$\hat{x} = \sqrt{\frac{\hbar}{2m\omega}}\left(\hat{a} + \hat{a}^\dagger\right) \qquad \hat{p} = -i\sqrt{\frac{m\omega\hbar}{2}}\left(\hat{a} - \hat{a}^\dagger\right). \tag{2.18}$$

Now, we can link the quantities $\{x_\alpha, k_\alpha\}$ to $\{\alpha_{Re}, \alpha_{Im}\}$ to the expressions $x_\alpha = \langle\hat{x}\rangle_\alpha$ and $\hbar k_\alpha = \langle\hat{p}\rangle_\alpha$ using $\alpha_{Re} = \mathrm{Re}\{\alpha\}$ and $\alpha_{Im} = \mathrm{Im}\{\alpha\}$, as follows:

$$x_\alpha = \langle\alpha|\hat{x}|\alpha\rangle = \sqrt{\frac{\hbar}{2m\omega}}\,(\alpha + \alpha^*) = \sqrt{\frac{2\hbar}{m\omega}} \times \alpha_{Re}, \tag{2.19}$$

and

$$\hbar k_\alpha = \langle\alpha|\hat{p}|\alpha\rangle = -i\sqrt{\frac{m\omega\hbar}{2}}\,(\alpha - \alpha^*) = \hbar\sqrt{\frac{2m\omega}{\hbar}} \times \alpha_{Im}. \tag{2.20}$$

Let us now introduce now the harmonic trap length a_{ho}:

$$a_{\mathrm{ho}} = \sqrt{\frac{\hbar}{m\omega}}. \tag{2.21}$$

Therefore, since we are considering our atoms to be trapped in an harmonic potential before they start propagating in the waveguide (simplified as a 1D free space), at $t = 0$, then the initial spreading $\Delta x(t = 0)$ of our 1D wavepacket is determined by the harmonic trap length a_{ho} as follow[41]:

$$\Delta x(t = 0) = \frac{a_{\mathrm{ho}}}{\sqrt{2}}. \tag{2.22}$$

Therefore we can re-write the quantities presents in Eq. (2.4) as:

$$\frac{v_\Delta t}{\Delta x(0)} = \omega t, \qquad \Delta x(t)^2 = \frac{a_{\text{ho}}^2}{2}\left(1 + [\omega t]^2\right). \tag{2.23}$$

And $\{x_\alpha, k_\alpha\}$ from Eq. (2.19) and Eq. (2.20) as:

$$x_\alpha = \sqrt{2} a_{\text{ho}} \alpha_{\text{Re}}, \qquad k_\alpha = \frac{\sqrt{2}}{a_{\text{ho}}} \alpha_{\text{Im}}. \tag{2.24}$$

Therefore, by linking $\left\{\hat{a}, \hat{a}^\dagger\right\}$ to $\{\hat{x}, \hat{p}\}$ we are writing our wavepacket in a coherent state basis, then converting it back to spatial basis through the coherent wavepacket $\psi_\alpha(x,t)$:

$$\begin{aligned}\psi_\alpha(x,t) = &\left(\sqrt{2\pi}\Delta x(t)\right)^{-1/2} \exp\left[-\frac{\left([x - v_0 t] - [x_\alpha + v_\alpha t]\right)^2}{4\Delta x(t)^2}\right] \\ &\times \exp[i[k_0 + k_\alpha][x - x_\alpha] - i\omega_{0+\alpha} t] \\ &\times \exp\left[i\frac{v_\Delta t}{\Delta x(0)}\frac{\left([x - v_0 t] - [x_\alpha + v_\alpha t]\right)^2}{4\Delta x(t)^2} - \frac{i}{2}\cos^{-1}\left(\frac{1}{2\Delta x(t)\Delta k}\right)\right],\end{aligned} \tag{2.25}$$

where $\omega_{0+\alpha} = \hbar(k_0 + k_\alpha)^2/(2m)$, $v_\alpha = \hbar k_\alpha / m$ and $\mathrm{d}^2\alpha = \mathrm{d}\alpha_{\text{Re}}\,\mathrm{d}\alpha_{\text{Im}} = \mathrm{d}x_\alpha\,\mathrm{d}k_\alpha\,/2$.

Then, the idea here, is to represent $\psi_\alpha(x,t)$ as a solution of the 1D free space Schrödinger equation, as much as ψ_0, both represented in a phase-space representation as you can see in Fig. 2.2. In this representation, ψ_0 is just a point (red point in Fig. 2.2) of coordinates $\{x_0, k_0\}$, therefore ψ_α is the point of coordinate $\{x_0 + x_\alpha, k_0 + k_\alpha\}$ (blue point in Fig. 2.2). Following this idea, we can represent Eq. (2.1) in Fig. 2.2 as a sum of all the blue points (centered on around the red point) with a distribution $\mathcal{P}(\alpha)$. By doing so, we go from the density operator $\hat{\rho}_0$ of a pure-state, represented by the red point (in Fig. 2.2), to the density operator $\hat{\rho}_{\bar{n}}$ of a mixed-state. The temperature information in this mixed-state density operator is then carried by $\bar{n}$ through the action of $\mathcal{P}(\alpha)$ working as a distribution function. Therefore, starting from Eq. (2.1) we can calculate $\psi_\alpha(x,t)\psi_\alpha^\dagger(x',t)$:

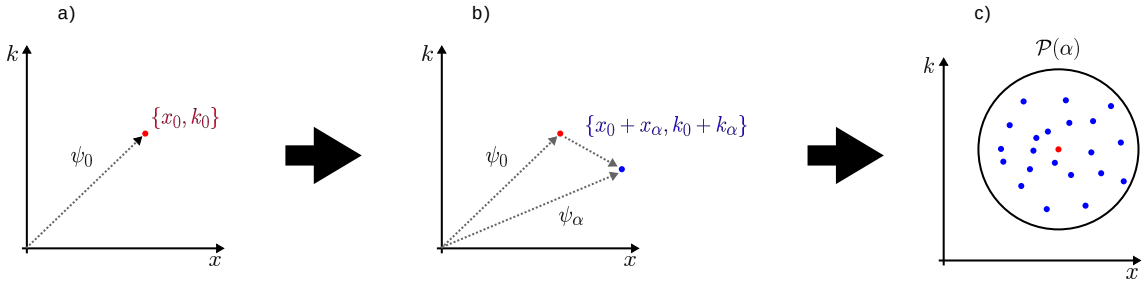

Figure 2.2: Phase-space representation. From left to right: (a), the red point represents ψ_0, (b), from ψ_0 we represent the coherent wavepacket ψ_α as a blue point, (c), we then represent a thermal mixed state as a sum of all the blue point centered in the red point with a $\mathcal{P}(\alpha)$ distribution.

$$
\begin{aligned}
&\psi_\alpha(x,t)\psi_\alpha^\dagger(x',t) = \\
&\quad \left(\sqrt{2\pi}\Delta x(t)\right)^{-1} \exp\left[-\frac{\left([x-v_0t]-[x_\alpha+v_\alpha t]\right)^2}{4\Delta x(t)^2}\right] \\
&\quad \times \exp\left[-\frac{\left([x'-v_0t]-[x_\alpha+v_\alpha t]\right)^2}{4\Delta x(t)^2}\right] \\
&\quad \times \exp[i(k_0+k_\alpha)(x-x_\alpha) - i\omega_{0+\alpha}t - i(k_0+k_\alpha)(x'-x_\alpha) + i\omega_{0+\alpha}t] \\
&\quad \times \exp\left[i\frac{v_\Delta t}{\Delta x(0)}\frac{\left([x-v_0t]-[x_\alpha+v_\alpha t]\right)^2}{4\Delta x(t)^2} - i\frac{v_\Delta t}{\Delta x(0)}\frac{\left([x'-v_0t]-[x_\alpha+v_\alpha t]\right)^2}{4\Delta x(t)^2}\right] \\
&\quad \times \exp\left[-\frac{i}{2}\cos^{-1}\left(\frac{1}{2\Delta x(t)\Delta k}\right) + \frac{i}{2}\cos^{-1}\left(\frac{1}{2\Delta x(t)\Delta k}\right)\right]
\end{aligned}
\tag{2.26}
$$

$$
\begin{aligned}
&= \left(\sqrt{2\pi}\Delta x(t)\right)^{-1} \exp\left[-\frac{\left([x-v_0t]-[x_\alpha+v_\alpha t]\right)^2}{4\Delta x(t)^2}\right] \\
&\quad \times \exp\left[-\frac{\left([x'-v_0t]-[x_\alpha+v_\alpha t]\right)^2}{4\Delta x(t)^2}\right] \\
&\quad \times \exp[i(k_0+k_\alpha)(x-x')] \\
&\quad \times \exp\left[i\frac{v_\Delta t}{\Delta x(0)}\left(\frac{\left([x-v_0t]-[x_\alpha+v_\alpha t]\right)^2}{4\Delta x(t)^2} - \frac{\left([x'-v_0t]-[x_\alpha+v_\alpha t]\right)^2}{4\Delta x(t)^2}\right)\right].
\end{aligned}
\tag{2.27}
$$

Since the integration in Eq. (2.1) is done over $\{x_\alpha, k_\alpha\}$ we can separate out the terms that are independent of these. By doing so, we recognize $\rho_0(x,x',t)$ from Eq (2.16) multiplied by the terms that hold the temperature information. Therefore using Eq (2.2) we can write:

$$
\begin{aligned}
\rho_{\bar{n}}(x,x',t) =& \rho_0(x,x',t)\frac{1}{\pi\bar{n}} \\
&\times \iint \exp\left[-\frac{x_\alpha^2}{2\bar{n}a_{\mathrm{ho}}^2}\right]\exp\left[-\frac{a_{\mathrm{ho}}^2k_\alpha^2}{2\bar{n}}\right]\exp[ik_\alpha(x-x')] \\
&\quad\times\exp\left[\frac{-1}{4\Delta x(t)^2}\Big(+2x_\alpha^2+4x_\alpha v_\alpha t+2v_\alpha^2t^2\right. \\
&\qquad\qquad -2x_\alpha[(x-v_0t)+(x'-v_0t)] \\
&\qquad\qquad \left.-2v_\alpha t[(x-v_0t)+(x'-v_0t)]\Big)\right] \\
&\quad\times\exp\left[\frac{v_\Delta t}{\Delta x(0)}\frac{i}{4\Delta x(t)^2}\Big(-2x_\alpha[(x-v_0t)-(x'-v_0t)]\right. \\
&\qquad\qquad \left.-2v_\alpha t[(x-v_0t)-(x'-v_0t)]\Big)\right]\frac{\mathrm{d}x_\alpha\,\mathrm{d}k_\alpha}{2}.
\end{aligned}
\tag{2.28}
$$

We observe that $\rho_{\bar{n}}(x,x',t)$ is written as $\rho_0(x,x',t)$ times a complex number. We identify this complex number to be a n-dimensional Gaussian integral with a linear term. This Gaussian integral can be solved in the following canonical form:

$$
\begin{aligned}
&\int \exp\left[\frac{-1}{2}\sum_{i,j}^{n}\mathbf{A}_{ij}z_iz_j+\sum_i \mathrm{B}_iz_i\right]\mathrm{d}^nz \\
&\qquad=\sqrt{\frac{(2\pi)^n}{\det[\mathbf{A}]}}\exp\left(\frac{1}{2}\vec{\mathbf{B}}^T\mathbf{A}^{-1}\vec{\mathbf{B}}\right) \qquad (2.29)\\
&\qquad=\sqrt{\frac{(2\pi)^n}{\det[\mathbf{A}]}}\exp\left(\frac{1}{2}\frac{1}{\det[\mathbf{A}]}\left(\mathrm{B}_1^2\mathrm{A}_{2,2}+\mathrm{B}_2^2\mathrm{A}_{1,1}-2\mathrm{B}_1\mathrm{B}_2\mathrm{A}_{1,2}\right)\right), \qquad (2.30)
\end{aligned}
$$

where we identify $z_1 = x_\alpha$, $z_2 = k_\alpha$ and $n = 2$. Meaning we can easily look for the matrix $\mathbf{A}$ and the vector $\vec{\mathbf{B}}$, and look to solve the integral on the coherent states.

2.2.1 The matrix A and vector $\vec{\mathbf{B}}$

Knowing that $v_\alpha = \hbar k_\alpha/m$, by identification, we can look at the coefficients for the x_α^2, k_α^2 and $x_\alpha k_\alpha$ terms in order to find the elements of the matrix $\mathbf{A}$.

For x_α^2 we see:

$$\begin{aligned}-\frac{1}{2}\mathrm{A}_{1,1} =& -\frac{1}{2\bar{n}a_{\mathrm{ho}}^2} - \frac{1}{2\Delta x(t)^2} \\ =& -\frac{1}{2}\frac{1}{a_{\mathrm{ho}}^2}\left(\frac{1}{\bar{n}} + \frac{a_{\mathrm{ho}}^2}{\Delta x(t)^2}\right),\end{aligned} \tag{2.31}$$

for k_α^2 we see:

$$\begin{aligned}-\frac{1}{2}\mathrm{A}_{2,2} =& -\frac{a_{\mathrm{ho}}^2}{2\bar{n}} - \frac{t^2}{2\Delta x(t)^2}\frac{\hbar^2}{m^2} \\ =& -\frac{1}{2}a_{\mathrm{ho}}^2\left(\frac{1}{\bar{n}} + [\omega t]^2\frac{a_{\mathrm{ho}}^2}{\Delta x(t)^2}\right),\end{aligned} \tag{2.32}$$

and for $x_\alpha k_\alpha$ we see:

$$\begin{aligned}-\frac{1}{2}\mathrm{A}_{1,2}\times 2 =& -\frac{\hbar t}{m\Delta x(t)^2} \\ =& -\frac{a_{\mathrm{ho}}^2}{\Delta x(t)^2}\omega t.\end{aligned} \tag{2.33}$$

This lead us to write the matrix $\mathbf{A}(t)$ in the following form:

$$\boxed{\mathbf{A}(t) = \begin{pmatrix} \frac{1}{a_{\mathrm{ho}}^2}\left(\frac{1}{\bar{n}} + \frac{a_{\mathrm{ho}}^2}{\Delta x(t)^2}\right) & \frac{a_{\mathrm{ho}}^2}{\Delta x(t)^2}\omega t \\ \frac{a_{\mathrm{ho}}^2}{\Delta x(t)^2}\omega t & a_{\mathrm{ho}}^2\left(\frac{1}{\bar{n}} + \frac{a_{\mathrm{ho}}^2}{\Delta x(t)^2}[\omega t]^2\right)\end{pmatrix}}. \tag{2.34}$$

Now we can look at the linear terms for the coefficients of x_α and k_α in order to find the elements for the vector $\vec{\mathbf{B}}$:

For x_α we see:

$$\begin{aligned}\mathrm{B}_1 =& \frac{1}{2\Delta x(t)^2}([x - v_0 t] + [x' - v_0 t]) - i\frac{v_\Delta t}{2\Delta x(t)^2\Delta x(0)}([x - v_0 t] - [x' - v_0 t]) \\ =& \frac{1}{2\Delta x(t)^2}([(x - v_0 t) + (x' - v_0 t)] - i\omega t[(x - v_0 t) - (x' - v_0 t)]),\end{aligned} \tag{2.35}$$

and for k_α we see:

$$\begin{aligned}\mathrm{B}_2 =& i(x - x') + \frac{\hbar t}{2m\Delta x(t)^2}([x - v_0 t] + [x' - v_0 t]) \\ & - i\frac{\hbar t}{2m\Delta x(t)^2\Delta x(0)}([x - v_0 t] - [x' - v_0 t]) \\ =& \frac{1}{2\Delta x(t)^2}\big(\omega t a_{\mathrm{ho}}^2[(x - v_0 t) + (x' - v_0 t)] + i a_{\mathrm{ho}}^2[(v_0 t) - (x' - v_0 t)]\big).\end{aligned} \tag{2.36}$$

We can, therefore, write the vector $\vec{\mathbf{B}}(x, x', t)$ in the following form:

$$\boxed{\vec{\mathbf{B}}(x, x', t) = \frac{1}{2\Delta x(t)^2}\begin{pmatrix} [(x - v_0 t) + (x' - v_0 t)] - i\omega t[(x - v_0 t) - (x' - v_0 t)] \\ a_{\mathrm{ho}}^2\omega t[(x - v_0 t) + (x' - v_0 t)] + i a_{\mathrm{ho}}^2[(x - v_0 t) - (x' - v_0 t)]\end{pmatrix}}. \tag{2.37}$$

Then, finally, using matrix $\mathbf{A}(t)$ and vector $\vec{\mathbf{B}}(x,x',t)$ we can write $\rho_{\bar{n}}(x,x',t)$ in the form of a pure state term multiplied and modified by a thermal term as follows:

$$\boxed{\rho_{\bar{n}}(x,x',t) = \rho_0(x,x',t) \times \frac{1}{\bar{n}\sqrt{\det[\mathbf{A}(t)]}} \exp\left[\frac{1}{2}\vec{\mathbf{B}}(x,x',t)^T \mathbf{A}(t)^{-1}\vec{\mathbf{B}}(x,x',t)\right]}. \tag{2.38}$$

Using Eq. (2.38) we can then plot the thermal wavepacket propagation, as you can see in Fig. 2.3 (using the parameters of Table 2.1), making the results comparable to Fig. 2.1. We clearly see a significant increase in the standard deviation on the diagonal axis and a reduction of the standard deviation on the anti-diagonal axis. This mean that we can clearly describe $\rho_{\bar{n}}(x,x',t)$ with a diagonal Gaussian and an anti-diagonal Gaussian, as in the formalism that we have selected for Eq. (2.16). Let us also note that the phase of $\rho_{\bar{n}}(x,x',t)$ is calculated by the function 'angle' function of Matlab, which uses the real and imaginary parts of $\rho_{\bar{n}}(x,x',t)$. Therefore, as those parts converge to 0 far from the diagonal, it is only on a specific region of the (x,x') space that the phase of $\rho_{\bar{n}}(x,x',t)$ can be accurately calculated. Still, the phase of $\rho_{\bar{n}}(x,x',t)$ is really similar to the phase of $\rho_0(x,x',t)$ as the $(0,\pi,2\pi)$ nodes appear to remain on the same position and are of the same size. This lead us to look for a more canonical form for $\rho_{\bar{n}}(x,x',t)$ with the same formalism as for Eq. (2.16), in this formalism $\rho_{\bar{n}}(x,x',t)$ could be written as follows:

$$\boxed{\rho_{\bar{n}}(x,x',t) = \mathrm{N}_{\bar{n}}(t)\mathrm{G}^{+}_{\bar{n}}(x,x',t)\mathrm{G}^{-}_{\bar{n}}(x,x',t)\exp(i\phi_{\bar{n}}(x,x',t))}. \tag{2.39}$$

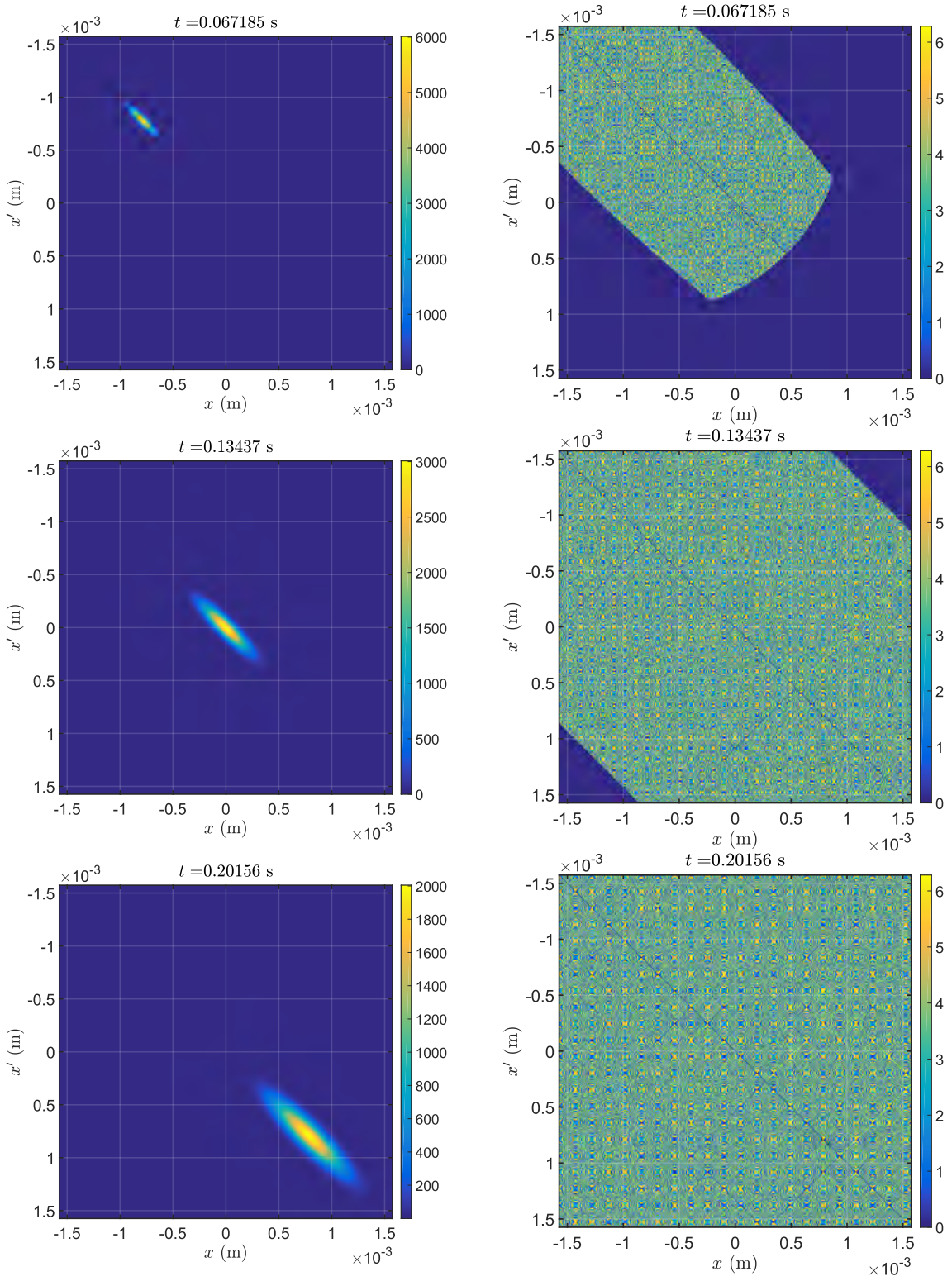

Figure 2.3: Plot of $\rho_{\bar{n}}(x, x', t)$ at three different times and for $T = 10$ nK. Left column, plots of $|\rho_{\bar{n}}(x, x', t)|$, we see a 2D elliptical Gaussian propagating on the diagonal and spreading on (x, x'). Right column, plots of $\arg(\rho_0(x, x', t))$, we can see nodes of values $(0, \pi, 2\pi)$ increasing in size as t increase. Let us note that the phase is calculated from the real and imaginary parts of $\rho_{\bar{n}}(x, x', t)$, therefore as they both converge to 0, only in a certain region of (x, x') can they be calculated.

2.2.2 A canonical formalism: $\mathrm{N}_{\bar{n}}(t)$

We know that $\rho_0(x,x,t) = |\psi_0(x,t)|^2$, which is in a normalised Gaussian canonical form. In this canonical form, $\Delta x(t)^2$ is the standard deviation and $\mathrm{N}_0(t) = 1/\sqrt{2\pi}\,\Delta x(t)$ is the normalisation factor. Therefore, following the same logic as Eq. 2.39, we expect here a normalised Gaussian function for $\rho_{\bar{n}}(x,x,t)$ with a standard deviation $\Delta x_{\bar{n}}(t)^2$ and a normalisation factor $\mathrm{N}_{\bar{n}}(t) = 1/\sqrt{2\pi}\,\Delta x_{\bar{n}(t)}$. Therefore, by identification, the normalisation factor $\mathrm{N}_{\bar{n}}(t)$ for $\rho_{\bar{n}}(x,x',t)$, from Eq. 2.38 is:

$$\mathrm{N}_{\bar{n}}(t) = \frac{1}{\sqrt{2\pi}\,\Delta x(t)}\frac{1}{2\pi\bar{n}}\sqrt{\frac{(2\pi)^2}{\det[\mathbf{A}]}}. \tag{2.40}$$

Then by calculating $\det[\mathbf{A}(t)]$ separately we have:

$$\begin{aligned}\det[\mathbf{A}(t)] =& \frac{1}{a_{\mathrm{ho}}^2}\left(\frac{1}{\bar{n}} + \frac{a_{\mathrm{ho}}^2}{\Delta x(t)^2}\right)a_{\mathrm{ho}}^2\left(\frac{1}{\bar{n}} + \frac{a_{\mathrm{ho}}^2}{\Delta x(t)^2}[\omega t]^2\right) - \frac{a_{\mathrm{ho}}^4}{\Delta x(t)^4}(\omega t)^2 \\ =& \frac{\Delta x(t)^2 + \bar{n}a_{\mathrm{ho}}^2\left(1+[\omega t]^2\right)}{\bar{n}^2\Delta x(t)^2}.\end{aligned} \tag{2.41}$$

We can now go back to the expression for $\mathrm{N}_{\bar{n}}(t)$:

$$\begin{aligned}\mathrm{N}_{\bar{n}}(t) =& \frac{1}{\sqrt{2\pi}\,\Delta x(t)\bar{n}}\frac{\bar{n}\Delta x(t)}{\sqrt{\Delta x(t)^2 + \bar{n}a_{\mathrm{ho}}^2\left(1+[\omega t]^2\right)}} \\ =& \frac{1}{\sqrt{2\pi}\sqrt{\Delta x(t)^2 + \bar{n}a_{\mathrm{ho}}^2\left(1+[\omega t]^2\right)}},\end{aligned} \tag{2.42}$$

identifying that:

$$\boxed{\Delta x_{\bar{n}}(t)^2 = \Delta x(t)^2 + \bar{n}a_{\mathrm{ho}}^2\left(1+[\omega t]^2\right)}. \tag{2.43}$$

Which can also be written in the following manner, as in Eq (2.23):

$$\boxed{\Delta x_{\bar{n}}(t)^2 = \frac{a_{\mathrm{ho}}^2}{2}\left(1+[\omega t]^2\right)(2\bar{n}+1) = \Delta x(t)^2(2\bar{n}+1)}. \tag{2.44}$$

In this expression, we see the increase of the standard deviation from the pure-state by the effect of temperature, as we observed in Fig. 2.3. We could then proceed to the next term, but first let us relate $\det[\mathbf{A}(t)]$ to $\Delta x_{\bar{n}}(t)^2$ (which will be useful going forward):

$$\det[\mathbf{A}(t)] = \frac{\Delta x_{\bar{n}}(t)^2}{\bar{n}^2\Delta x(t)^2}. \tag{2.45}$$

2.2.3 A canonical formalism: $\mathrm{G}^{+}_{\bar{n}}(x, x', t)$

Having defined $\Delta x_{\bar{n}}(t)$ by identification of $\mathrm{N}_{\bar{n}}(t)$, we can then expect $\mathrm{G}^{+}_{\bar{n}}(x, x', t)$ to have the following form:

$$\mathrm{G}^{+}_{\bar{n}}(x, x', t) = \exp\left[-\frac{([x - v_0 t] + [x' - v_0 t])^2}{8\Delta x_{\bar{n}}(t)^2}\right]. \tag{2.46}$$

However only the parts in $\vec{\mathbf{B}}^T \mathbf{A}^{-1} \vec{\mathbf{B}}$ that have $([x - v_0 t] + [x' - v_0 t])^2$ as common factors will be included in the expression for $\mathrm{G}^{+}_{\bar{n}}(x, x', t)$. By expanding $\vec{\mathbf{B}}^T \mathbf{A}^{-1} \vec{\mathbf{B}}$, we can write:

$$\begin{aligned}
\mathrm{G}^{+}_{\bar{n}}(x, x', t) =& \mathrm{G}^{+}_{0}(x, x', t) \\
&\times \exp\left[\frac{1}{2\det[\mathbf{A}(\mathbf{t})]}\left(\frac{a_{\mathrm{ho}}^2}{2\Delta x(t)^4}([x - v_0 t] + [x' - v_0 t])^2\right.\right. \\
&\qquad \times \left[\frac{(\omega t)^2}{2}\left(\frac{1}{\bar{n}} + \frac{a_{\mathrm{ho}}^2}{\Delta x(t)^2}\right) + \frac{1}{2}\left(\frac{1}{\bar{n}} + \frac{a_{\mathrm{ho}}^2}{\Delta x(t)^2}(\omega t)^2\right)\right. \\
&\qquad\left.\left.\left. - \frac{a_{\mathrm{ho}}^2}{\Delta x(t)^2}(\omega t)^2\right]\right)\right],
\end{aligned} \tag{2.47}$$

And using Eq. (2.45) for $\det[\mathbf{A}(t)]$ we have :

$$\begin{aligned}
\mathrm{G}^{+}_{\bar{n}}(x, x', t) =& \exp\left[([x - v_0 t] + [x' - v_0 t])^2\left(\frac{\bar{n} a_{\mathrm{ho}}^2}{8\Delta x(t)^2 \Delta x_{\bar{n}}(t)^2} - \frac{1}{8\Delta x(t)^2}\right)\right] && (2.48) \\
=& \exp\left[-\frac{([x - v_0 t] + [x' - v_0 t])^2}{8\Delta x_{\bar{n}}(t)^2}\right]. && (2.49)
\end{aligned}$$

Which agrees with our expectations from identification of a Gaussian wavepacket canonical form. However, we cannot go further with this method as there are no possible predictions by identification on the anti-diagonal and the phase terms.

2.2.4 A canonical formalism: $\mathrm{G}^{-}_{\bar{n}}(x, x', t)$

From Eq (2.38) and Fig (2.3) we know that the anti-diagonal Gaussian has a different standard deviation than the diagonal. Therefore, in this case we cannot really predict what we would obtain. However, in the same way as for $\mathrm{G}^{+}_{\bar{n}}(x, x', t)$, we can calculate $\mathrm{G}^{-}_{\bar{n}}(x, x', t)$, taking the parts of $\vec{\mathbf{B}}^T \mathbf{A}^{-1} \vec{\mathbf{B}}$ that has $([x - v_0 t] - [x' - v_0 t])^2$

as a common factor:

$$\begin{aligned}
&\mathrm{G}^{-}_{\bar{n}}(x,x',t) = \\
&\quad \mathrm{G}^{-}_{0}(x,x',t)\exp\Bigg[-\frac{\left([x-v_0t]-[x'-v_0t]\right)^2}{2\det[\mathbf{A}(\mathbf{t})]\Delta x(t)^4} \\
&\qquad \times\left(\frac{a_{\mathrm{ho}}^2}{4}\left(\frac{1}{\bar{n}}+\frac{a_{\mathrm{ho}}^2}{\Delta x(t)^2}[\omega t]^2\right)\left(\frac{v_\Delta t}{\Delta x(0)}\right)^2+\frac{\Delta x(0)^4}{a_{\mathrm{ho}}^2}\left(\frac{1}{\bar{n}}+\frac{a_{\mathrm{ho}}^2}{\Delta x(t)^2}\right)\right. \\
&\qquad\quad \left.+\frac{a_{\mathrm{ho}}^2}{\Delta x(t)^2}\omega t v_\Delta t\Delta x(0)\right)\Bigg],
\end{aligned} \tag{2.50}$$

using the relationship of Eq. (2.23) we have:

$$=\mathrm{G}^{-}_{0}(x,x',t)\exp\left[-\frac{\left([x-v_0t]-[x'-v_0t]\right)^2}{8\Delta x_{\bar{n}}(t)^2}2\bar{n}(2\bar{n}+1)\right] \tag{2.51}$$

$$=\exp\left[\left(-2\bar{n}(2\bar{n}+1)+\frac{\Delta x_{\bar{n}}(t)^2}{\Delta x(t)^2}\right)\frac{\left([x-v_0t]-[x'-v_0t]\right)^2}{8\Delta x_{\bar{n}}(t)^2}\right]. \tag{2.52}$$

We can now introduce $\Delta x^{-}_{\bar{n}}(t)^2$ such that:

$$\mathrm{G}^{-}_{\bar{n}}(x,x',t) =\exp\left[-\frac{\left([x-v_0t]-[x'-v_0t]\right)^2}{8\Delta x^{-}_{\bar{n}}(t)^2}\right], \tag{2.53}$$

therefore, we have:

$$\Delta x^{-}_{\bar{n}}(t)^2 =\frac{\Delta x(t)^2}{(2\bar{n}+1)}. \tag{2.54}$$

Let us note that $\Delta x_{\bar{n}}(t)^2 = \Delta x(t)^2(2\bar{n}+1)$, from this we then notice a certain symmetry with $\Delta x^{-}_{\bar{n}}(t)^2$ which show the following relation :

$$\Delta x_{\bar{n}}(t)\Delta x^{-}_{\bar{n}}(t) = \Delta x(t)^2 \tag{2.55}$$

As we will see, this relation shows a conservation of the 2D Gaussian's 'volume' (integrated over (x,x')) between $\mathrm{G}^{+}_{0}\mathrm{G}^{-}_{0}$ and $\mathrm{G}^{+}_{\bar{n}}\mathrm{G}^{-}_{\bar{n}}$. It also highlights the importance of the quantity $(2\bar{n}+1)$ as the signature of thermal effects and this agrees with the elliptical Gaussian we can observe in Fig (2.3).

2.2.5 A canonical formalism: $\phi_{\bar{n}}(x,x',t)$

Once we have taken the terms that have:

$$\left([x-v_0t]-[x'-v_0t]\right)^2, \qquad \text{and} \qquad \left([x-v_0t]+[x'-v_0t]\right)^2,$$

as common coefficients in $\vec{\mathbf{B}}^T\mathbf{A}^{-1}\vec{\mathbf{B}}$, we are left with only the imaginary terms that have

$$([x - v_0t] + [x' - v_0t])([x - v_0t] - [x' - v_0t]),$$

as common factors. This coincides with the last term of our density operator formalism. Our phase term $\phi_{\bar{n}}(x, x', t)$ is then:

$$\begin{aligned}
&\phi_{\bar{n}}(x, x', t) \\
&\quad = \phi_0(x, x', t) - \frac{a_{\mathrm{ho}}^2}{2\Delta x(t)^4}\frac{([x - v_0t] + [x' - v_0t])([x - v_0t] - [x' - v_0t])}{2\det[\mathbf{A}(\mathbf{t})]} \\
&\qquad\quad \times \left(\omega t\left[\frac{1}{\bar{n}} + \frac{a_{\mathrm{ho}}^2}{\Delta x(t)^2}(\omega t)^2\right] - \omega t\left[\frac{1}{\bar{n}} + \frac{a_{\mathrm{ho}}^2}{\Delta x(t)^2}\right] + \frac{a_{\mathrm{ho}}^2}{\Delta x(t)^2}\omega t\left[1 - (\omega t)^2\right]\right) \qquad (2.56) \\
&= \phi_0(x, x', t) - \frac{a_{\mathrm{ho}}^2}{2\Delta x(t)^4}\frac{([x - v_0t] + [x' - v_0t])([x - v_0t] - [x' - v_0t])}{2\det[\mathbf{A}(\mathbf{t})]} \times 0 \\
&= \phi_0(x, x', t). \qquad (2.57)
\end{aligned}$$

So it appears that the thermal mixed-state density operator has the same phase as the pure-state density operator, which can be interpreted as the temperature not having any effect on the phase of a thermal wavepacket. This result can actually be seen the Fig. 2.3 especially for the third time $t = 0.20156$ s (last line) in the plot of the phase (right column) equal to the phase of the pure-state in Fig. 2.1 for the same time (can be seen by looking at the position and the values of the nodes). This consideration is important as an unchanged phase means an unchanged interference fringes spatial frequency. However, this does not give us direct information on the impact of temperature on the contrast. Indeed, we can predict from the impact of the temperature on the anti-diagonal term that an increased temperature should decrease the contrast. This is an expected result that will be addressed in Chapter 3.

2.2.6 The analytic solution and expected values

Following Eq. (2.39), we can write the full analytic solution:

$$
\begin{aligned}
&\rho_{\bar{n}}(x,x',t) \\
&\quad = \mathrm{N}_{\bar{n}}(t)\mathrm{G}^{+}_{\bar{n}}(x,x',t)\mathrm{G}^{-}_{\bar{n}}(x,x',t)\exp(i\phi_0(x,x',t)) \qquad (2.58)\\
&\quad = \frac{1}{\sqrt{2\pi}\,\Delta x_{\bar{n}(t)}}\exp\left[-\frac{([x-v_0t]+[x'-v_0t])^2}{8\Delta x_{\bar{n}}(t)^2}\right]\exp\left[-\frac{([x-v_0t]-[x'-v_0t])^2}{8\Delta x^{-}_{\bar{n}}(t)^2}\right] \\
&\qquad \times \exp[ik_0([x-v_0t]-[x'-v_0t])] \\
&\qquad \times \exp\left[2i\frac{v_\Delta t}{\Delta x(0)}\frac{([x-v_0t]+[x'-v_0t])([x-v_0t]-[x'-v_0t])}{8\Delta x(t)^2}\right]. \qquad (2.59)
\end{aligned}
$$

Let us note that when $T \to 0$, $\bar{n} \to 0$ and we have $\rho_{\bar{n}}(x,x',t) = \rho_0(x,x',t)$, which is to be expected (this aspect will be discussed in Chapter 3 by extending our formalism). Therefore the main effect of temperature on the density operator is to effect the standard deviations of the diagonal and anti-diagonal Gaussian terms. From this point, one question remains, what is the effect of the temperature on the expected values?

We can address that point by using the density matrix $\rho_{\bar{n}}(x,x',t)$ to calculate the expected values of $\hat{x}$, $\hat{x}^2$, $\hat{p}$ and $\hat{p}^2$:

$$
\begin{aligned}
\langle\hat{x}\rangle &= \mathrm{Tr}[\hat{x}\hat{\rho}_{\bar{n}}] \\
&= v_0 t, \qquad (2.60)\\
\langle\hat{x}^2\rangle &= \mathrm{Tr}\left[\hat{x}^2\hat{\rho}_{\bar{n}}\right] \\
&= \Delta x_{\bar{n}}(t)^2 + \langle\hat{x}\rangle^2 \\
&= \Delta x(t)^2(2\bar{n}+1) + \langle\hat{x}\rangle^2\,, \qquad (2.61)\\
\langle\hat{p}\rangle &= \mathrm{Tr}[\hat{p}\hat{\rho}_{\bar{n}}] \\
&= \hbar k_0, \qquad (2.62)\\
\langle\hat{p}^2\rangle &= \mathrm{Tr}\left[\hat{p}^2\hat{\rho}_{\bar{n}}\right] \\
&= (\hbar\Delta k)^2(2\bar{n}+1) + \langle\hat{p}\rangle^2\,. \qquad (2.63)
\end{aligned}
$$

First, we see that the temperature does not change $\langle\hat{x}\rangle$ and $\langle\hat{p}\rangle$, however it does change for $\langle\hat{x}^2\rangle$ and $\langle\hat{p}^2\rangle$ by a factor $2\bar{n}+1$. This is the same factor which acts on $\Delta x_{\bar{n}}(t)^2$ (which follows since it is related to $\langle\hat{x}^2\rangle$) and on $\Delta x^{-}_{\bar{n}}(t)^2$. It appears that there is some particular physical interpretation of the $2\bar{n}+1$ term.

2.3 Interpretation of $2\bar{n}+1$ and conclusion

The first interpretation we can make on $2\bar{n}+1$ is that it quantifies how much $|\rho_{\bar{n}}(x,x',t)|$ is going to be deformed in comparison to $|\rho_0(x,x',t)|$. Indeed, following the 2D Gaussian view of $\mathrm{G}^+_{\bar{n}}\mathrm{G}^-_{\bar{n}}$, the elliptical deformation of the 2D Gaussian is decided by how much $\Delta x_{\bar{n}}(t)^2$ and $\Delta x^-_{\bar{n}}(t)^2$ differ. Therefore, following Eq. (2.44) and Eq. (2.54), the elliptical deformation depends of the value of $2\bar{n}+1$. Furthermore, $\bar{n}$ depends not only on the temperature, but also on the trap frequency ω, as you can see in Eq. (2.3). We can then plot $2\bar{n}+1$ as function of temperature for different values of ω.

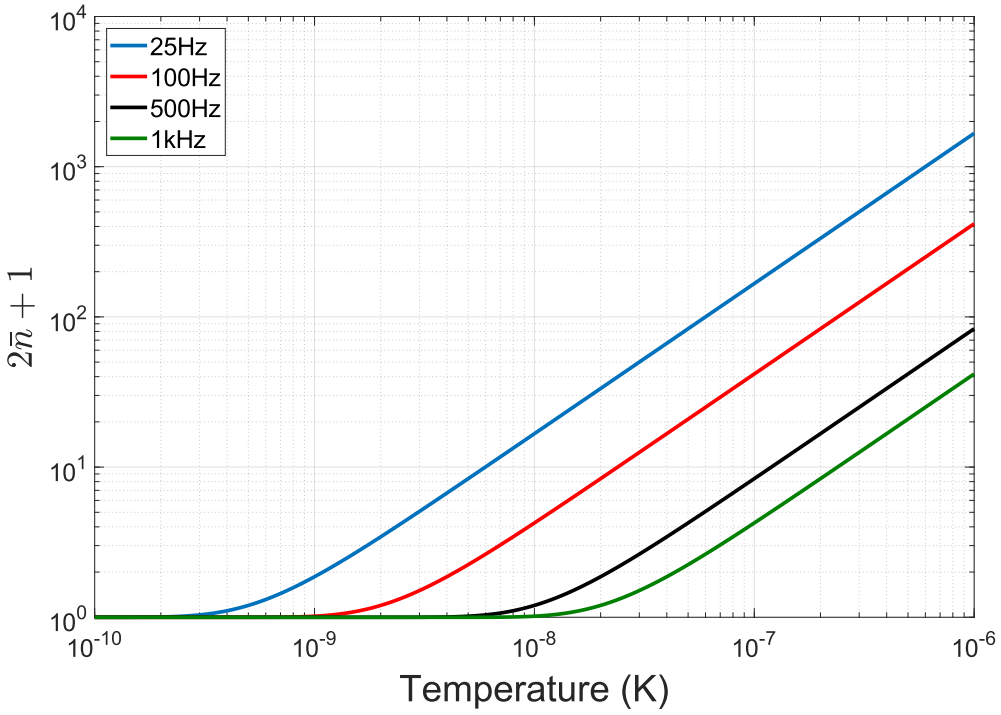

Figure 2.4: Plot of $(2\bar{n}+1)$ as function of temperature for different values of trap frequency ω (values in the legend correspond to $\omega/2\pi$). We see that as ω increases, the higher is the temperature to observe an effect of temperature on $|\rho_{\bar{n}}(x,x',t)|$.

Following Fig. 2.4, we can then deduce, for a given ω, which temperatures would have no visible impact on $|\rho_{\bar{n}}(x,x',t)|$, and which ones would have a huge impact. You can see in Fig. 2.5 the effect of 1 nK, 10 nK and 20 nK on $|\rho_{\bar{n}}(x,x',t)|$. These temperatures have been chosen following Fig. 2.4 for $\omega = 2\pi\times 100$ Hz as at $T = 1$ nK we should not see a visual difference from Fig. 2.1 at the same time $t = 0.13437$ s.

At $T = 10$ nK we have the same plot for Fig. 2.3 and finally at $T = 20$ nK, the value of $2\bar{n}+1$ is around twice its value then for $T = 10$ nK. These figures show how the value of $2\bar{n}+1$ effects $|\rho_{\bar{n}}(x,x',t)|$.

Another aspect that we have not addressed here, but is nevertheless related to the $2\bar{n}+1$ term, is the interpretation related to entropy. This interpretation comes from the fact that the 2D Gaussian $\mathrm{G}^{+}_{\bar{n}}\mathrm{G}^{-}_{\bar{n}}$ would have a 'volume' (integral over (x,x')) which is independent of T. However, due to the normalisation factors $\mathrm{N}_0(t)$ and $\mathrm{N}_{\bar{n}}(t)$, we have the following relations:

$$\iint |\rho_0(x,x',t)|^2 \,\mathrm{d}x\,\mathrm{d}x' = \mathrm{N}_0(t)^2 \iint \mathrm{G}^{+}_0(x,x',t)^2 \mathrm{G}^{-}_0(x,x',t)^2 \,\mathrm{d}x\,\mathrm{d}x' \,, \tag{2.64}$$

$$\iint |\rho_{\bar{n}}(x,x',t)|^2 \,\mathrm{d}x\,\mathrm{d}x' = \mathrm{N}_{\bar{n}}(t)^2 \iint \mathrm{G}^{+}_{\bar{n}}(x,x',t)^2 \mathrm{G}^{-}_{\bar{n}}(x,x',t)^2 \,\mathrm{d}x\,\mathrm{d}x' \,. \tag{2.65}$$

Furthermore, we have the following relation:

$$\mathrm{N}_{\bar{n}}(t)^2 = \frac{\mathrm{N}_0(t)^2}{2\bar{n}+1}. \tag{2.66}$$

It is therefore possible that the $2\bar{n}+1$ term appears in the linear entropy of a mixed state, as we have:

$$\mathrm{Tr}\left[\hat{\rho}^2_{\bar{n}}\right] = \int \rho^2_{\bar{n}}(x,x,t)\,\mathrm{d}x \tag{2.67}$$

$$= \int \left(\int \langle x|\hat{\rho}_{\bar{n}}|u\rangle \, \langle u|\hat{\rho}_{\bar{n}}|x\rangle \,\mathrm{d}u \right) \mathrm{d}x \tag{2.68}$$

$$= \iint \rho_{\bar{n}}(x,u,t)^2 \,\mathrm{d}u\,\mathrm{d}x \,. \tag{2.69}$$

However, we do not know how the phase would be effected in Eq. (2.69) as entropy has not been addressed in this thesis. We can, however, still expect that the quantity $2\bar{n}+1$ should be present or at least play a role in the linear entropy.

Still, something of importance for us is the effect of temperature on the contrast. This question will be addressed within the next Chapter.

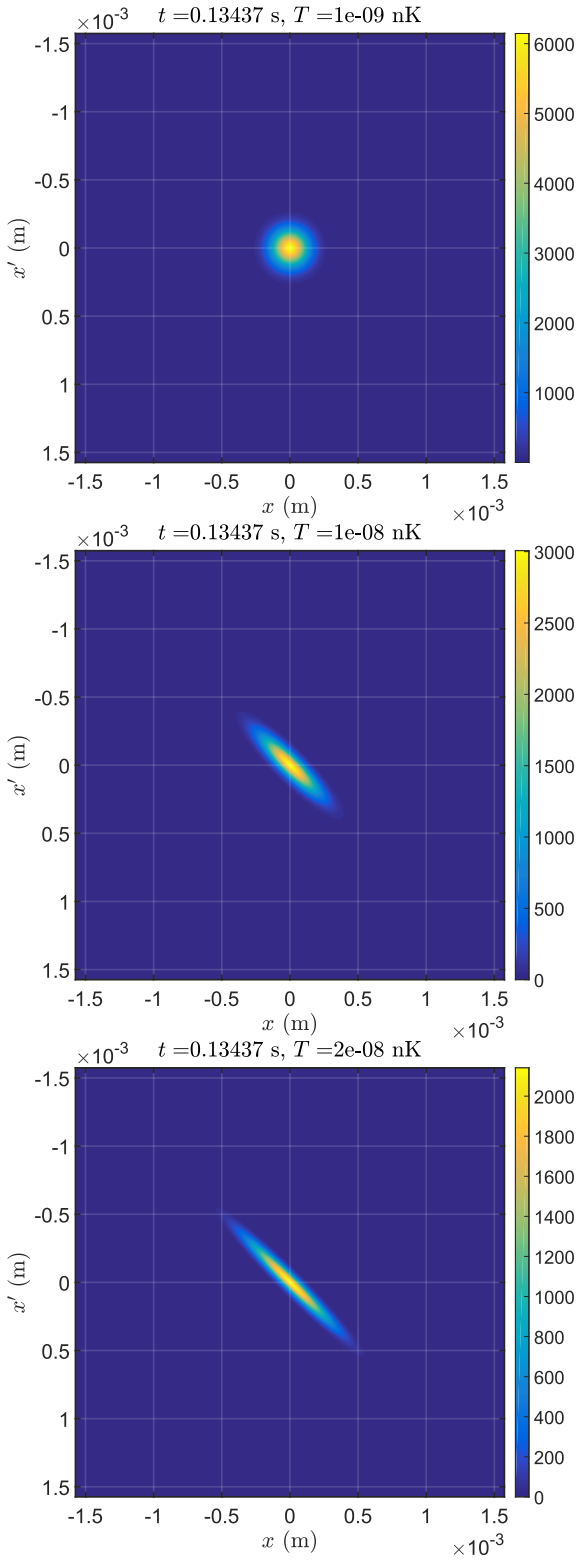

Figure 2.5: Plot of $|\rho_{\bar{n}}(x, x', t)|$ at the same time with three different temperatures. The parameters used are from Table 2.1.

Chapter 3

Interference fringes

We studied the effect of temperature on the spreading of a free wavepacket, which is important from an application perspective to the atomic ring waveguide gyros. Studying the effect of temperature on the interference fringes is then the crucial next step as inertial rotation measurements are done by looking at the interference. Indeed as we have showed before, the temperature does not effect the phase, therefore, we would expect no changes on the fringe spacing. However, the temperature does effect the wavepacket coherence (see Fig. 2.3), therefore, we expect to see the fringe contrast effected too. Using the thermal wavepacket formalism that we have developed in Chapter 2, we can now look at how our thermal wavepacket would produce interference.

With this in mind we will first use a naive approach where we will let two coherent wavepackets interfere with each-other, as a way to reproduce a single wavepacket interfering with itself in a closed ring waveguide [22]. Then we will try to increase the complexity by introducing the process of beam-splitting, then look for an interference sequence with double Bragg diffraction in order to get closer to an experimental process.

3.1 A näive picture for interference

The most common procedure to transfer an atomic cloud from a 3D trap to a ring waveguide is to release the cloud in a section of the waveguide from where it will spread, then, after some time, occupy the whole ring [22, 42, 26]. A less common

procedure is to transfer uniformly the initial cloud to the ring waveguide [43, 44]. Let us however, focus on the most common procedure as the cloud spreads in the waveguide, we will reach the moment where the two extremities of the cloud meet, the extremities will then interfer with each other [22]. However observing these interference experimentally is not easy. For example, in the experiment done by Thomas A. Bell & Jake A. P. Glidden [22], they compare a simulation showing interference, to an experiment where they are not measured. We present in Fig.3.1 a figure from [22] in which the simulation and the experiment are presented and compared. The absence of fringes in the experimental data is explained by the fringes being below the resolution of the imaging system.

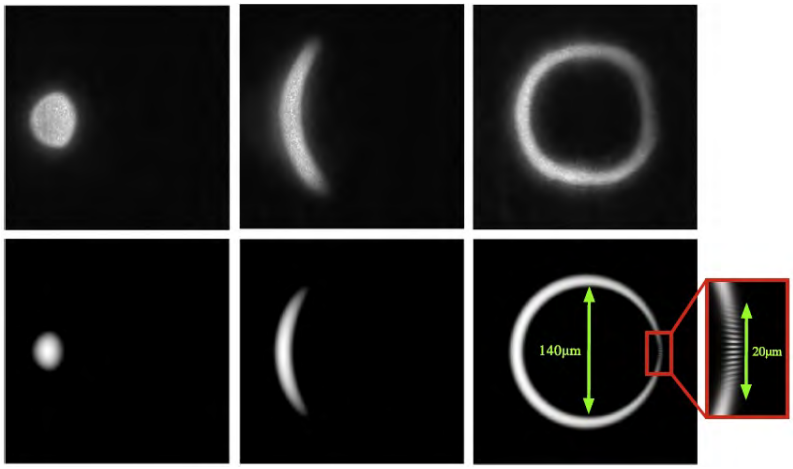

Figure 3.1: Comparison between simulation and experiment, work and figure published by Thomas A. Bell & Jake A. P. Glidden in [22]. The three images at the top shows an experimental Bose-Einstein Condensate (BEC) spreading in a ring waveguide. The three images at the bottom shows the simulation data of the experiment at the same times. The simulations show interference fringes which are not observed in the experiment.

Reflecting on Fig. 3.1, we want for our model to look at how it would predict the contrast of interference fringes then see under which conditions of temperature the contrast would permit to actually see fringes. We can actually try to address the question with a naive approach which would still give us insights on the contrast for more general situations. Our approach will be on the approximation of the ring waveguide to 1D free space (as in Chapter 2) considering, however, here the fact that the ring is a closed 1D azimuthal space. This will translate to us considering

our 1D waveguide of length L as a periodic 1D free space where the coordinates $x = 0$, $x = L$ and $x = 2L$ are the same positions. This representation can be seen in Fig. 3.2 where the closed 1D azimuthal space is a ring of perimeter L with a curvilinear coordinate $s(\theta)$ assimilated to a 1D linear coordinate x such that $s(\theta) = x$ modulo 2π, with $s(\theta = 0) = 0$ and $s(\theta = 2\pi) = L$.

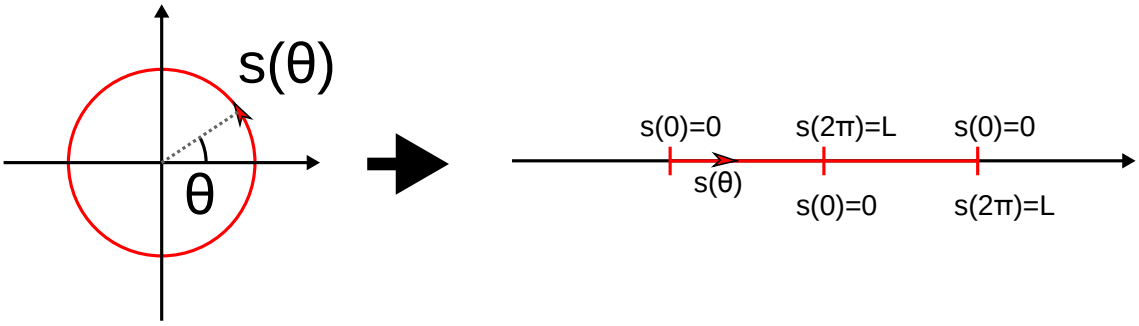

Figure 3.2: Schematic of an azimuthal 1D ring space extrapolated as a 1D linear space. You can see that it leads to consider a periodicity on the 1D linear space.

We can then treat the Self Interefering Single wavepacket (ψ_{SIS}) initially at position $x = 0$ as two distinct coherent wavepacket spreading from position $x = 0$ (ψ_1) and $x = L$ (ψ_2):

$$\psi_{\text{SIS}} = \frac{1}{\sqrt{\mathcal{N}}}(\psi_1 + \psi_2), \tag{3.1}$$

the expected meeting point is $x = L/2$, with $\mathcal{N}$ being a normalisation factor ($\mathcal{N} = 2$ in the numerical applications). Before going further, we need to redefine our notation using the definition of $\langle x|\psi_0\rangle$ from Eq. (2.8) and $\psi_0(x,t)$ of Eq. (2.4) such as:

$$\langle x|x_0, k_0\rangle \equiv \langle x|\psi_0\rangle \tag{3.2}$$

$$\psi(x_0, k_0; x, t) \equiv \psi_0(x, t) \tag{3.3}$$

We can extend this notation to the coherent state $\langle x|\alpha\rangle = \psi_\alpha(x,t)$ from Eq. (2.1) as follows:

$$\langle x|x_0 + x_\alpha, k_0 + k_\alpha\rangle \equiv \langle x|\alpha\rangle\,, \tag{3.4}$$

$$\psi(x_0 + x_\alpha, k_0 + k_\alpha; x, t) \equiv \psi_\alpha(x, t) \tag{3.5}$$

Such that for a given initial position x_{in} and initial momentum $\hbar k_{\text{in}}$, we can write a Gaussian wavepacket solution of a 1D free space Shrödinger equation as:

$$\langle x|x_{\text{in}}, k_{\text{in}}\rangle \equiv \psi(x_{\text{in}}, k_{\text{in}}; x, t) \tag{3.6}$$

With this notation, we can then rewrite Eq. (3.1) as:

$$\psi_{\text{SIS}} = \frac{1}{\sqrt{\mathcal{N}}}(\psi(x_1, k_1; x, t) + \psi(x_2, k_2; x, t)). \tag{3.7}$$

From this point, we want to write the density operator $\hat{\rho}_{\text{SIS}}$ related to ψ_{SIS}. Similarly to what we have done in Chapter 2, we want to write $\hat{\rho}_{\text{SIS}}$ without introducing $\bar{n}$ and $\mathcal{P}(\alpha)$, so we can see how thermal effect would effect the fringes from a more standard case. However, earlier in the case of $\hat{\rho}_0$ we had a pure state (in Chapter 2), which is not the case here. Therefore we need to keep extending our notation introduced in Eq. (3.2) and Eq. (3.3) to the density operators, in order to keep our formalism stable.

3.2 Notation and formalism of thermal density operators

The thermal density operator $\hat{\rho}_{\bar{n}}$ given in Eq. (2.58) is by definition a mixed state, as it is a sum of coherent wavepackets with $\mathcal{P}(\alpha)$ as a density distribution of those wavepackets, as you can see in Eq. (2.1). However from Eq. (2.2) we can write $\mathcal{P}(\alpha)$ as a 2D Gaussian distribution over $\{\alpha_{Re}, \alpha_{Im}\}$, which is equivalent to $\{x_\alpha, k_\alpha\}$ as they are related in Eq. (2.19) and Eq. (2.20). Therefore, $\mathcal{P}(\alpha)$ is as follow:

$$\mathcal{P}(\alpha) = \frac{1}{\sqrt{\pi\bar{n}}}\exp\left(-\frac{\alpha_{\text{Re}}^2}{\bar{n}}\right) \times \frac{1}{\sqrt{\pi\bar{n}}}\exp\left(-\frac{\alpha_{\text{Im}}^2}{\bar{n}}\right), \tag{3.8}$$

we can note that $\mathcal{P}(\alpha)$ is normalized to 1 in $\{\alpha_{Re}, \alpha_{Im}\}$ space. Therefore we can apply the zero variance limit for when $\bar{n} \to 0$ (equivalent to $T \to 0$), such that:

$$\lim_{\bar{n}\to 0} \mathcal{P}(\alpha) = \delta(x_\alpha)\delta(k_\alpha). \tag{3.9}$$

Moreover, with the zero variance limit, we can extend $\hat{\rho}_{\bar{n}}$ defined in Eq. (2.58) to $\hat{\rho}_0$ defined in Eq. (2.8) as follows:

$$\lim_{\bar{n}\to 0} \hat{\rho}_{\bar{n}} = \hat{\rho}_0. \tag{3.10}$$

Which is a limit that have been discussed in Chapter 2 and trivial when using the analytical expressions of $\rho_0(x, x', t)$ in Eq. (2.16) and of $\rho_{\bar{n}}(x, x', t)$ in Eq. (2.58). Let us therefore extend $\bar{n}$ too,

$$\bar{n}(T = 0) = 0. \tag{3.11}$$

We can now extrapolate the notation from Eq. (3.2) and Eq. (3.3) to the density matrix as follows:

$$\begin{aligned}\rho(x_0, k_0, \bar{n}; x, x', t) =& \rho_{\bar{n}}(x, x', t) \\ =& \iint \mathcal{P}(\alpha)\psi(x_0 + x_\alpha, k_0 + k_\alpha; x, t)\psi^\dagger(x_0 + x_\alpha, k_0 + k_\alpha; x', t)\,\mathrm{d}^2\alpha\,.\end{aligned} \tag{3.12}$$

Therefore we can write the density operator $\hat{\rho}_{\mathrm{SIS}}$ related to the interference as follow:

$$\begin{aligned}\rho_{\mathrm{SIS}}(x, x', t) =& \iint \frac{\mathcal{P}(\alpha)}{\mathcal{N}}[\psi(x_1 + x_\alpha, k_1 + k_\alpha; x, t) + \psi(x_2 + x_\alpha, k_2 + k_\alpha; x, t)] \\ & \times [\psi(x_1 + x_\alpha, k_1 + k_\alpha; x', t) + \psi(x_2 + x_\alpha, k_2 + k_\alpha; x', t)]^\dagger \mathrm{d}^2\alpha\end{aligned} \tag{3.13}$$

$$\begin{aligned}=& \frac{1}{\mathcal{N}}[\rho(x_1, k_1, \bar{n}; x, x', t) + \rho(x_2, k_2, \bar{n}; x, x', t)] \\ & + \frac{1}{\mathcal{N}} \iint \mathcal{P}(\alpha)\big[\psi(x_1 + x_\alpha, k_1 + k_\alpha; x, t)\psi^\dagger(x_2 + x_\alpha, k_2 + k_\alpha; x', t) \\ & + \psi(x_2 + x_\alpha, k_2 + k_\alpha; x, t)\psi^\dagger(x_1 + x_\alpha, k_1 + k_\alpha; x', t)\big]\,\mathrm{d}^2\alpha\end{aligned} \tag{3.14}$$

We can see that $\hat{\rho}_{\mathrm{SIS}}$ is a sum of $\hat{\rho}(x_1, k_1, \bar{n})$ and $\hat{\rho}(x_2, k_2, \bar{n})$, which correspond to the individuals density matrix of the two conter-propagating wavepacket, plus two more term that would correspond to cross-terms between the two wavepackets. Then let us call those cross-terms, in this particular case, $\hat{\rho}_{12}(\bar{n})$ and $\hat{\rho}_{21}(\bar{n})$ such that:

$$\rho_{12}(\bar{n}; x, x', t) = \iint \mathcal{P}(\alpha)\psi(x_1 + x_\alpha, k_1 + k_\alpha; x, t)\psi^\dagger(x_2 + x_\alpha, k_2 + k_\alpha; x', t)\,\mathrm{d}^2\alpha \tag{3.15}$$

$$\rho_{21}(\bar{n}; x, x', t) = \iint \mathcal{P}(\alpha)\psi(x_2 + x_\alpha, k_2 + k_\alpha; x, t)\psi^\dagger(x_1 + x_\alpha, k_1 + k_\alpha; x', t)\,\mathrm{d}^2\alpha \tag{3.16}$$

We will now proceed by trying to give an analytical expression to $\hat{\rho}_{12}(\bar{n})$ and $\hat{\rho}_{21}(\bar{n})$.

3.3 Case of $\bar{n} = 0$

As in Chapter 2, let us first consider the case of $\bar{n} = 0$, so that we have something to compare to when we will consider $\bar{n} > 0$. Therefore, using the zero variance limit and Eq. (3.9), we can write $\hat{\rho}_{12}(0)$ and $\hat{\rho}_{21}(0)$ as follow:

$$\rho_{12}(0; x, x', t) = \psi(x_1, k_1; x, t)\psi^{\dagger}(x_2, k_2; x', t), \tag{3.17}$$

$$\rho_{21}(0; x, x', t) = \psi(x_2, k_2; x, t)\psi^{\dagger}(x_1, k_1; x', t). \tag{3.18}$$

It is not obvious at this point if $\hat{\rho}_{12}(0)$ and $\hat{\rho}_{21}(0)$ are hermitian conjugates due to the presence of x_1 and x_2. However, $\hat{\rho_{\text{SIS}}}$ should conserve the hermiticity property. We will then focus on the calculation of the cross-terms $\hat{\rho}_{12}(0)$ and $\hat{\rho}_{21}(0)$.

3.3.1 Calculation of $\rho_{\text{SIS}}(\bar{n} = 0; x, x', t)$ cross-term

For now, we are assuming that $|k_1| = |k_2|$ (for simplicity), therefore, let us focus on $\hat{\rho}_{12}(0)$ then calculate $\hat{\rho}_{21}(0)$ separately:

$$\rho_{12}(0;x,x',t) =$$
$$\frac{1}{\sqrt{2\pi}\,\Delta x(t)}\exp\left[-\frac{(x-x_1-v_1t)^2}{4\Delta x(t)^2}\right]\exp\left[-\frac{(x'-x_2-v_2t)^2}{4\Delta x(t)^2}\right]$$
$$\times\exp\Bigg[i(k_1[x-x_1]-\omega_1t)-i(k_2[x'-x_2]-\omega_2t)$$
$$-i\frac{v_1^2t^2}{4\Delta x(t)^2}\frac{v_\Delta t}{\Delta x(0)}+i\frac{v_2^2t^2}{4\Delta x(t)^2}\frac{v_\Delta t}{\Delta x(0)}\Bigg]$$
$$\times\exp\left[i\frac{v_\Delta t}{\Delta x(0)}\frac{(x-x_1-v_1t)^2}{4\Delta x(t)^2}-i\frac{v_\Delta t}{\Delta x(0)}\frac{(x'-x_2-v_2t)^2}{4\Delta x(t)^2}\right] \tag{3.19}$$

$$=\frac{1}{\sqrt{2\pi}\,\Delta x(t)}\exp\left[-\frac{([x-x_1-v_1t]+[x'-x_2-v_2t])^2}{8\Delta x(t)^2}\right]$$
$$\times\exp\left[-\frac{([x-x_1-v_1t]-[x'-x_2-v_2t])^2}{8\Delta x(t)^2}\right]$$
$$\times\exp[ik_1(x-x_1)-ik_2(x'-x_2)]\exp\Bigg[2i\frac{v_\Delta t}{\Delta x(0)}$$
$$\times\frac{\Big([x-x_1-v_1t]+[x'-x_2-v_2t]\Big)\Big([x-x_1-v_1t]-[x'-x_2-v_2t]\Big)}{8\Delta x(t)^2}\Bigg] \tag{3.20}$$

Using the same steps we can write $\hat{\rho}_{21}(0)$ as follow:

$$\rho_{21}(0;x,x',t) =$$
$$\frac{1}{\sqrt{2\pi}\,\Delta x(t)}\exp\left[-\frac{([x-x_2-v_2t]+[x'-x_1-v_1t])^2}{8\Delta x(t)^2}\right]$$
$$\times\exp\left[-\frac{([x-x_2-v_2t]-[x'-x_1-v_1t])^2}{8\Delta x(t)^2}\right]$$
$$\times\exp[ik_2(x-x_2)-ik_1(x'-x_1)]\exp\Bigg[2i\frac{v_\Delta t}{\Delta x(0)}$$
$$\times\frac{\Big([x-x_2-v_2t]+[x'-x_1-v_1t]\Big)\Big([x-x_2-v_2t]-[x'-x_1-v_1t]\Big)}{8\Delta x(t)^2}\Bigg] \tag{3.21}$$

At this point, we can determine that $\hat{\rho}_{21}(0)$ is not the hermitian conjugate of $\hat{\rho}_{12}(0)$. Furthermore, we also recognize the canonical formalism we used in Chapter 2

with the diagonal Gaussian, the anti-diagonal Gaussian and the phase. We can note that for $\hat{\rho}_{21}(0)$ and $\hat{\rho}_{12}(0)$ the diagonal Gaussians expression are equal and by looking at the phases expressions we can predict the apparition of the fringes as a *cos* function over $x = x'$. However, the action of the anti-diagonal is not straight forward. Therefore, we will once again introduce new terms in order to give more sense to the equation relative to the nature of our problem. Let us introduce x_+, x_-, v_+ and v_- such as:

$$x_+ = \frac{x_1 + x_2}{2} \qquad x_- = \frac{x_1 - x_2}{2} \tag{3.22}$$

$$v_+ = \frac{v_1 + v_2}{2} \qquad v_- = \frac{v_1 - v_2}{2} \tag{3.23}$$

$$k_+ = \frac{k_1 + k_2}{2} \qquad k_- = \frac{k_1 - k_2}{2} \tag{3.24}$$

Then Eq. (3.20) become:

$$\begin{aligned}
&\rho_{12}(0; x, x', t) = \\
&\frac{1}{\sqrt{2\pi}\,\Delta x(t)} \exp\left[-\frac{([x - (x_+ + v_+t)] + [x' - (x_+ + v_+t)])^2}{8\Delta x(t)^2}\right] \\
&\times \exp\left[-\frac{([x - x'] - 2[x_- + v_-t])^2}{8\Delta x(t)^2}\right] \\
&\times \exp[ik_1(x - x_1) - ik_2(x' - x_2)] \exp\left[2i\frac{v_\Delta t}{\Delta x(0)}\right. \\
&\left.\times \frac{\Big([x - (x_+ + v_+t)] + [x' - (x_+ + v_+t)]\Big)\Big([x - (x_- + v_-t)] - [x' + (x_- + v_-t)]\Big)}{8\Delta x(t)^2}\right],
\end{aligned} \tag{3.25}$$

and Eq. (3.21) become:

$$
\begin{aligned}
&\rho_{21}(0;x,x',t) = \\
&\frac{1}{\sqrt{2\pi}\,\Delta x(t)}\exp\left[-\frac{\left([x-(x_+ + v_+t)] + [x'-(x_+ + v_+t)]\right)^2}{8\Delta x(t)^2}\right] \\
&\times \exp\left[-\frac{\left([x-x'] + 2[x_- + v_-t]\right)^2}{8\Delta x(t)^2}\right] \\
&\times \exp[-ik_1(x'-x_1) + ik_2(x-x_2)]\exp\left[2i\frac{v_\Delta t}{\Delta x(0)}\right. \\
&\left.\times \frac{\Big([x-(x_+ + v_+t)] + [x'-(x_+ + v_+t)]\Big)\Big([x+(x_- + v_-t)] - [x'-(x_- + v_-t)]\Big)}{8\Delta x(t)^2}\right].
\end{aligned}
\tag{3.26}
$$

Therefore, using Eq. (3.25) and Eq. (3.26) we can write the total cross-term component of ρ_{SIS} as:

$$
\begin{aligned}
&\rho_{12}(0;x,x',t) + \rho_{12}(0;x,x',t) = \\
&\quad\frac{1}{\sqrt{2\pi}\,\Delta x(t)}\exp\left[-\frac{\left([x-(x_+ + v_+t)] + [x'-(x_+ + v_+t)]\right)^2}{8\Delta x(t)^2}\right] \\
&\quad\times\left(\exp\left[-\frac{\left([x-x'] - 2[x_- + v_-t]\right)^2}{8\Delta x(t)^2}\right]e^{i[k_1(x-x_1)-k_2(x'-x_2)]}\right. \\
&\qquad\qquad\times e^{iC(x,x',t)\left(\left[x-(x_- + v_-t)\right]-\left[x'+(x_- + v_-t)\right]\right)} \\
&\qquad\left.+\exp\left[-\frac{\left([x-x'] + 2[x_- + v_-t]\right)^2}{8\Delta x(t)^2}\right]e^{-i[k_1(x'-x_1)-k_2(x-x_2)]}\right. \\
&\qquad\qquad\left.\times e^{-iC(x,x',t)\left(\left[x+(x_- + v_-t)\right]-\left[x'-(x_- + v_-t)\right]\right)}\right)
\end{aligned}
\tag{3.27}
$$

where:

$$
C(x,x',t) = \frac{v_\Delta t}{\Delta x(0)}\frac{\Big([x-(x_+ + v_+t)] + [x'-(x_+ + v_+t)]\Big)}{4\Delta x(t)^2}. \tag{3.28}
$$

We can recognize in Eq. (3.27) some terms close to Euler's cosine formula (and its extension to hyperbolic cosines). We can then apply the following formula in order to make the hyperbolic cosines term appear:

$$
e^a + e^b = 2e^{\frac{a+b}{2}}\cosh\left(\frac{a-b}{2}\right), \tag{3.29}
$$

where $(a, b) \in \mathbb{C}^2$ and if (a, b) are both pure imaginary then the hyperbolic cosine becomes a regular cosine. Therefore we can write Eq. (3.27) as follow:

$$\begin{aligned}\rho_{12}(0; x, x', t) + \rho_{12}(0; x, x', t) = \\ &\frac{1}{\sqrt{2\pi}\,\Delta x(t)} \exp\left[-\frac{([x - (x_+ + v_+t)] + [x' - (x_+ + v_+t)])^2}{8\Delta x(t)^2}\right] \\ &\times 2\exp\left[-\frac{(x - x')^2 + 4(x_- + v_-t)^2}{8\Delta x(t)^2}\right] \exp\left[i(x - x')(k_+ + C(x, x', t))\right] \\ &\times \cosh\Bigg(\frac{(x - x')(x_- + v_-t)}{2\Delta x(t)^2} \\ &\qquad + i(k_-[x + x'] - 2[k_+x_- + k_-x_+]) - i(2C(x, x', t)[x_- + v_-t])\Bigg).\end{aligned} \tag{3.30}$$

With Eq. (3.30) we can then write and plot $\rho_{\text{SIS}}(x, x', t)$ and look at interference of wavepackets with or without momenta (as long as they have the same normalisation). However, in this chapter we focus for now on the case of static wavepackets spreading and interfering with each other, we will now discuss the fringes in this case.

3.3.2 Fringes and the static spatial frequency

The $\rho_{\text{SIS}}(0; x, x', t)$ cross-term in Eq. (3.30) can give us an intuition on the interference fringes. First, let us remind ourselves that it is in the diagonal of our matrices that the physical space is represented. Therefore, we can identify in Eq. (3.30) (when $x = x'$) a normalised Gaussian envelop:

$$\frac{1}{\sqrt{2\pi}\,\Delta x(t)} \exp\left[-\frac{([x - (x_+ + v_+t)] + [x - (x_+ + v_+t)])^2}{8\Delta x(t)^2}\right], \tag{3.31}$$

what we identify as a contrast term:

$$\exp\left[-\frac{4(x_- + v_-t)^2}{8\Delta x(t)^2}\right], \tag{3.32}$$

and the sinusoidal term that will create our fringes:

$$\cos\Big(2k_-x - 2[k_+x_- + k_-x_+] - 2C(x, x, t)[x_- + v_-t]\Big). \tag{3.33}$$

Let us note that in the cosine, we can distinguish two spatial frequencies, one related to the momenta: $2k_-x$, the other, related to the spreading of the wavepacket and the

Our parameter	Value used	Reference
ω	$2\pi \times 100$ Hz	arbitrary
m	$1.44316060 \times 10^{-25}$ Kg	[40]
$\hbar$	1.054571×10^{-34} J $\cdot$ s	[40]
k_{B}	1.380650×10^{-23} J $\cdot$ K^{-1}	[40]
k_1	0	
k_2	0	
L	$\pi \times 140$ μm	[22]
x_1	0	
x_2	L	

Table 3.1: Table of parameters used in Fig. 3.3, in Fig. 3.5 and Fig. 3.6.

relative initial position: $2C(x,x,t)[x_- + v_- t]$. It is therefore this spatial frequency, that we call the static frequency, which is of interest in order to produce fringes comparable to Fig. 3.1. Furthermore, as we are still in the case of $\bar{n} = 0$, thus Eq. (3.30) can be compared to the fringes of $|\psi_{\mathrm{SIS}}|^2$ from Eq. (3.7), for $x = x'$.

When we have static wavepackets ($k_1 = 0$ and $k_2 = 0$), we can write the angular spatial frequency $f(t)$ from Eq. (3.33) (and from $|\psi_{\mathrm{SIS}}|^2$) as:

$$\begin{aligned}\cos(2C(x,x,t)x_-) &= \cos\left(-2x_- \frac{v_\Delta t}{\Delta x(0)} \frac{(2x - 2x_+)}{4\Delta x(t)^2}\right) \\ &= \cos\left(-\frac{v_\Delta t}{\Delta x(0)} \frac{x_-}{\Delta x(t)^2}(x - x_+)\right),\end{aligned} \tag{3.34}$$

therefore, from Eqs. (2.23), we can write:

$$\begin{aligned}f(t) &= -\frac{v_\Delta t}{\Delta x(0)} \frac{x_-}{\Delta x(t)^2} \\ &= -\frac{2x_-}{a_{\mathrm{ho}}^2} \frac{\omega t}{1 + (\omega t)^2}.\end{aligned} \tag{3.35}$$

In Fig. 3.3 we estimate the spatial frequency from Eq. (3.35). The parameters used for Fig. 3.3 can be seen in Tab. 3.1. The estimation of $f(t)$ is important as we can easily fall into the trap of spatial aliasing effects due to a bad choice of spatial sampling frequency.

Indeed, as you can see in Fig. 3.3, the angular spatial frequency $f(t)$ have a peak in the order of 10^8 m^{-1} (for $\omega = 100$ Hz), then decrease reaching the order of

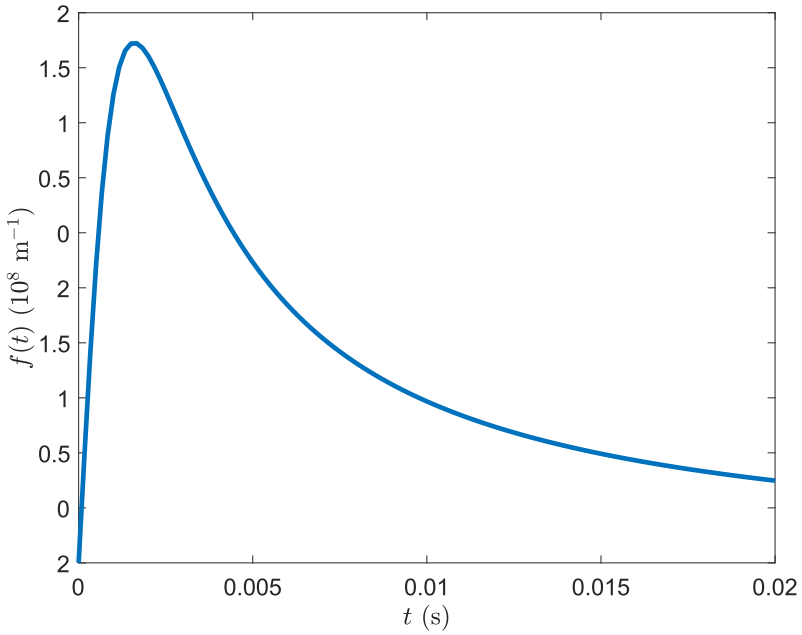

Figure 3.3: Plot of the angular spatial frequency $f(t)$, the parameters used for this plot can be seen in Tab. 3.1. The time scale focus on the initial peak where $f(t)$ reach its maximum value, but, in our case the wavepackets meet at longer times where $f(t)$ is in the order of 10^6 m^{-1}.

10^6 m^{-1} at a time which correspond to when the two wavepackets will meet (this time is outside the time scale of Fig. 3.3 which focus on the initial peak). We can also estimate the time at which we expect the spreading wavepackets to meet with v_Δ from Eq. (2.7), and by estimating $f(L/2v_\Delta)$ we can choose a spatial step of $\simeq 2\times10^{-8}$ m. However, the size of our 1D free space is $L \simeq 4.4\times10^{-4}$ m, therefore, we cannot use a spatial definition capable to show both the full space and the fringes. We then decide to zoom on $L/2 \simeq 2.2\times10^{-4}$ m and see the interference fringes, as you can see in Fig. 3.4.

The first thing we can comment on Fig. 3.4 is the surprisingly high spatial frequency for our chosen trap frequency ω. As it was discussed in [22], observing those fringes related to the spreading appears to be a technical challenge. The second notable thing in Fig. 3.4, is the symmetry of the diagonal and anti-diagonal spatial frequencies. It is however, somewhat to be expected if we extrapolate a perfect symmetry from diagonal and anti-diagonal in Fig. 2.1. Now that we have a reference expression for a non-thermal $\hat{\rho}_{\mathrm{SIS}}$, we can push our study to the effect of temperature on $\hat{\rho}_{\mathrm{SIS}}$.

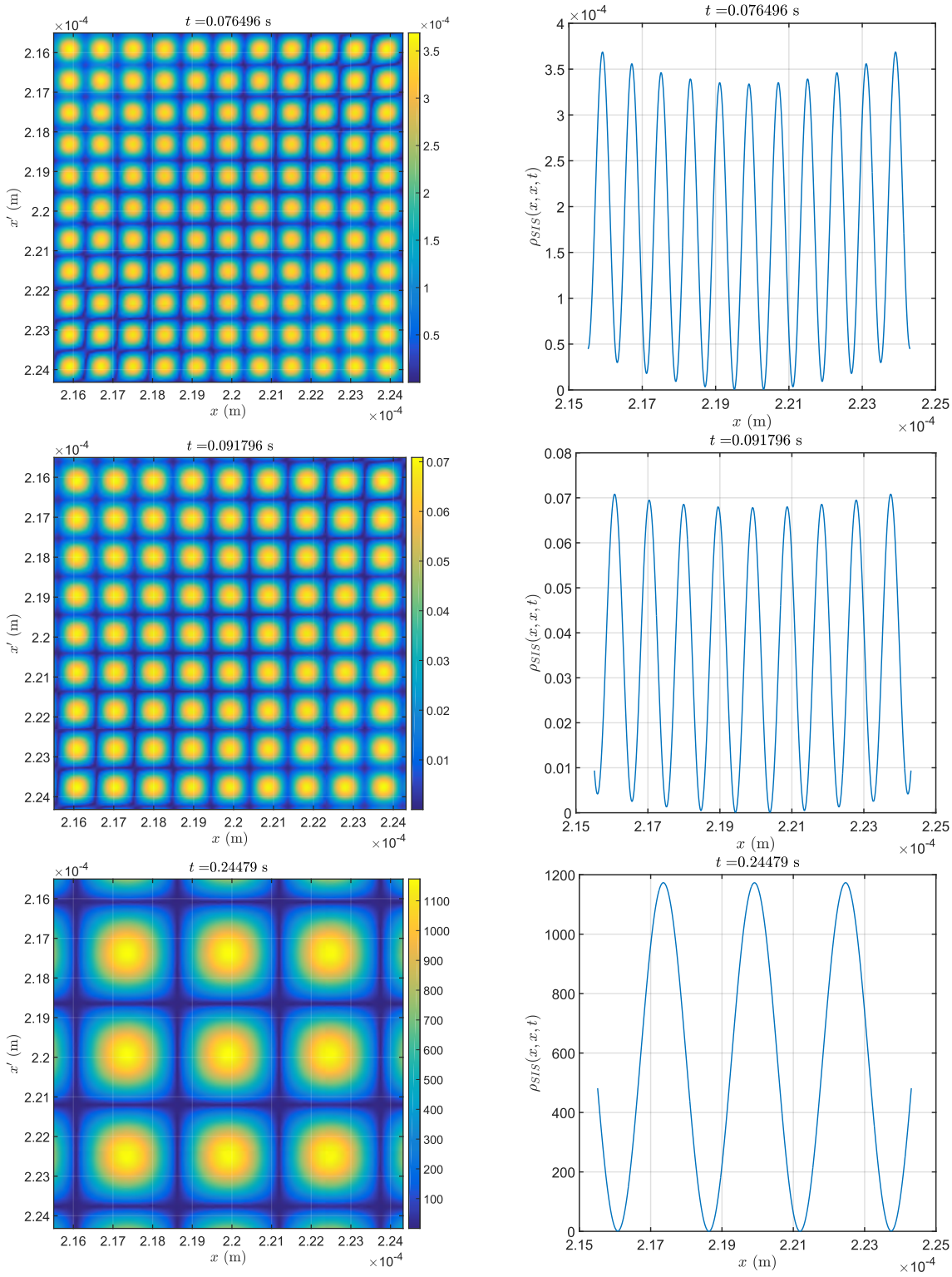

Figure 3.4: Interference pattern using the values in Tab. 3.1 for $\bar{n} = 0$. Left column, we have $|\rho_{\mathrm{SIS}}(0; x, x', t)|$ and its diagonal $\rho_{\mathrm{SIS}}(0; x, x, t)$ on the right column, each lines show different times. The first two lines show the fringes before the wavepackets meet and when they are getting closer (the value of $\hat{\rho}_{\mathrm{SIS}}$ is negligible), the last line show the fringes when the wavepackets have met. Both diagonal and anti-diagonal spatial frequency are the same as expected when $\bar{n} = 0$.

3.4 Case of $\bar{n} > 0$

Following the same method as in Section. 2.2, we will start by identifying the matrix $\mathbf{A}(t)$ and the vector $\vec{\mathbf{B}}^{12}$ associated to our case (where $|k_1| = |k_2|$). It should be straight forward as we build our formalism in Chapter 2 focusing on a symmetry around the relative wavepacket center: "$\big(x - [x_0 + v_0 t]\big)$".

3.4.1 Matrix $\mathbf{A}(t)$ and vector $\vec{\mathbf{B}}^{12}(x, x', t)$

Therefore, let us start by calculating $\psi(x_1 + x_\alpha, k_1 + k_\alpha; x, t)\psi^\dagger(x_2 + x_\alpha, k_2 + k_\alpha; x', t)$:

$$
\begin{aligned}
&\psi(x_1 + x_\alpha, k_1 + k_\alpha; x, t)\psi^\dagger(x_2 + x_\alpha, k_2 + k_\alpha; x', t) = \\
&\Big(\sqrt{(2\pi)}\Delta x(t)\Big)^{-1} \exp\left[-\frac{\big([x - (x_1 + x_\alpha) - (v_1 + v_\alpha)t]\big)^2}{4\Delta x(t)^2}\right] \\
&\times \exp\left[-\frac{\big([x' - (x_2 + x_\alpha) - (v_2 + v_\alpha)t]\big)^2}{4\Delta x(t)^2}\right] \\
&\times \exp[i(k_1 + k_\alpha)(x - x_1 - x_\alpha) - i\omega_{1+\alpha}t - i(k_2 + k_\alpha)(x' - x_2 - x_\alpha) + i\omega_{2+\alpha}t] \\
&\times \exp\left[i\frac{v_\Delta t}{\Delta x(0)}\frac{\big([x - x_1 - v_1 t] - [x_\alpha + v_\alpha t]\big)^2}{4\Delta x(t)^2}\right. \\
&\qquad\qquad \left. - i\frac{v_\Delta t}{\Delta x(0)}\frac{\big([x' - x_2 - v_2 t] - [x_\alpha + v_\alpha t]\big)^2}{4\Delta x(t)^2}\right] \\
&\times \exp\left[-\frac{i}{2}\cos^{-1}\left(\frac{1}{2\Delta x(t)\Delta k}\right) + \frac{i}{2}\cos^{-1}\left(\frac{1}{2\Delta x(t)\Delta k}\right)\right],
\end{aligned}
\tag{3.36}
$$

$$
\begin{aligned}
=&\Big(\sqrt{(2\pi)}\Delta x(t)\Big)^{-1} \exp\left[-\frac{\big([x - x_1 - v_1 t] - [x_\alpha + v_\alpha t]\big)^2}{4\Delta x(t)^2}\right] \\
&\times \exp\left[-\frac{\big([x' - x_2 - v_2 t] - [x_\alpha + v_\alpha t]\big)^2}{4\Delta x(t)^2}\right] \\
&\times \exp\big[i\big(k_\alpha[x - x_1 - x' + x_2] + x_\alpha[k_2 - k_1] + k_1[x - x_1] - k_2[x' - x_2]\big)\big] \\
&\times \exp\left[i\frac{v_\Delta t}{\Delta x(0)}\left(\frac{\big([x - x_1 - v_1 t] - [x_\alpha + v_\alpha t]\big)^2}{4\Delta x(t)^2} - \frac{\big([x' - x_2 - v_2 t] - [x_\alpha + v_\alpha t]\big)^2}{4\Delta x(t)^2}\right)\right].
\end{aligned}
\tag{3.37}
$$

Therefore, since the integration is done over $\{x_\alpha, k_\alpha\}$ we can separate out the terms that are independent of these. By doing so, we recognize $\rho_{12}(0; x, x', t)$:

$$\begin{aligned}
&\rho_{12}(\bar{n}; x, x', t) = \\
&\rho_{12}(0; x, x', t)\frac{1}{\pi\bar{n}}\iint \exp\left[-\frac{x_\alpha^2}{2\bar{n}a_{\text{ho}}^2}\right]\exp\left[-\frac{a_{\text{ho}}^2 k_\alpha^2}{2\bar{n}}\right] \\
&\times \exp[ik_\alpha(x - x_1 - x' + x_2) + ix_\alpha(k_2 - k_1)] \\
&\times \exp\left[\frac{-1}{4\Delta x(t)^2}\Big(+ 2x_\alpha^2 + 4x_\alpha v_\alpha t + 2v_\alpha^2 t^2 - 2x_\alpha[(x - x_1 - v_1 t) + (x' - x_2 - v_2 t)]\right. \\
&\qquad\qquad \left. - 2v_\alpha t[(x - x_1 - v_1 t) + (x' - x_2 - v_2 t)]\Big)\right] \\
&\times \exp\left[\frac{v_\Delta t}{\Delta x(0)}\frac{i}{4\Delta x(t)^2}\Big(- 2x_\alpha[(x - x_1 - v_1 t) - (x' - x_2 - v_2 t)]\right. \\
&\qquad\qquad \left. - 2v_\alpha t[(x - x_1 - v_1 t) - (x' - x_2 - v_2 t)]\Big)\right] \\
&\qquad\qquad \times \frac{\mathrm{d}x_\alpha\,\mathrm{d}k_\alpha}{2}.
\end{aligned} \tag{3.38}$$

Now we will use Eq. (2.30) and identify the coefficients for x_α^2, k_α^2 and $x_\alpha k_\alpha$. By doing so, we can see we that have the same matrix $\mathbf{A}(t)$ as in Eq. (2.34):

$$\boxed{\mathbf{A}(t) = \begin{pmatrix} \frac{1}{a_{\text{ho}}^2}\left(\frac{1}{\bar{n}} + \frac{a_{\text{ho}}^2}{\Delta x(t)^2}\right) & \frac{a_{\text{ho}}^2}{\Delta x(t)^2}\omega t \\ \frac{a_{\text{ho}}^2}{\Delta x(t)^2}\omega t & a_{\text{ho}}^2\left(\frac{1}{\bar{n}} + \frac{a_{\text{ho}}^2}{\Delta x(t)^2}[\omega t]^2\right) \end{pmatrix}}. \tag{3.39}$$

Now we will identify the coefficients for x_α and k_α. By doing so we will have the vector $\vec{\mathbf{B}}^{12}$, which is actually different from Eq. (2.37):

$$\begin{aligned}
&\boxed{B_1^{12}(x, x', t) = \frac{1}{2\Delta x(t)^2}\Big([(x - x_1 - v_1 t) + (x' - x_2 - v_2 t)]} \\
&\qquad\qquad \boxed{-i\omega t[(x - x_1 - v_1 t) - (x' - x_2 - v_2 t)]\Big) + i(k_2 - k_1)}
\end{aligned} \tag{3.40}$$

$$\begin{aligned}
&\boxed{B_2^{12}(x, x', t) = \frac{1}{2\Delta x(t)^2}\Big(a_{\text{ho}}^2\omega t[(x - x_1 - v_1 t) + (x' - x_2 - v_2 t)]} \\
&\qquad\qquad \boxed{+ia_{\text{ho}}^2[(x - x_1 - v_0 t) - (x' - x_2 - v_2 t)]\Big)}.
\end{aligned} \tag{3.41}$$

We can see, however, that if $k_1 = k_2$ and $x_1 = x_2$ we have $\vec{\mathbf{B}}^{12} = \vec{\mathbf{B}}$. Finally, we can write $\rho_{12}(\bar{n}; x, x', t)$:

$$\boxed{\rho_{12}(\bar{n}; x, x', t) = \rho_{12}(0; x, x', t) \frac{1}{\bar{n}\sqrt{\det[\mathbf{A}(t)]}} \exp\left[\frac{1}{2}\vec{\mathbf{B}}^{12}(x, x', t)^T \mathbf{A}(t)^{-1} \vec{\mathbf{B}}^{12}(x, x', t)\right]}. \tag{3.42}$$

Knowing that $\rho_{12}(\bar{n}; x, x', t)^\dagger = \rho_{21}(\bar{n}; x, x', t)$, we can then compute $\rho_{\mathrm{SIS}}(\bar{n}; x, x', t)$ from Eq. (3.42). You can see in Fig. 3.5 the plots of $\rho_{\mathrm{SIS}}(\bar{n}; x, x', t)$ to compare with the plots of $\rho_{\mathrm{SIS}}(\bar{n}; x, x', t)$ in Fig. 3.4. We can see the expected loss of contrast which is already significant at 5 nK. Furthermore, we see the consequences of the higher diagonal spreading, not only we see the wavepackets reach $L/2$ faster, but we can also see an 'offset' to the fringes due to this spreading (compared to the non-thermal wavepackets).

We can now compute and interfere thermal wavepackets using Eq. 3.42 and Eq. 2.58 as long as they verify the condition $|k_1| = |k_2|$. However, Eq. 2.58 does not allow us to have an analytic expression needed to give a physical understanding to the effect of temperature on wavepackets.

3.4.2 An analytic formula for $\rho_{12}(\bar{n}; x, x', t)$

Due to the increasing number of terms in the calculation of $\rho_{\mathrm{SIS}}(\bar{n}; x, x', t)$, it is time consuming to reach an analytic result. Fortunately, our formalism shows an impressive symmetry, and following the steps of Section 2.2 up to the analytic equation Eq. (2.58) we can actually make a straightforward guess on $\rho_{12}(\bar{n}; x, x', t)$ of

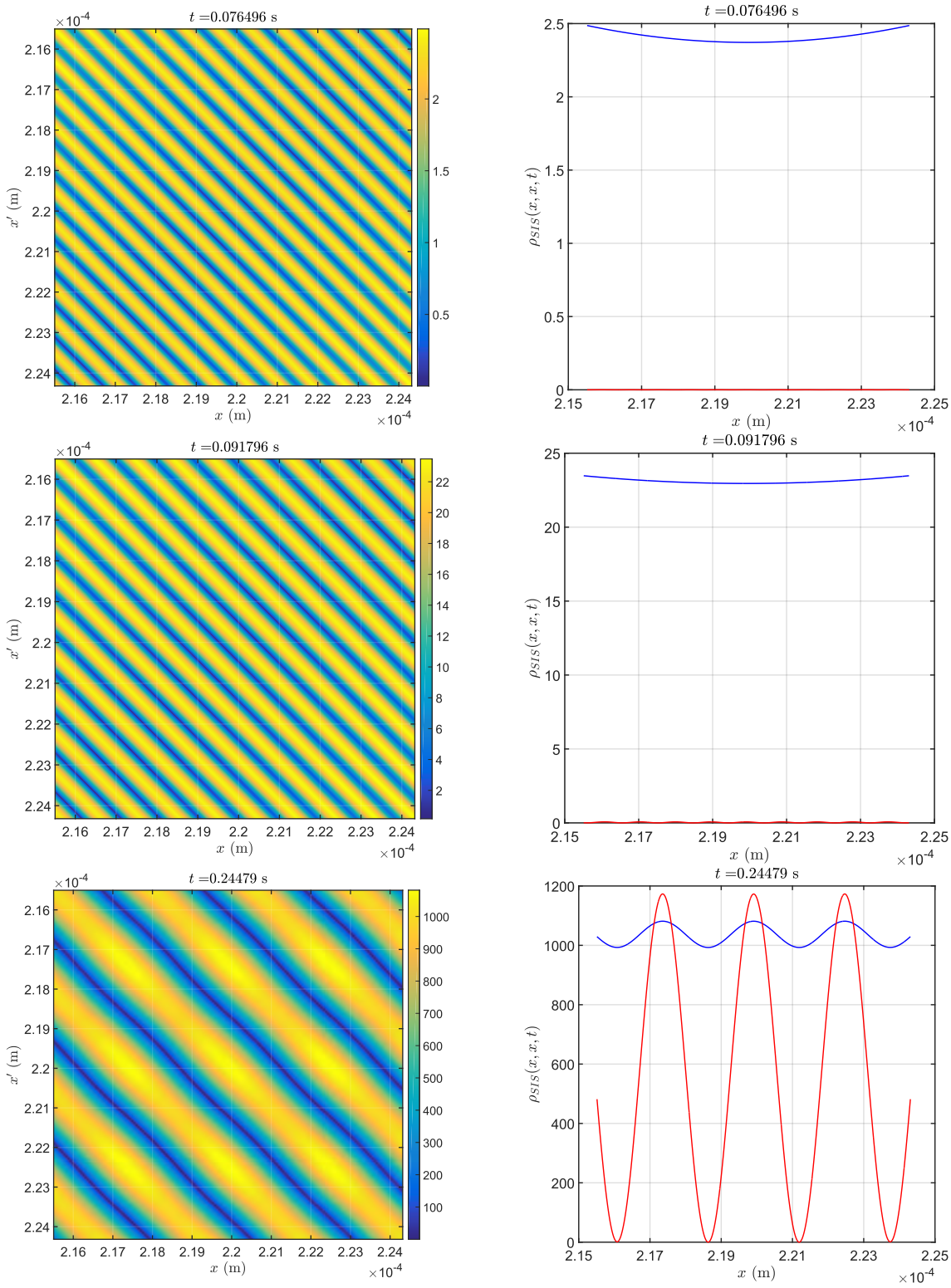

Figure 3.5: Interference pattern of two static wavepackets for $\bar{n} > 0$ with $T = 5$ nK. Left column, we have plotted $|\rho_{\mathrm{SIS}}(\bar{n}; x, x', t)|$. Right column, we have plotted $\rho_{\mathrm{SIS}}(\bar{n}; x, x, t)$ in blue and $\rho_{\mathrm{SIS}}(0; x, x, t)$ in red. We used the parameters in Tab. 3.1. We can clearly see a loss in contrast from Fig. 3.4, as well as a an 'offset' due to a higher diagonal spreading.

Eq. (3.42):

$$\rho_{12}(\bar{n};x,x',t) = \\ \frac{1}{\sqrt{2\pi}\,\Delta x_{\bar{n}}(t)}\exp\left[-\frac{([x-(x_+ + v_+t)]+[x'-(x_+ + v_+t)])^2}{8\Delta x_{\bar{n}}(t)^2}\right] \\ \times \exp\left[-\frac{([x-x']-2[x_- + v_-t])^2}{8\Delta x_{\bar{n}}^-(t)^2}\right] \\ \times \exp[ik_1(x-x_1)-ik_2(x'-x_2)]\exp\left[2i\frac{v_\Delta t}{\Delta x(0)}\right. \\ \left.\times \frac{\Big([x-(x_+ + v_+t)]+[x'-(x_+ + v_+t)]\Big)\Big([x-(x_- + v_-t)]-[x'+(x_- + v_-t)]\Big)}{8\Delta x(t)^2}\right], \tag{3.43}$$

Let us note that we have not touched to the phase as it was shown in Eq. (2.58) that the temperature has no effect on the phase. Therefore we can now write $\rho_{\text{SIS}}(\bar{n};x,x',t)$ using Eq. (3.14) as follow:

$$\rho_{\text{SIS}}(\bar{n};x,x',t) = \frac{1}{\mathcal{N}}(\rho(x_1,k_1,\bar{n};x,x',t)+\rho(x_2,k_2,\bar{n};x,x',t)+[\rho_{12}(\bar{n};x,x',t)+\text{h.c. }]). \tag{3.44}$$

We can then compare Eq. (3.42) to Eq. (3.44) and see if our expectation meet the reality in Fig. 3.6. We can see that the plot of Eq. (3.44) coincide perfectly with Eq. (3.42). Therefore, we can have a pretty high confidence in Eq. (3.44). Furthermore, in Fig. 3.6, we present times which are not presented in Fig. 3.4 and Fig. 3.5. We can see how the thermal wavepakets dominate at small t, this is due to a faster spreading than non-thermal wavepackets. Moreover, we can see that at longer t, the contrast of thermal fringes actually increases, this is probably due to the time dependence of $f(t)$ (as you can see in Fig. 3.3).

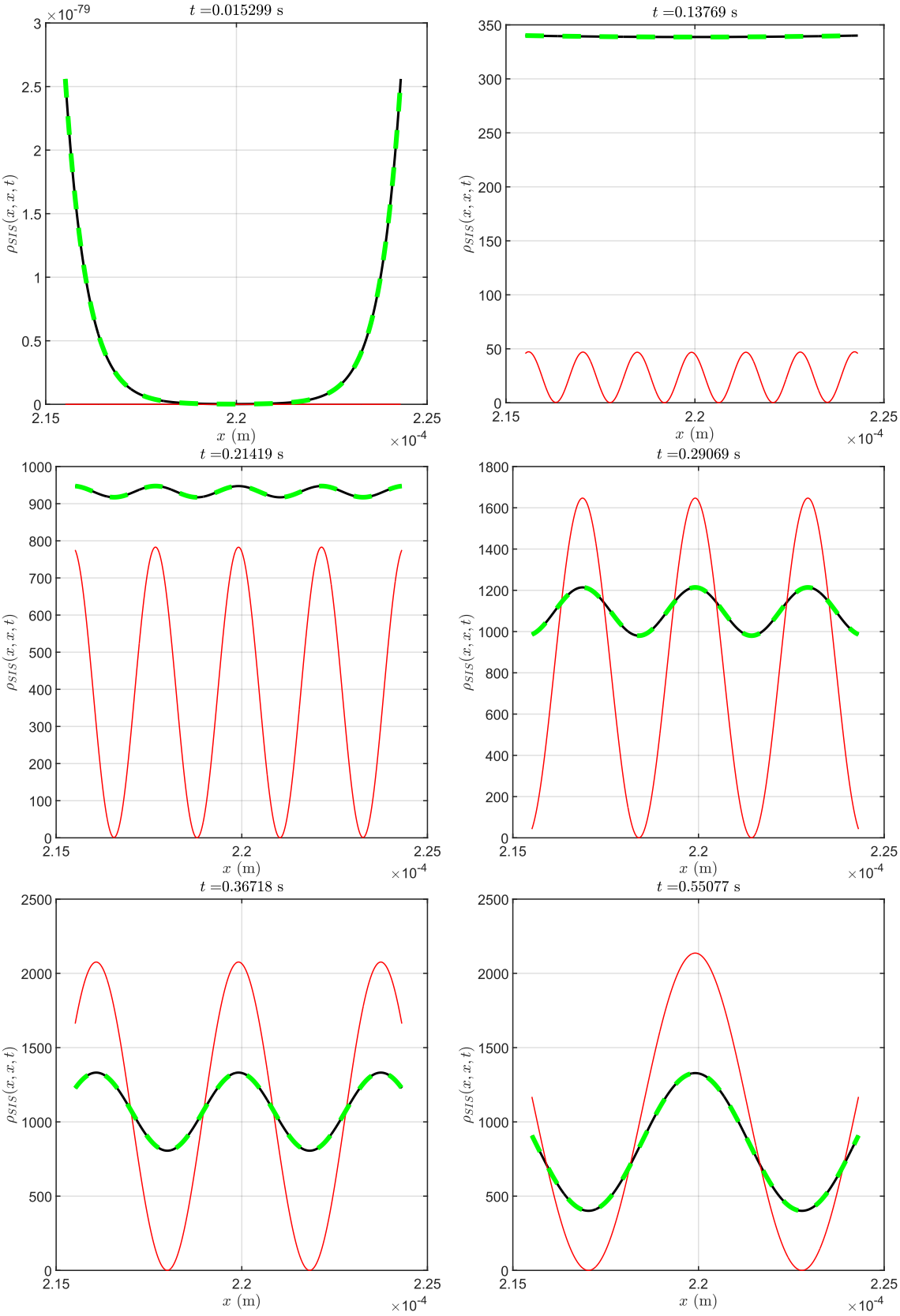

Figure 3.6: Comparison of the interference fringes between non-thermal wavepackets, thermal wavepacket calculated by matrices and thermal wavepacket analytic form. In black: Eq. (3.42), in dashed green: Eq. (3.44) and in red: Eq. (3.30).

3.5 Contrast and conclusion

We can now extrapolate Eq. (3.30) to $\bar{n} > 0$ by using Eq. (3.44):

$$\begin{aligned}\rho_{12}(\bar{n}; x, x', t) + \rho_{12}(\bar{n}; x, x', t) = \\ &\frac{1}{\sqrt{2\pi}\,\Delta x(t)} \exp\left[-\frac{([x-(x_+ + v_+ t)] + [x'-(x_+ + v_+ t)])^2}{8\Delta x_{\bar{n}}(t)^2}\right] \\ &\times 2\exp\left[-\frac{(x-x')^2 + 4(x_- + v_- t)^2}{8\Delta x_{\bar{n}}^-(t)^2}\right] \exp\left[i(x-x')(k_+ + C(x,x',t))\right] \\ &\times \cosh\Bigg(\frac{(x-x')(x_- + v_- t)}{2\Delta x_{\bar{n}}^-(t)^2} \\ &\qquad + i(k_-[x+x'] - 2[k_+ x_- + k_- x_+]) - i(2C(x,x',t)[x_- + v_- t])\Bigg).\end{aligned} \tag{3.45}$$

Therefore, our long awaited contrast term η, can be expressed by:

$$\boxed{\eta(\bar{n}, x_-, v_-, t) = \exp\left[-\frac{(x_- + v_- t)^2}{2\Delta x_{\bar{n}}^-(t)^2}\right]}. \tag{3.46}$$

It is obvious now that the contrast decreases with an increasing temperature. Furthermore, the effect of temperature on the contrast is exactly the same as on the coherence of density matrix as both are effected by $\Delta x_{\bar{n}}^-(t)$ in the same way (see Eq. (2.58)). However, the effect of temperature on the contrast can be compensated (up to a certain limit) by the choice of experimental parameters (x_- and t) for a given trap frequency ω, indeed, at longer times t, $\Delta x_{\bar{n}}^-(t)$ increase and the contrast converge to 1. Therefore, an experimenter can adjust the time window of its measurement in order to measure fringes at a given temperature T (as you can see in Fig. 3.6), however, the density $\hat{\rho}_{\text{SIS}}$ will drop (and converge to 0 in an infinite space) as the wavepacket keep spreading in the whole space, which will limit the experimenter capacity to compensate the effect of temperature on the contrast.

Moreover, the model we have presented can be used, as it is, for cases where the interfering wavepackets have a momentum, which was not discussed in this chapter. Indeed, once considering momentum, the problem increases in complexity. For example, we assumed here that the momentum would have the same norm, but it is not the case if we want to apply this model for cold atom interferometry. Indeed, most of the beam-splitter pulse used are not perfect and can generate clouds with

a non-symmetrical momentum [33, 45]. In Ref. [38], a pulse sequence is discussed for a rotation measurement in a ring waveguide using double Bragg diffraction [46]. The first $\pi/2$-pulse would split a standing wavepacket into clouds with symmetric momenta, our model was actually true for this first $\pi/2$-pulse. However, a second $\pi/2$-pulse would recombine the two symmetric clouds into 3 clouds. A standing cloud and again two clouds with symmetric momenta. It is by accessing the population ratio of those 3 clouds that a Sagnac interferometer is realized and inertial rotation measured. Further work on this thermal wavepacked model would allow us to access those conditions and study the effect of temperature on an inertial sensing measurement.

Chapter 4

Atom-chip fabrication

So far, we have discussed the propagation of a thermal wavepacket in a 1D free space as an approximation of a ring waveguide without even discussing the waveguide itself. This thesis focuses on the case of a magnetic waveguide generated by micro-fabricated wire on an atom chip. Therefore in this chapter we will look at the fabrication of an atom-chips for the experiment at SYRTE.

Atom-chips have a lot of advantages in cold atom experiments, especially in regards to size reduction, which is crucial to the integration of atomic inertial sensors within vehicles. One such advantage is, in comparison to macroscopic coils, a lower power consumption to generate important magnetic gradients for the traps, which is also crucial for integration in vehicles. This aspect forms an important part of this thesis as we will investigate current supplies for the atom-chip and the technical noise related to it (see Chapter 5). In our case, technical noise will be mainly due to current noise and wire roughness. Therefore, in this chapter, we will discuss the different processes in the fabrication of atom-chips. These are: photolithography, metal deposition (by vapour deposition or electrodeposition) and finishing processes (lift off, insulating layer, mirror), while focusing on the impact of the different fabrication steps to the wire roughness. You can see in Fig. 4.1 the different fabrication steps of an atom-chip for two different metal deposition processes with a negative photoresist method.

Benefiting from the mature technology of semiconductors and microelectronics, atom-chip fabrication can be easily done in clean rooms equipped with such technologies. L'Observatoire de Paris (who host the SYRTE) possess such a clean room,

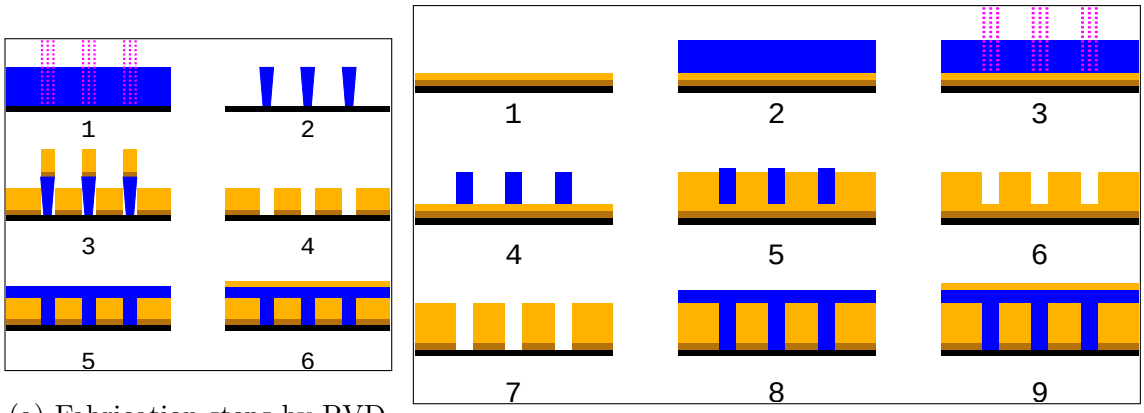

(a) Fabrication steps by PVD

(b) Fabrication by electroplating

Figure 4.1: Different fabrication steps for an atom-chip fabrication by Physical Vapour Deposition (PVD) or electrodeposition with a negative photolithography. The black represents the substrate, blue the photoresist, magenta dashes the UV light going through a mask, in yellow gold and in dark yellow titanium.

and it was decided to transfer there the atom-chip fabrication, initially done by Thales industries, to their facilities. In doing so, I was required to prepare the Observatoire's clean room in order to reproduce and, if possible, improve the atom-chips manufactured by Thales for our experiment. In Fig. 4.2 we can see the atom-chip manufactured by Thales. The chip configuration we want to achieve is a layer of gold wires upon a substrate, covered by an insulator, with a gold mirror on its top. This chip uses an Aluminium Nitride (AlN) substrate, therefore, we will discuss this choice in the next section. However, the height of the wire ($\simeq 1$ μm in Fig. 4.2) does not suit us, if we consider electrical resistivity and heat dissipation we are aiming for a 3 μm height. We will then discuss the fabrications process for such thick metal depositions, required by the application of our atom-chip.

As we will see in the following sections, I realised photolithographies and metal depositions on a Silicon (Si) substrates before working on AlN substrates. The low cost of Si substrates make it perfect to train, optimise and test any challenges and issues, not related to the substrates roughness, that could arise. Issues such as the 'step coverage' present with vapour deposition processes of thick layers, as we will see within the following sections.

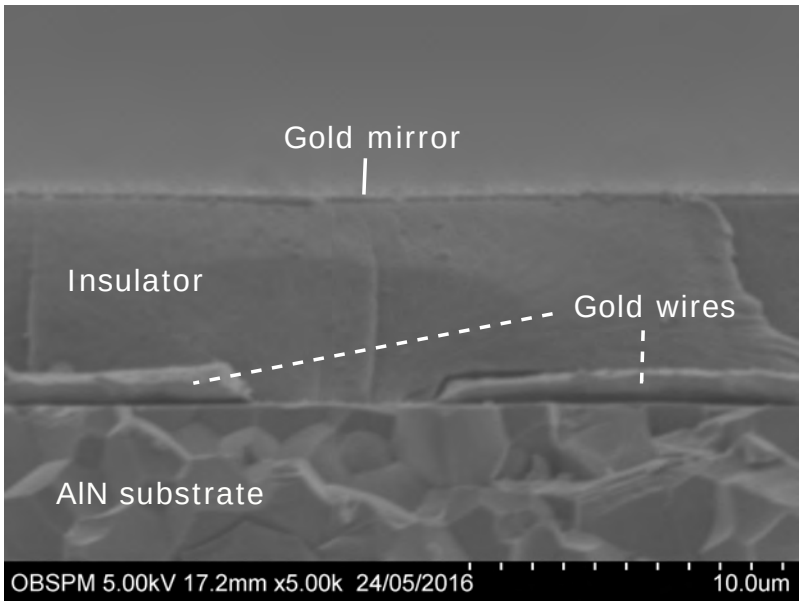

Figure 4.2: SEM picture of an atom-chip's cross section (manufactured by Thales industries). We can see the polycrystalline AlN substrate, the gold wires with $\simeq$ 1 μm height, an insulator layer (a baked polymerised photoresist) and a gold mirror on the top in order to achieve a mirror MOT.

4.1 The substrate

The substrate has to provide a robust use of our device in regards to mechanical, electrical and thermal aspects. The nature of our experiment requires the substrate to be a good electric insulator and a good thermal conductor. The two most common substrates for atom-chips are Si substrates with a layer of Silicon Oxide (SiO_2) as an electric insulator and AlN ceramics substrates. In order to avoid coherence loss due to atom-surface interaction, the atoms must remain at a certain distance from the atom-chip surface. Indeed atom-surface interactions have been measured to have a significant impact to an Na atomic beam at up to 3 μm [47]. Casimir-Polder forces limit the atom-chip's trap depth at distances less than 2 μm (for a ^{87}Rb BEC) [48]. It is commonly agreed that atoms must be at greater 10 μm distances from the chip to avoid losses due to atom-surface interaction and other technical noises [49]. At l'Observatoire, Carlos L. Garrido Alzar proposed an atom-chip design for rotation sensing [35] where the magnetic waveguide would be created 13 μm above the chip's substrate.

However, the further the waveguide is from the surface, the higher the current

required in the wire, which will create need for heat sinking. A higher current also requires a higher power from the current supplies since the micro-wires have a non negligible resistivity which depends on the wire's cross-section and length. When the total dissipated power from the wires becomes large, substrate heating effects cannot be neglected [50]. We then need to consider a substrate with a high thermal conductivity. AlN is then a better choice than Si in this regard as it has a better thermal conductivity, $170 - 280$ W/(m $\cdot$ K) for AlN as opposed to $80 - 150$ W/(m$\cdot$K) for Si[49]. In addition, AlN is a better electric insulator then Si, which requires a layer of SiO_2 (with a poor thermal conductivity) to electrically insulate the wires. With AlN, the wires can be directly in contact with the thermal conductor, instead of a SiO_2 layer, improving therefore the heat transfer. However AlN, being a polycrystalline ceramic, has a surface roughness typicaly < 40 nm (after polishing) which will never achieve the quality of a mono crystal Si substrate (typically $<$ 0.5 nm of roughness) and will still show isolated defects on the micrometer scale [49]. You can see in Fig. 4.3 different pictures of AlN substrates seen through both a microscope and a Scanning Electron Microscope (SEM). In Fig. 4.3a micron sized defects can be observed, these are holes on the surface of the substrate which can be critical for metal depostion if such a defect is located on a micron sized wire's position (these holes can also be seen in Fig. 4.5 and Fig. 4.9). AlN surface roughness actually represents a significant challenge to building structures of size < 10 μm [49], however, it is a challenge that needs to be addressed.

Let us note, however, that the perfect choice for our application would be a type IIa diamond substrate with a thermal conductivity of 2300 W/(m$\cdot$K) at 300 K [51]. There is indeed some advancement being made on diamond substrates, however, its cost is still significant. Actual "cheap" fabrication processes for diamond in MEMS technology will produce UltraNanoCrystalline Diamond (UNCD) thin films on a chosen substrate. This technology could be applied to atom-chips, it will however not solve the issues relating to surface roughness as with AlN substrate. Indeed, there is a relation between grain size and conductivity in a polycrystalline structure [52]. It seems that for polycrystalline substrates, a compromise between surface roughness and thermal conductivity, both of which relate to the grain size, needs to be considered. Therefore the heat conductivity of UNCD rapidly drops from

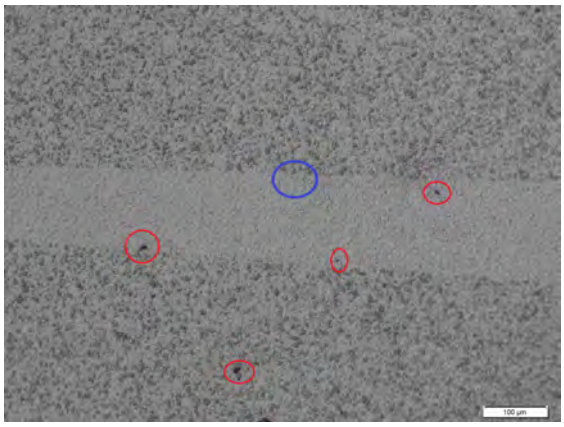

(a) AlN surface by optical microscope. Scale indicate 100 μm.

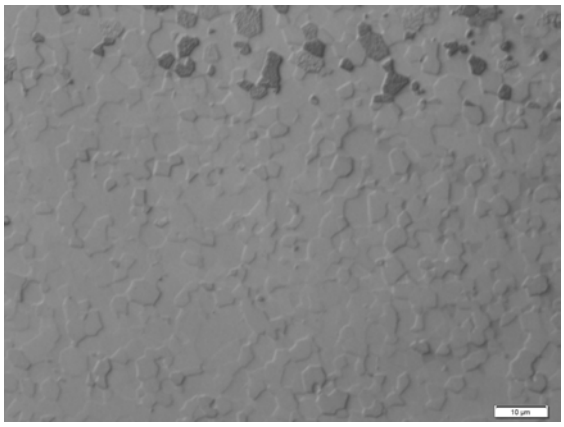

(b) Zoom on the blue circle of (a). Scale indicates 10 μm.

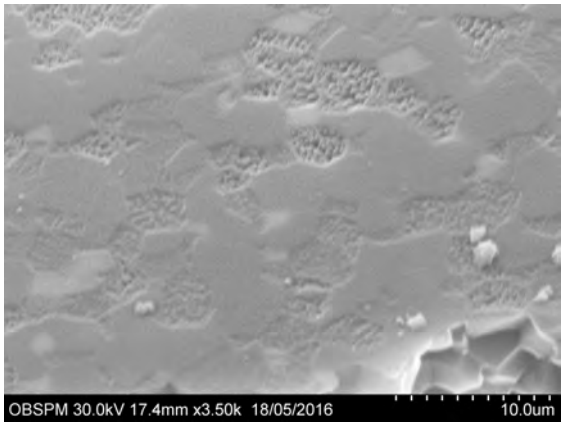

(c) AlN by SEM. Exposed substrate surface from Thales' atom-chip.

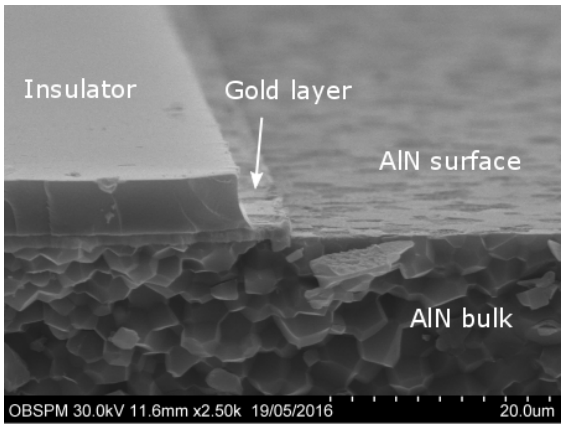

(d) Cross sectional view by SEM of Thales' atom-chip with a surface view.

Figure 4.3: (a) and (b) are the picture of a substrate used to charaterise the photolithography process while (c) and (d) show the substrate of an atom-chip manufactured by Thales. In (a), red circles represent microsized defects (holes). In (b) we see a zoom of (a) on the blue circle. The color difference follows a photolithography process that was totally removed, the white part was exposed to UV light. In (c), the defect we see in the lower right corner is due to the cleavage of the atom-chip. In (d), we have a view of the AlN surface and the polycrystalline bulk.

the known conductivity of diamond (2300 W/(m $\cdot$ K)) to 300 W/(m $\cdot$ K), as it was experimentally measured for a 1.35 μm thick UNCD Aqua 100 [53], this thermal conductivity value may increase for thickness $>$ 1.35 μm as here the thickness is in the order of the UNCD grains (a theoretical value of $800-900$ W/(m$\cdot$K) is expected to 5 μm UNCD Aqua 100 [53]). In such cases the cost difference to AlN may not

be worth the gain in thermal conductivity. Nevertheless, there are current efforts working on achieving (commercially viable) mono-crystal substrates for both AlN and diamond with important exciting results [54, 55, 56, 57]. Indeed, mono-crystal AlN substrates are starting to be commercialized, but still limited in physical size (and at important prices). Still, such breakthrough technologies would have a big impact on atom-chip fabrication and application. Thankfully, even without mono-crystal AlN substrates, there is a way to reduce the impact of the roughness of the wires on trapping fields by giving special care to the photolithography part of the process.

4.2 The photolithography

The photolithography is a corner stone process for all the different branches of microfabrication and nanotechnologies. Being a mature technique, photolithography gives an incredible amount of possibilities for anyone who wants to fabricate atom-chips [49, 58]. The basic idea is to transfer the pattern from a mask to a photoresist layer (upon a substrate) through optical exposure (generally UV light, depending of the photoresist sensitivity) and then chemically develop the pattern. Then, the exposed subtrate will be etched or processed according to its need. In our case, the developed photoresist will reveal a negative picture of our mask, as you can see in Fig. 4.4, and metal will be deposited on the exposed substrate. A lift-off process will then dissolve the polymerised photoresist and the metal remaining will be a reproduction of our mask pattern (Fig. 4.4). The quality of the photolithography is crucial for the atom-chips as we need to reproduce the mask pattern with fidelity, but we also need to guarantee that the slope at the edge of our deposited wires is as vertical as possible. A cross-section of our wires needs to reveal a rectangular profile instead of a trapezoid profile. It has indeed been shown that the roughness at the edges of a wire is the main contributor to the magnetic potential roughness [59, 60]. In Fig. 4.1, we can see our processes for a negative photolithography followed by the different processes depending of the kind of metal deposition. We want to realize (steps 1-2 in Fig. 4.1a and steps 2-4 in Fig. 4.1b).

The negative photolithography consists of deposition by spin coating a layer of

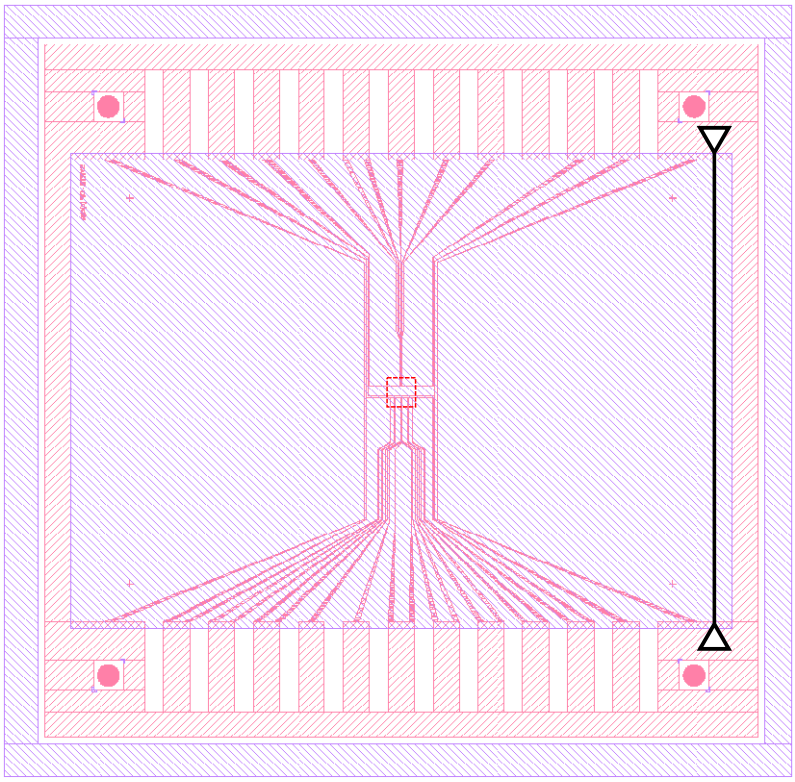

(a) Schematic of the pattern of the wires. The black line represents a scale of $\simeq 3.5$ cm.

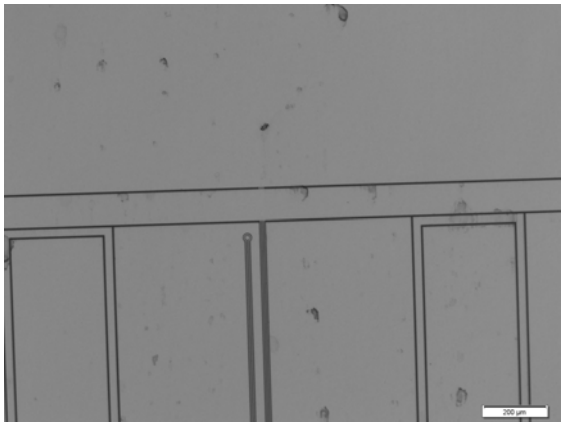

(b) Picture of the mask on the red rectangle of (a). Scale indicate 200 μm.

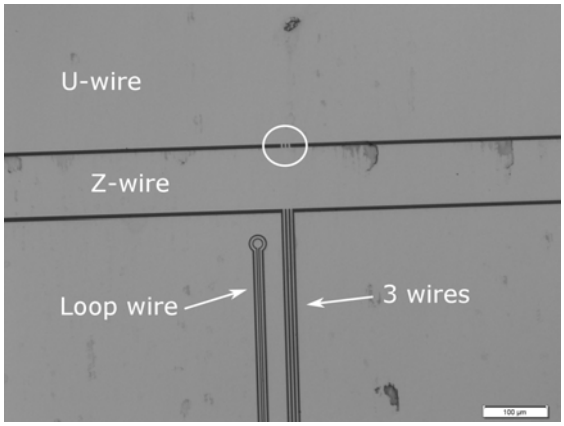

(c) Zoomed picture by optical microscope of (b). Scale indicates 100 μm.

Figure 4.4: In (a), wire pattern used in the mask for the photolithography present in this thesis. The black line represents the dimension of the insulating layer on top of the wires. In (b), the scale represent 200 μm, picture of the mask using a microscope on the region of the red rectangle in (a). In (c), the scale represent 100 μm, we zoom on (b) in order to see the 3 wires which will be used to generate a waveguide and which are in contact with the U and Z wires as you can see in the white circle, the loop wire is an antenna that can be used to add phase shift to the atoms in one arm of a linear waveguide in future experiments.

photoresist (AZ nLOF 2070), then we soft-bake it at 110°C (step 2 in Fig. 4.1b). We expose the photoresist to UV light (320 nm) through our mask (step 1 in Fig. 4.1a and step 3 in Fig. 4.1b), then we do a post-exposure baking at 110°C, the exposed photoresist is then polymerised and hardened. Then, by using the developer (AZ 826 MIF), the unpolymerised photoresist will dissolve, leaving only the UV exposed photoresist as a negative picture of our wires pattern [58] (step 2 in Fig. 4.1a and step 4 in Fig. 4.1b). It it by setting the correct combination of times for UV-light exposure and development bath that we are able to to select a profile shape for the photoresist's negative pattern. As you can see in Fig. 4.1, the photoresist's profile needs to be adapted to our metal deposition methods. Moreover, during the developer bath, it is important to give some agitation to the solution in order to avoid concentration gradient in the developer due to the dissolution of the unexposed photoresist. This matter can be critical to the development of small patterns (3 wires, loop wire). This agitation, depending to the photoresist's adhesion to the substrate surface, may destroy high aspect ratio structures. Indeed, since the photoresist layer is $\simeq$ 6 μm, then the pattern relating to the loop wire shows the highest aspect ratio profile (6 μm for 2 μm), it is subject to high tensions and can easily collapse at too vigorous agitations, as you can see in Fig. 4.5 on AlN. The same would occur with Si but with lesser sensitivity to the agitation.

I achieved this process on Si substrates and AlN substrates. We can see the result of those photolithographies in Fig. 4.6. The photoresist profile does not have the same requirements for PVD and electrodeposition, a PVD requires an under-cut profile in order to be dissolved after the deposition while the ectrodeposition need to match the intended wires profile (see Fig. 4.1). Once the photolithography is done, we can follow up our process with the metal deposition.

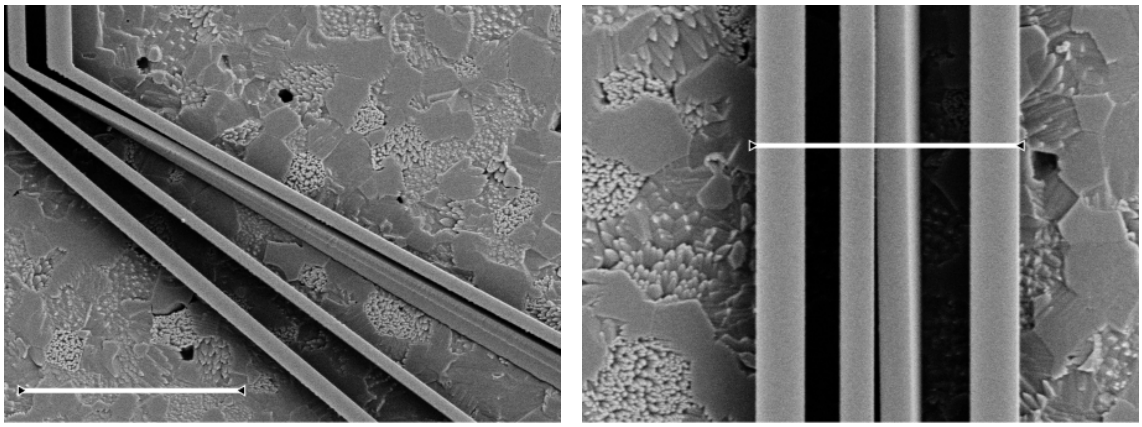

(a) Collapsed photoresist strip for the loop wire, far from the loop region. The white scale is 29 μm.

(b) Bended photoresist strip for the loop wire, close to the loop region. The white scale is 19 μm.

Figure 4.5: SEM image of the collapse of a photoresist strip related to the loop wire due to agitation and a high aspect ratio. In (a), we see the collapse at the junction between the wire sized pattern and electrode pattern used for the atom-chip connection. In (b), we see that the strip collapse propagate tension in the strip making it bend in a region close to the loop.

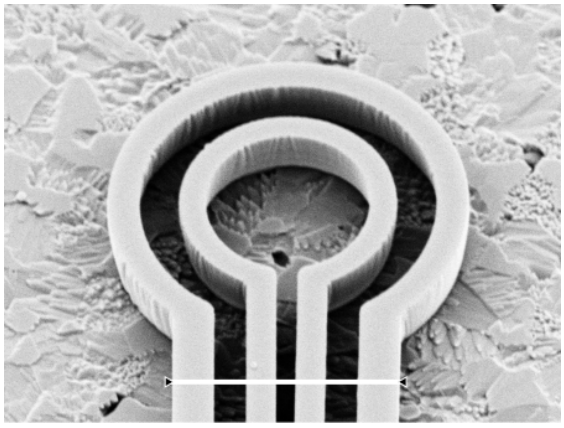

(a) Photolithography on AlN for the loop wire. White scale is 19 μm.

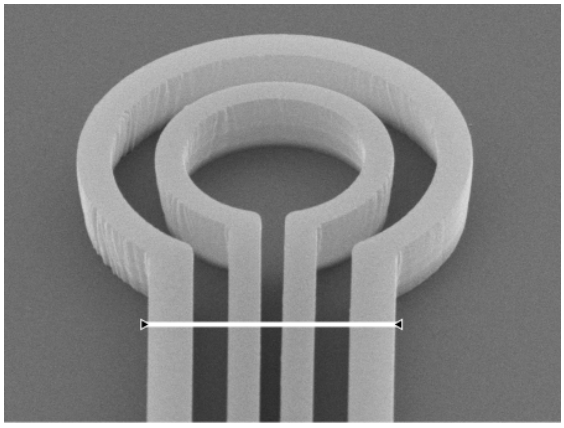

(b) Photolithography on Si for the loop wire. White scale is 19 μm.

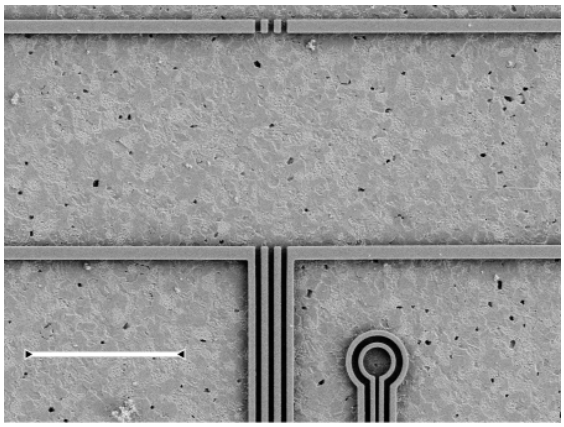

(c) Top view of a photolithography on AlN. The white scale is 71 μm.

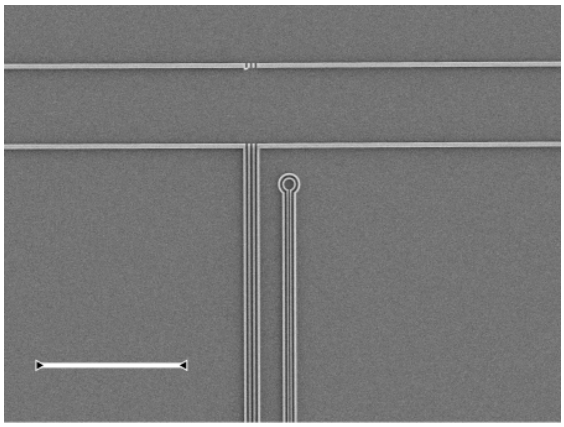

(d) Top view of a photolithography on Si. The white scale is 183 μm.

Figure 4.6: SEM images of photolithographies on AlN ((a) and (c)) and on Si ((b) and (d)). (a) and (b) show the negative loop wire with a tilted view to appreciate the 3D structure. (c) and (d) show the top view of the region corresponding to the red rectangle in Fig. 4.4a.

4.3 Metal deposition

It is through metal deposition that we will create a wire circuit to generate magnetic potentials. As we have discussed in the previous sections, our goal is a thick metal deposition, for heat dissipation and power consumption reasons, with a cross section as close as possible to rectangular. The grain size needs to be as small as possible such that the metal deposition does not increase the surface roughness. Two process are tested and investigated in this section. The physical vapour deposition (PVD) process, known to give the best surface quality for the wire circuits and the electroplating, an economical process which can easily achieve thick depositions. One problem with electroplating is that it can also produce cavities inside the wires [61] and have a surface roughness far more significant than vapour deposition, possibly deterioring the surface roughness compared to AlN substrates.

4.3.1 Physical Vapour Deposition (PVD)

We used a physical vapour deposition (PVD), a method to deposit matter on a target via evaporation [62] (step 3 in Fig. 4.1a). We deposited aluminium (Al) on a Si substrate in order to test the capacities of thick deposition with PVD. Then we deposited gold on the AlN substrate to see the impact of the surface roughness on the depositions. You can see a PVD chamber in Fig. 4.7, it is basically a vacuum chamber where a crucible (made of tungsten) loaded with matter faces our target which is positioned over the crucibles. A high current is then passed through the crucible until the matter inside the crucible is first melted then evaporated, creating a cone shaped vapour beam in the vacuum that will directly hit the target. We first deposit a layer of titanium (Ti) which has excellent adhesion properties and will efficiently stick to the substrate, allowing the our chosen metal to grow on it. Then we start the deposition of our chosen metal, Al or Au, which will adhere to the Ti layer. The metal vapour cone hits the target and will deposit the matter over all surfaces directly facing the crucible. Therefore, in this method, there is no need for us to have vertical profiles for the photoresist as the incident angle of the vapour cone is what is more crucial for us. However, since the metal also grows on the photoresist, there is actually a need to have an under-cut profile for the

lift-off process, as you can see in steps 2-3 of Fig. 4.1a. Still, thick deposition is more challenging in this case as the finite size of the crucible gives us a limit on the thickness we can achieve in one PVD. Indeed, in order to realise thicker deposition, the PVD chamber needs to be opened several times in order to reload the crucible. By opening the vacuum chamber we may introduce impurities inside the wires, this can actually be seen with Al deposition in Fig. 4.8 (and Fig. 4.10) through oxidation blisters on the top of the wires. Thankfully, the chemical inertness of gold allows us to not worry too much about contaminations as it the noblest metal [63].

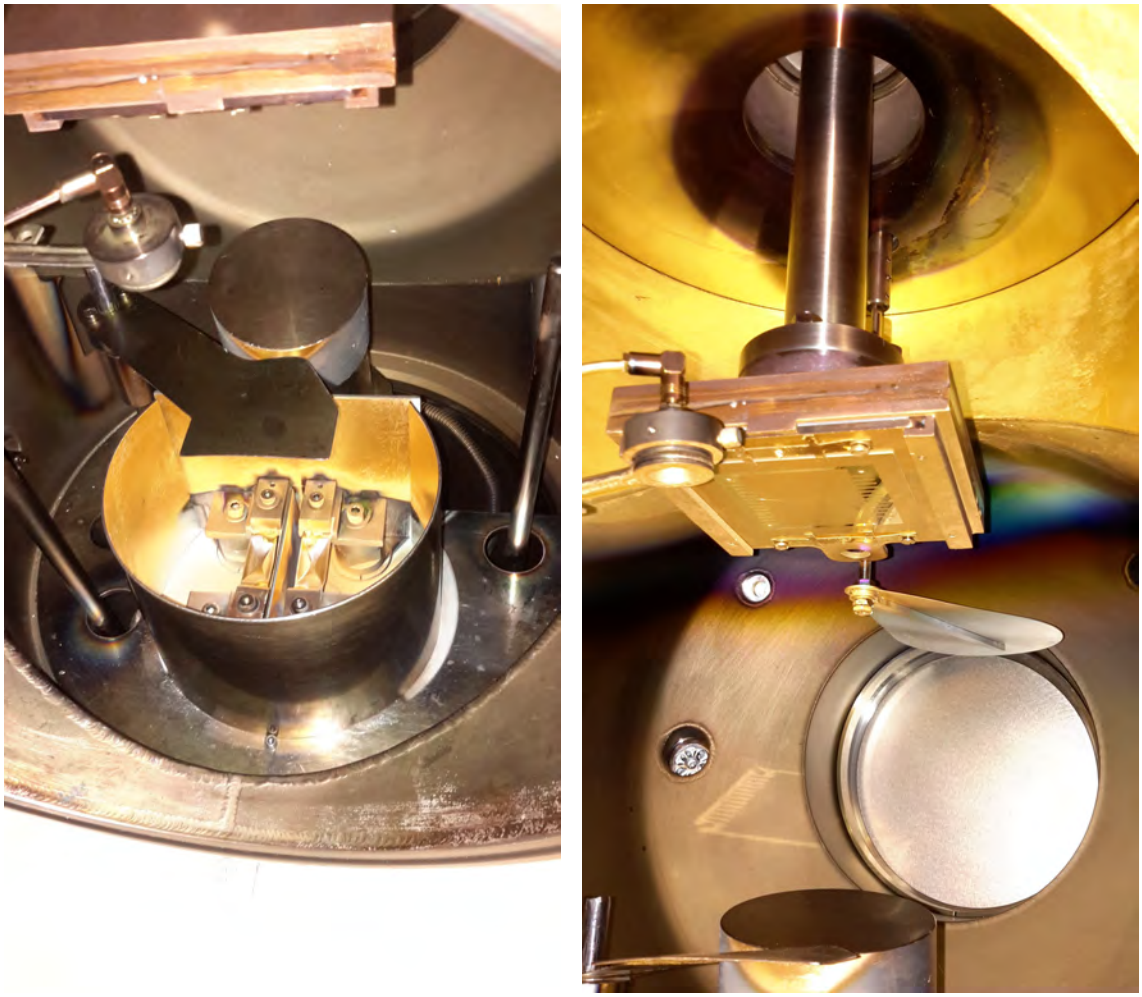

(a) Picture of the crucibles inside the PVD chamber.

(b) Picture of the deposition target inside the PVD chamber.

Figure 4.7: Pictures of the PVD chamber. In (a), we see two crucibles that were previously loaded with gold. In (b), we see the target (a photolithography on an AlN substrate) on top of the crucibles. The result of this PVD can be seen on Fig. 4.9.

I then tried thick deposition of Al on Si substrate by PVD, as you can see in Fig. 4.8 for deposition heights of $\simeq$ 2 μm, I achieved the deposition on a static target (Fig. 4.8a and Fig. 4.8c) and on a rotating target (Fig. 4.8b and Fig. 4.8d. In Fig. 4.8a and Fi. 4.8c, we can see different layers for a static target PVD due to the different positions of the two crucibles (seen in Fig. 4.7). We also see a significant roughness on the edges of the wires, we believe it to be mostly due to the metal growing on the photoresist. However, we see for a rotating target, that the different metal layers and the edge roughness disappears. Furthermore, the profile slope seems more significant than with the static target deposition. The PVD on the rotating target was realised with Al on Si substrates (Fig. 4.8b and Fig. 4.8d) and also with gold on a used AlN substrate that showed a high surface roughness (compared to a unused polished AlN substrate) as you can see in Fig. 4.9. At the end of this PVD characterisation, my first field mission at SYRTE was done (a second field mission will focus on electrodeposition). Using my PVD characterisation and my work on photolithography, an atom-chip was fabricated on an unused and polished AlN substrate and is now in the experiment's vacuum chamber at SYRTE (presented at the end of the chapter in Fig. 4.17).

However, using PVD method, we would have a limit on the wires' height due to the pattern sizes of the circuit we want to deposit. Indeed, with the vapour deposition process, the metal is deposited everywhere, even on the top of the photoresist. However the metal will not grow purely vertically on the photoresist's edge, as you can see on Fig. 4.10. This is known as step coverage [64, 65], and it has an important impact when the deposited thickness is of the same order as the gap you are trying to fill. This led, in our case, to reduce the gap between the negative photoresist structure seen by the vapour cone and to give an important slope at the edges of our wires (until the gap is totally closed for the 3 wires or the loop wire for example). This ultimately fixes a maximum height to our wire and make it impossible to grow vertical profiles for thicker depositions. Therefore, in order to realise thick vapour depositions with vertical profiles, we need to find a way to overcome the issue related to the step coverage of the protoresist. Meanwhile, we will explore another metal deposition process: electrodeposition.

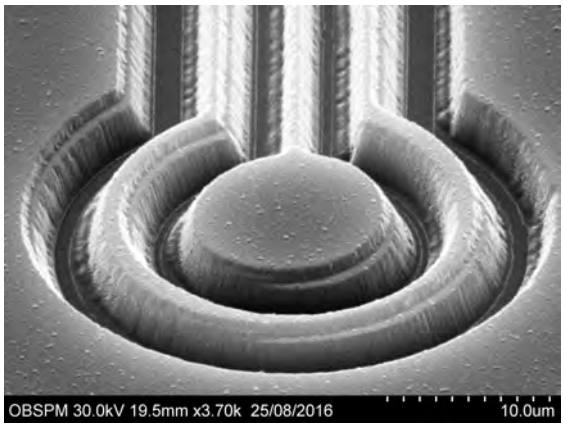

(a) PVD on a static target. SEM image of the loop wire.

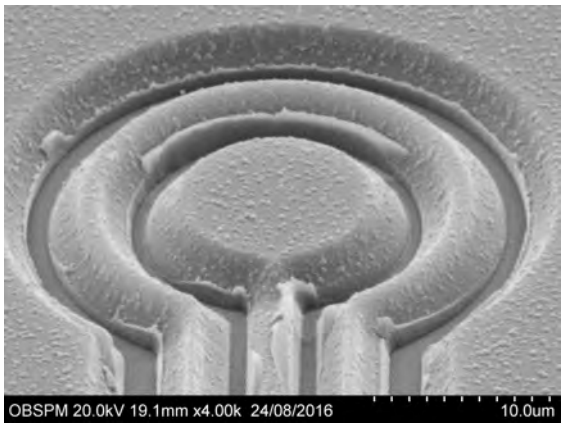

(b) PVD on a spinning target. SEM image of the loop wire.

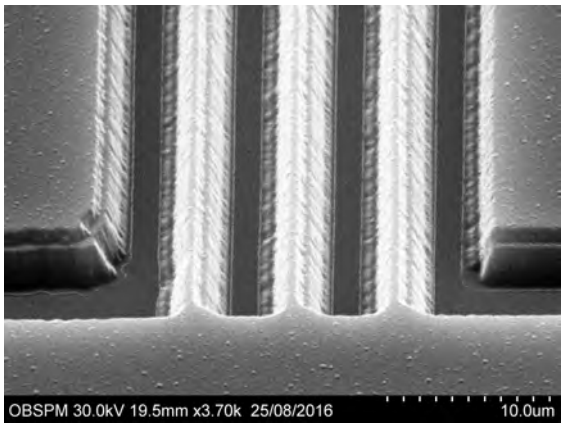

(c) PVD on a static target. SEM image on the 3 wires.

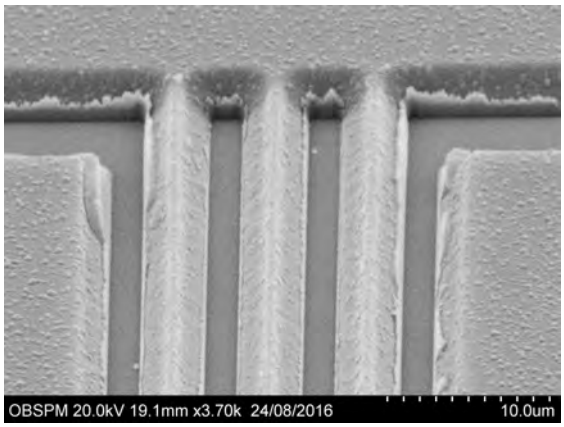

(d) PVD on a spinning target. SEM image on the 3 wires.

Figure 4.8: SEM image of two atom-chip prototypes done by Al PVD on a Si (2 μm thick). We see the result of two different techniques where the target is static ((a) and (c)) and rotating ((b) and (d)). Both techniques gives different output in term of edge slope, surface roughness and metal purity (due to the oxidations blisters on the Al due to vacuum quality).

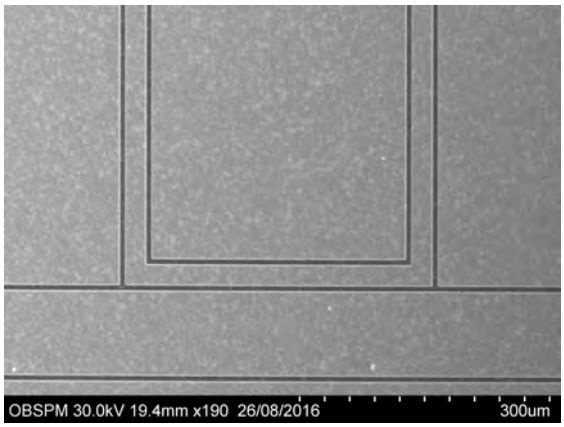

(a) SEM image on a small U wire of a gold PVD on an AlN substrate.

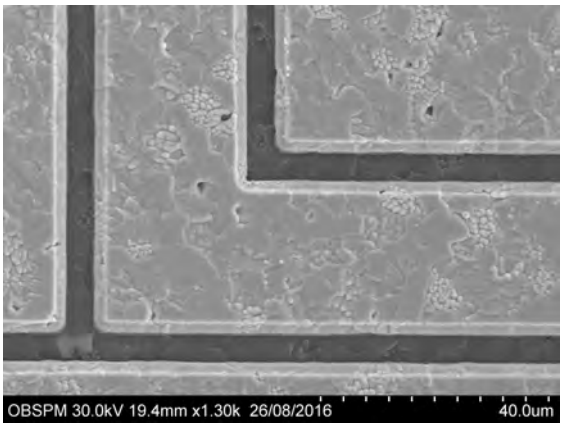

(b) Zoom of (a) on the left lower corner of the U wire.

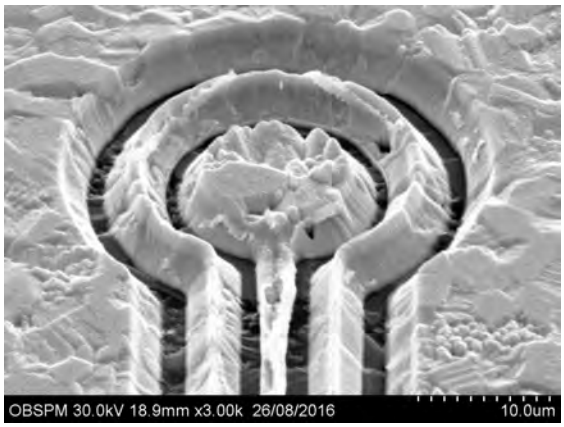

(c) SEM image on the loop wire of a gold PVD on an AlN substrate.

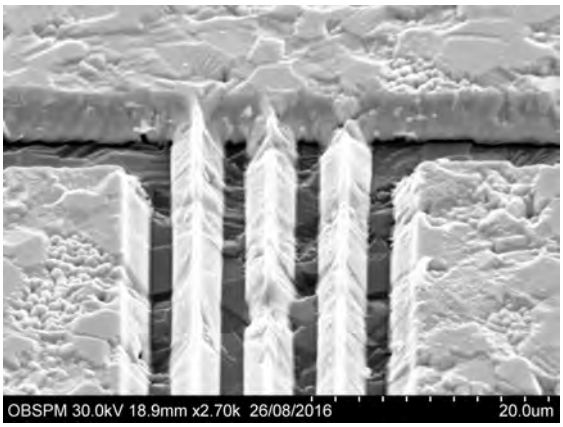

(d) SEM image on the 3 wires of a gold PVD on an AlN substrate.

Figure 4.9: SEM images of a gold PVD on an AlN substrate, we can see that the PVD reproduce with high fidelity the surface roughness of the AlN substrate. In (a), a small U wire that you can see in Fig. 4.4b. In (b), zoom on (a), you can see that the gold layer reproduce with fidelity the AlN roughness. In (c) and (d), you can see the ALN roughness have huge consequences on structures of few μm.

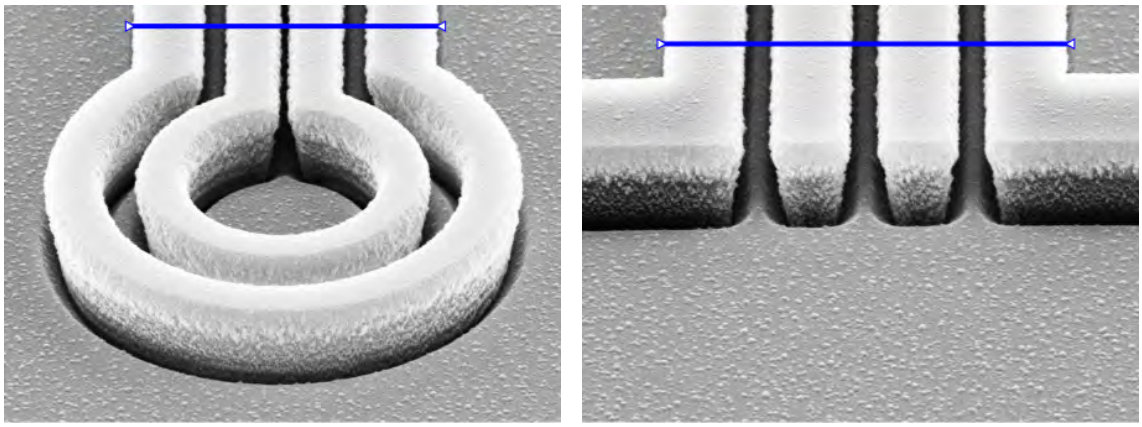

(a) SEM image on the loop wire of a PVD before the lift-off. Blue scale is 20 μm.

(b) SEM image on the 3 wires of a PVD before lift-off. Blue scale is 23 μm.

Figure 4.10: Result of a PVD (Al on Si substrate) on a spinning target before the lift-off. In (a), we see the loop wire and in (b) the 3 wires connecting to the Z wire. Let us note the step coverage, we clearly see the metal growing on the photoresist with a porous layer of metal growing on the under-cut profile.

4.3.2 Electrodeposition: expectations

In term of grain size and surface roughness, electrodeposition cannot beat PVD, the only limiting factors for PVD is the photolithography quality and the substrate roughness. By any means, electrodeposition cannot beat PVD's surface roughness as the metal is grown over a seed layer produced by PVD, as you can see in step 1 of Fig. 4.1b. In micro-fabrication, every growing process deteriorate the surface roughness or at best copy it, there is only one way to reduce a surface roughness, it is by polishing it. However, considering step coverage issues, it appears that not only we cannot achieve wires with vertical profiles using the PVD processes, additionally, the wire height in our circuit would be limited. It is common in clean rooms for microfabrication processes to use vapour depositions for thin metal films with an excellent RMS surface roughness (R_q) of $\simeq 3$ nm [66, 67], while thick deposition are achieved by electrodeposition with a surface roughness of lesser quality. We have then turned to the electrodeposition processes with the aim to achieve the smoothest surface roughness possible for our gold wires. Electrodeposition, in comparison to PVD, is less expensive (in price, energy consumption and metal mass consumption) and can perform metal deposition of several μm far easier and faster. This process is free of step coverage issues since there is no metal growing on the photoresist (as you can see in step 5 of Fig. 4.1b). The question is then: which deposition quality do we need to achieve such that electrodeposition can be competitive to PVD?

By looking at Fig. 4.9 we see that PVD will reproduce with high fidelity the AlN surface roughness, while Fig. 4.8 show us that the wire's edge roughness is affected by the quality of the photolithography. Therefore, we only need to achieve an electrodeposition quality such that we would still be limited by those factors (AlN and photolithography roughness) and do not need to reach the same quality as with PVD. Literature on this matter tends to show this objective is achievable. Indeed, Konstantin Ott in Ref. [68], achieved a gold electrodeposition on AlN substrate where he measured an arithmetical mean deviation of the surface roughness (R_a) of 28 ± 3 nm while the AlN shows an R_a of 34 ± 3 nm. Clearly, the surface roughness measured by Konstantin Ott is limited by the AlN surface roughness. Furthermore, Philipp Treutlein in Ref. [66], using the same electrolyte as Konstantin Ott, achieved an electrodeposition on a Si substrate, such that the surface roughness is not limited

by the AlN, and achieved a surface roughness $R_q = 15$ nm, a factor $\simeq 2$ below the AlN roughness measured by Konstantin Ott. Moreover, to the best of our knowledge, the best electrodeposition in term of surface roughness that can be found in the litterature was achieved by Elena Koukharenko et al. in Ref. [69] on Si substrate with a R_q of 2.3 nm, which is a surface quality that would then exceed the quality of vapour deposition. Let us note, however, that this result shows some discrepancy with later work from the same team [67], published 6 years later, they noted a surface roughness of $R_q = 3$ nm by vapour deposition, stating that vapour deposition processes exceed the quality achieved via electrodeposition.

4.3.3 Electrodeposition: the experiment

Looking at the experimental setup of Philipp Treutlein and Konstantin Ott in Fig. 4.11, we believe that there is room for improvement. It appears that the important factors to control the electrodeposition and achieve a low surface roughness are the choice of the chemical electrolyte, the control of the temperature, the control of the current surface density and the solution agitation.

The choice of electrolyte is actually discussed by Philipp Treutlein in Ref. [66] where a sulfite bath is compared to a cyanide bath used by [70], it is concluded that sulfite bath could achieve less roughness. Cyanide baths are historically the most used electrolytic bath for gold electrodeposition as they are not only cheap, but also extremely robust in use as they are resistant to changes in pH, oxidations and hydrolysis. However, their compatibility to standard photoresist and 'under-plating' (when metal grow underneath the photoresist where it is not supposed to) represents a major issue. Sulfite baths are in fact highly compatible with micro-electronic processes and are now the most used bath in this field [71]. For examples of commercial sulfite baths we have, Gold-SF from Metakem used by Philipp Treutlein and Konstantin Ott [66, 68], and Gold ECF 60, brightener E3, from Metalor [69]. While for an example of commercial example of cyanide bath example we have PurAGold 402 [70]). As in [66, 68] we will be using Gold-SF from Metakem. Metakem's sulfite bath recommends a working temperature range of 55° to 65 °C with an optimum at 60 °C. The temperature then needs to be controled and maintained during the whole process. Better temperature control is achievable through the use of a water

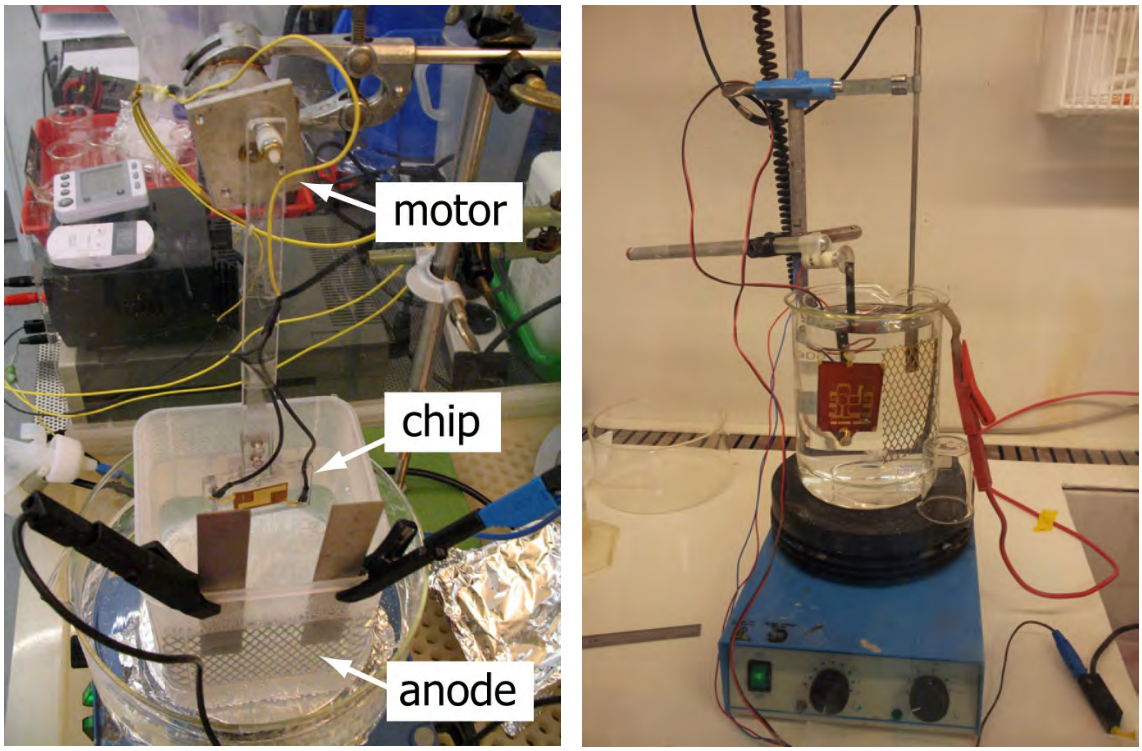

(a) Electrodeposition setup of Philipp Treutlein presented in [66].

(b) Electrodeposition setup of Konstantin Ott, with courtesy of SYRTE and Konstantin Ott.

Figure 4.11: Typical electrodeposition setup for non cyanide bath.

bath with a circulation pump rather then a magnetic stirrer with a hot plate as used in Fig. 4.11.

The most critical difference we decided to adopt from the electrodepositions of Fig. 4.11 is related to the electric contact to our atom-chip. In the electrodeposition process, the metal is deposited on the cathode, therefore in our case the cathode would be our atom-chip. In this situation the most common way to proceed is to deposit a seed layer of gold on all the substrate before proceeding to the photolithography (as you can see in Fig. 4.1b). Furthermore, how the current density is managed has a significant impact in the process, in terms of electrical contact, but also in term of time evolution of the resistivity's area density as we will evolve from a thin seed layer of gold, between 50 to 200 nm, to the targeted thickness (few μm). It is known that an inhomogeneous contact would make metal grow more significantly in the vicinity of that contact [72]. We also want to use a current generator in order to fix the current surface density, therefore we need to be sure that the metal depos-

ition is done on the atom-chip and only the atom-chip, which requires the electrical contact to not be exposed to the gold electrolyte. We can see in Fig. 4.12 how an homogeneous electrical contact to our gold seed layer is managed and sealed, with the atom-chip holder capable holding two atom-chips (one on each side). This was designed by David Holleville from SYRTE, but due to sealing stress, I decided to introduce a small cut to the rings copper contact.

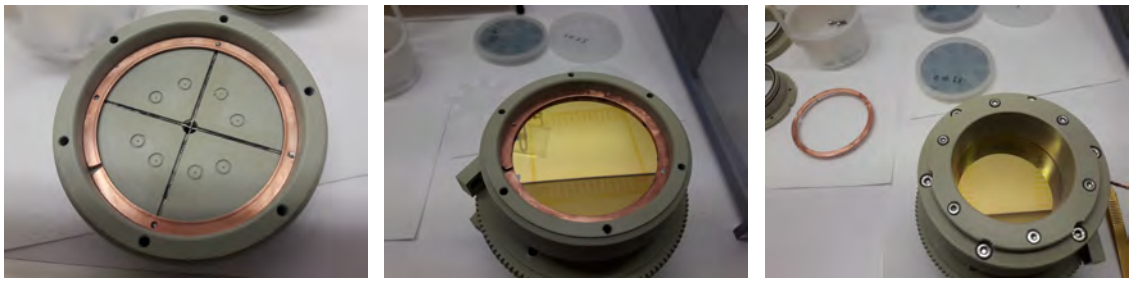

(a) Picture of the atom-chip holder for electrodeposition.

(b) Picture of an atom-chip (before electrodepostion) in the holder.

(c) Sealed holder with an atom-chip for electrodeposition.

Figure 4.12: Pictures of the atom-chip holder with a homogeneous sealed electrical contact to improve electrodeposition. In (a), we see how the electrical contact is done from the back to the top of an atom-chip positioned as in (b), then the copper contact is sealed from the electrolyte bath in (c).

Another change that we decided to take is the method used for the solution's agitation. In both electrodeposition baths of Philipp Treutlein and Konstantin Ott (Fig. 4.11), the agitation is done through a magnetic stirrer, we chose to use mechanical agitation through the use of an overhead stirrer with a propeller. There is actually several reasons for the choice of an overhead stirrer, going from commodity in terms of space with the water bath to trusting the higher efficiency of a propeller. Still, there is a question that does not seems to be addressed in the literature, in relation to electrodeposition processes applied to atom-chip fabrication using magnetic stirrers. Would the magnetic stirring field affect the quality of the deposited gold through the Lorentz force applied on the gold ions? There are studies on the effect of constant magnetic fields during electrodeposition [72, 73, 74]: those studies actually show that a constant magnetic field (around 1 T) parallel to the electrodes' electric field enhances the electrodeposition quality (in term of surface roughness

and even speed for ferromagnetic metals). There is, however, to the best of our knowledge, no study on the effect of a rotating field from a magnetic stirring on electrodeposition has been done. Although we acknowledge that the weakness of the magnetic field would probably not be enough to create a visible effect. Still, it is wiser to not introduce a magnetic field which is uncontrolled and whose effect is unknown. Moreover, an experiment without magnetic stirring would be more easily adapted to investigate gold electrodeposition in a controlled magnetic field environment.

Our experimental setup can be seen in Fig. 4.13. The electroplating frame with a sealed electric contact and a customized beaker were designed by David Holleville from SYRTE. The customized 3D printed beaker is clean room compatible as it has been recently proven that, with special care and cleaning processes, 3D printed devices can be used in clean room for semiconductors processing [75].

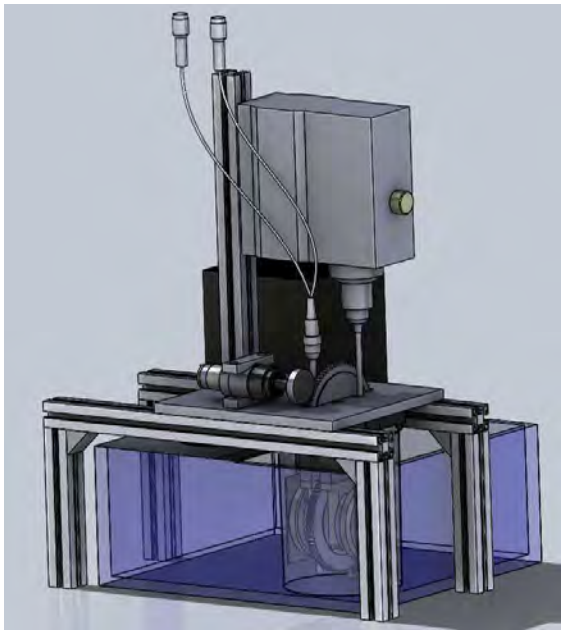

(a) Schematic of our electrodeposition setup.

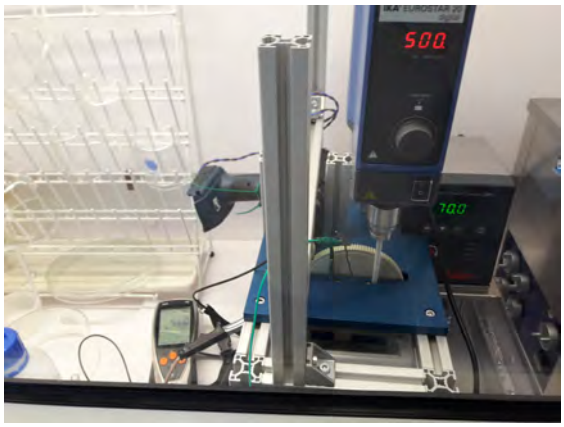

(b) Picture of our electrodepsition setup.

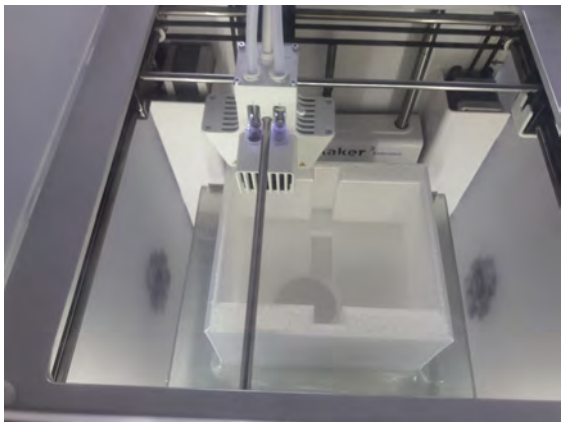

(c) The customized beaker being 3D printed.

(d) Customized beaker in the water bath before installing the electrodeposition frame.

Figure 4.13: Presentation of the electrodeposition setup designed by David Holleville. In (a), we see a schematic of the electrodeposition setup and in (b) we see its picture. In (c), we see our customized beaker matching the electrodeposition frame in order to have an effective volume of 1 L for the electrolyte bath. In (d), we see a picture of the beaker and the water bath which are below the electrodeposition frame in (b).

4.3.4 Electrodeposition: mixed result

Therefore I achieved the first 3 μm gold electrodeposition on a Si substrate. However, the resulting deposition was ultimately a failure as the deposited gold layer was covered by an unknown contaminant. We can see in Fig. 4.14a an inhomogeneous brown to black deposition on the atom-chip, and is likely to be due to a known issue of the electrolyte [76]. This issue relate to the oxidation of the additives present in Metakem's electrolyte which occurs when the electrolyte solution is exposed to air for some time but not much gold is worked out. Introducing additives could be enough to correct this deposition issue in future attempts. Another possible cause could be the 3D printed beaker, not for contaminant reasons but for the structural properties of 3D printed structures. Indeed, due to it having hollow walls the beaker acted as a thermal insulator, preventing the temperature control of the electrolyte solution beyond the recommended temperature range. However, SEM images in Fig. 4.14 shows that this brown deposition occurred only at the end of the process as we can see crystal on the top of the gold but never inside the layers seen through the edges of the wire (see Fig. 4.14c and Fig. 4.14d).

Morever, SEM images in Fig. 4.15 shows that this first electrodeposition attempt was far from being a total failure as the roughness of the gold wires is unusually low, when they are not covered by the contaminant crystals. Indeed, contaminant free gold surfaces of our wires show a surface roughness $R_q \simeq 12$ nm, below Philipp Treutlein's results ($R_q \simeq 15$ nm) and far below the AlN roughness budget ($30 - 40$ nm). Furthermore, if we look into Philipp Treutlein's electrodeposition in Fig. 4.15d, we see that the roughness on the top and on the edge of the wires is the same. We do not see such consistency between the roughness at the top and at the edges of our wires, actually it seems that the roughness at the edge of the wires is better then the roughness at their top, as you can see in Fig. 4.14d and Fig. 4.15c. Looking more in detail at Fig. 4.14d, the SEM definition cannot see a difference between the seed layer (at the bottom) and the wire's edge, unfortunately it is not possible to measure the edge's roughness with our profilometer as we did for the top of the wires. However, it is more likely that the edge's roughness is limited not by the seed layer but by the photolithography and the photoresist's roughness (which can be impressively good).

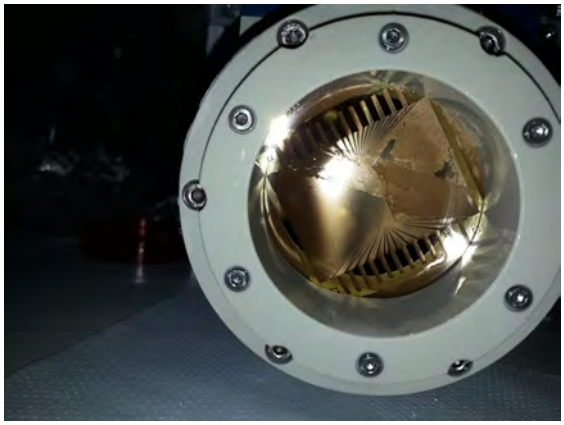

(a) Picture of the atom-chip right after the electrodeposition.

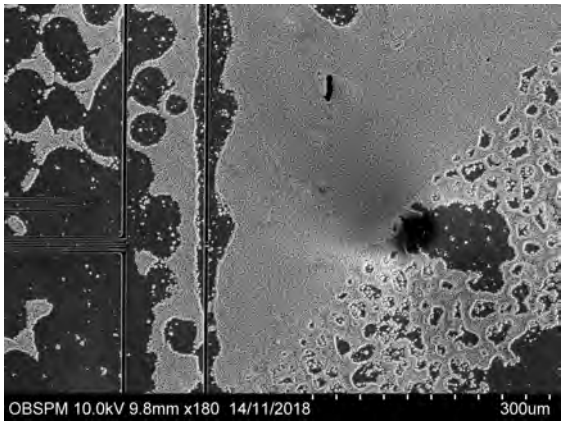

(b) SEM picture of red rectangle region of Fig. 4.4a

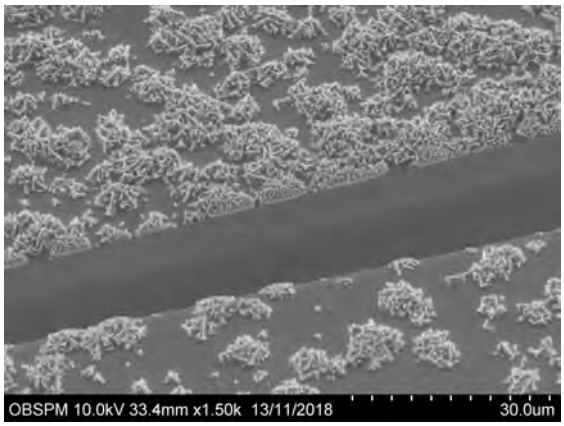

(c) SEM picture inside a wire gap.

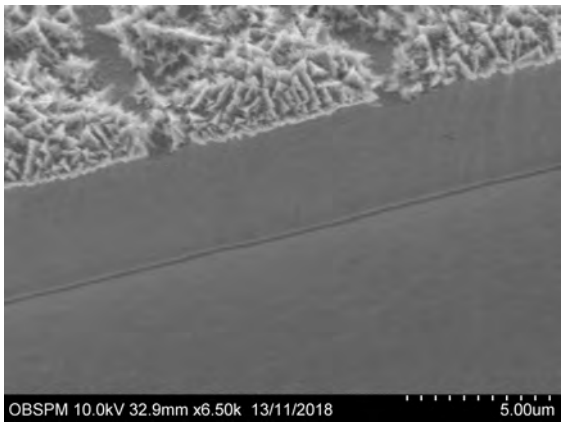

(d) Zoom of (c) on the edge of the gold layer.

Figure 4.14: Pictures of the gold electrodeposition on a Si substrate showing brown contaminants. In (a), a picture of the atom-chip right after the electrodeposition showing inhomogeneous brown deposition. In (b), SEM image of the atom-chip showing the region of the red rectangle of Fig. 4.4a, we see in clear grey the irregularity of the brown deposition of (a). In (c), we look into the gap between wires, we can clearly distinguish the contaminant crystals which appear to be present only on the top of the deposition. In (d), we zoom on (c) to have a better look at the wire's edge, at this definition, the SEM is not capable to show a visible difference between the wire's edge and the bottom seed layer.

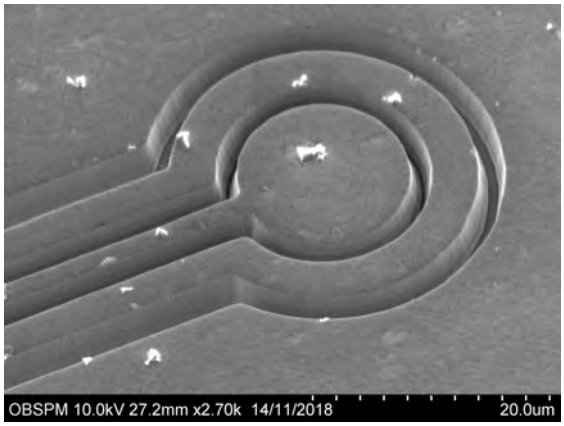

(a) Electrodeposited loop wire seen with a tilted angle.

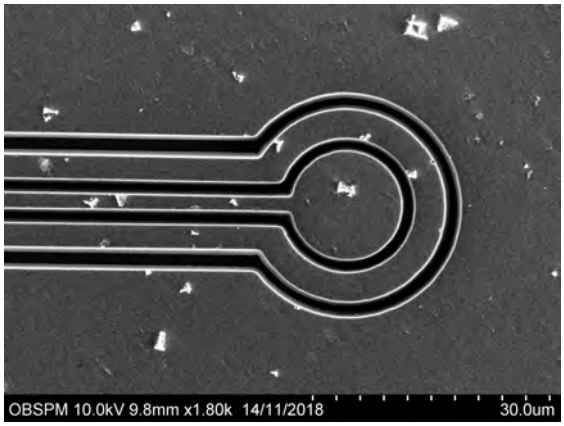

(b) Electrodeposited loop wire seen from above.

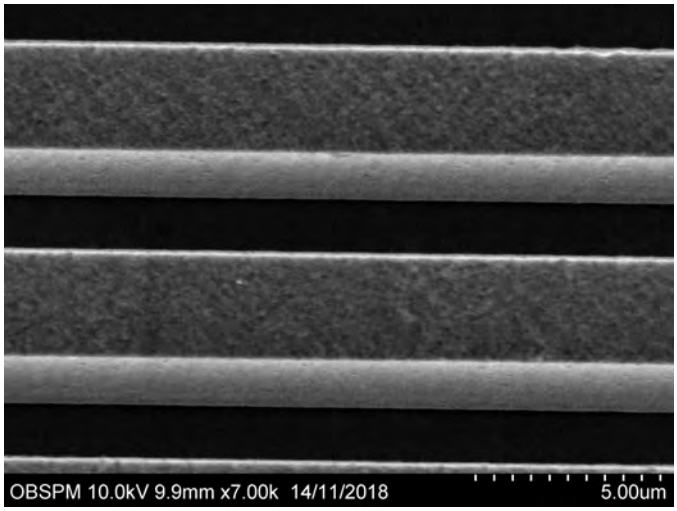

(c) Electrodeposited 3 wires seen with a tilt.

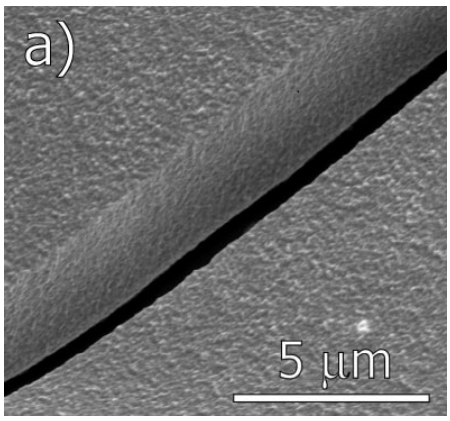

(d) Electrodeposited wires from Philipp Treutlein in [66]

Figure 4.15: SEM images of electrodeposited wires showing the surface roughness of the wires. In (a), we see the loop wire with a tilt in order to see the edges. The loop wire photolithography has a known roughness due to UV light difraction (and is mask dependant), we can see the reproduction of this roughness on the electrodeposition. In (b), the loop wire from above, we see the fidelity of the pattern reproduction and the low slope of the wire's edge. In (c), 3 wires seen with a tilt in order to show the wire's edge profile. In (d), image taken from Philipp Treutlein [66] in order to compare roughness to our wires. Images (c) and (d) are at the same scale.

This shows not only the validity of our choices for the electrodeposition bath, but also opens the possibilities to improvement the surface roughness through electrodeposition as there is still room for improvement from our first deposition attempt. Moreover, the unexpected difference between the wire's edge roughness and top roughness shows that there is still margin to improve the roughness measurement of $R_q \simeq 12$ nm. This point will be important in the future, indeed, if there's no need to improve such surface roughness for an atom-chips on polycrystalline AlN substrate, there is however an interest to be capable to produce thick metal deposition for mono-crystalline substrate with lower surface roughness (below the nm). Moreover, it is possible that an electrodeposition of such quality on AlN substrate could force the roughness of the wire edges to be defined by the photolithography as they grow confined between two photoresist strips.

4.4 Finishing processes and conclusion

With our metal deposition achieved, we still need to to get rid of the polymerised photoresist by disolving it into an organic solvent (acetone or TechniStrip NI 555). This step is often called lift-off (step 4 in Fig. 4.1a and step 6 in Fig. 4.1b) as (for PVD) the gold on the top of the photoresist is lifted-off, however lift-off refers to the whole micro-fabrication process where metal deposition is used to grow structures rather than etching metal layers [77]. There is no gold being lifted-off in the case of electrodeposition processes, however, this step is still called lift-off as a metonymy due to the symmetry of a metal deposition process instead of etching a metal layer. It is a pretty simple process for electrodeposition as the photoresist is well exposed to the organic solvent and will simply dissolve in it. However, things get more difficult for the PVD process as metal is also deposited on top of the photoresist, making it less exposed to the chemical. Moreover, due to this metal growing on the top of the photoresist, there is a need for an under-cut profile of the resist so the chemical can access the resist by the edges. Under this condition, step coverage can be a significant issue as it tends to close the gaps on top of the wires, sealing the photoresist edges to the solvent, and the under-cut photoresist profile also tends to be covered in metal as you can see in Fig. 4.10. You can actually see for example in

Fig. 4.8b and in Fig. 4.8d that the lift-off process was not totally successful as we see metal 'ears', a common problem related to lift-off due to metal growing on the under-cut photoresist profile then falling on the wires during the lift-off. We believe, however, that those ears are not only due to the step coverage of our PVD process, but also the fact that we have coated by sputtering the whole atom-chip (in Fig. 4.8b and in Fig. 4.8d) with a thin layer of gold (few nm) in order to observe the step coverage on the photoresist by SEM. As you can see in Fig. 4.16, a lift-off following a gold PVD on AlN substrate, the gold metal layer on the top of the photoresist is being lifted-off and falling to the bottom of the beaker.

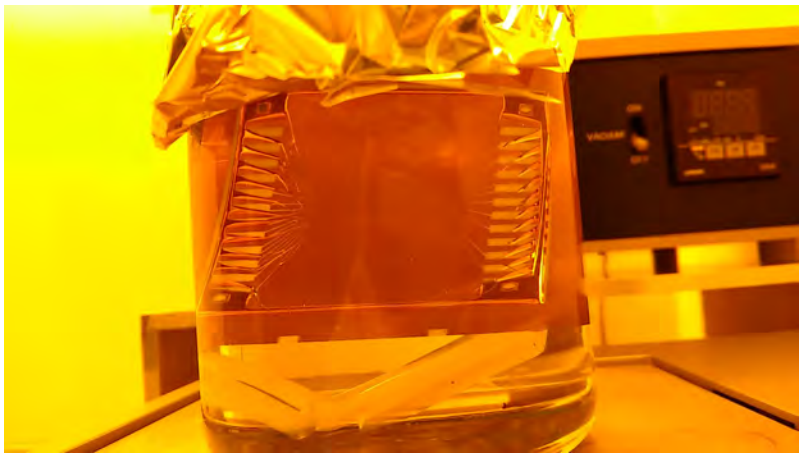

(a) A gold PVD on ALN substrate ongoing the lift-off process.

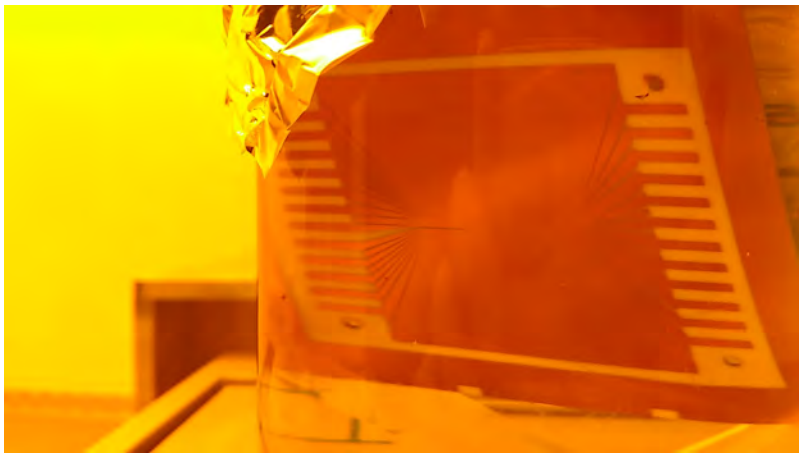

(b) A gold PVD on ALN substrate at the end of the lift-off process.

Figure 4.16: Lift-off process of a gold PVD. In (a) you can see the gold layer deposited on the top of the photoresist fall as the photoresist is dissolved. In (b), you can see the result of the lift-off once all the photoresist's gold layer is gone.

As we mentioned, for the electrodeposition process, the lift-off is easier. However, there is an extra step, compared to the PVD process, in order to expose the gap between the wires. This extra step is the etching of the seed layer, done by chemical processes i.e. wet etching, or by Reactive Ion Etcching (RIE) (step 7 in Fig. 4.1b). There is no particular need for lithography as this process is basically etching a thickness of $50 - 200$ nm (corresponding to the seed layer's thickness) across all the atom-chip, which does not change the intended deposited thickness as the etched layer was an original "offset" to the general thickness. This process step is known to increase the surface roughnesses, Konstantin Ott in Ref. [68] shows that RIE does not deteriorate the gold surface roughness within the measurement definition of an Atomic Force Microscope (AFM) while a wet etching (aqua regia) increase the R_a surface roughness of 32 nm. The efficiency of RIE etching is believed to be due to the chemical inertness of gold as in the same process the RIE have increased the AlN R_a surface roughness of by 16 nm.

Following this step, we need to build a mirror on the atom-chip in order to create a mirror Magneto-Optical Trap (MOT). A very easy way to produce a mirror is to deposit a layer of gold on a smooth surface (step 6 in Fig. 4.1a and step 9 in Fig. 4.1b). Therefore we need to deposit on the top of our wires an insulator layer to insulate the metal mirror from the wire, but also to flatten the surface. This can be done by using a layer of our photoresist ($\simeq 5$ μm) polymerised by UV exposure and then slowly baked up to 200 °C to harden it and make it compatible with a high vacuum (step 5 in Fig. 4.1a and step 8 in Fig. 4.1b). The final result (from a PVD process) can be seen in Fig. 4.17; this atom-chip is currently used in experiments in the vacuum chamber at SYRTE.

We can conclude that we have succeeded to transfer the atom-chip fabrication techniques to l'Observatoire's clean room, as this clean room has now produced an atom-chip which is in use in the SYRTE's experiment vacuum chamber. We have also shown a way to improve atom-chip fabrication, by electrodeposition, which would allow us to fabricate thick metal wires that decrease the power consumption and increase the heat dissipation of atom-chips. This improvement can be made without sacrificing the surface roughness of our wires, compared to PVD process, since only the AlN substrates roughness and the photolithography quality would

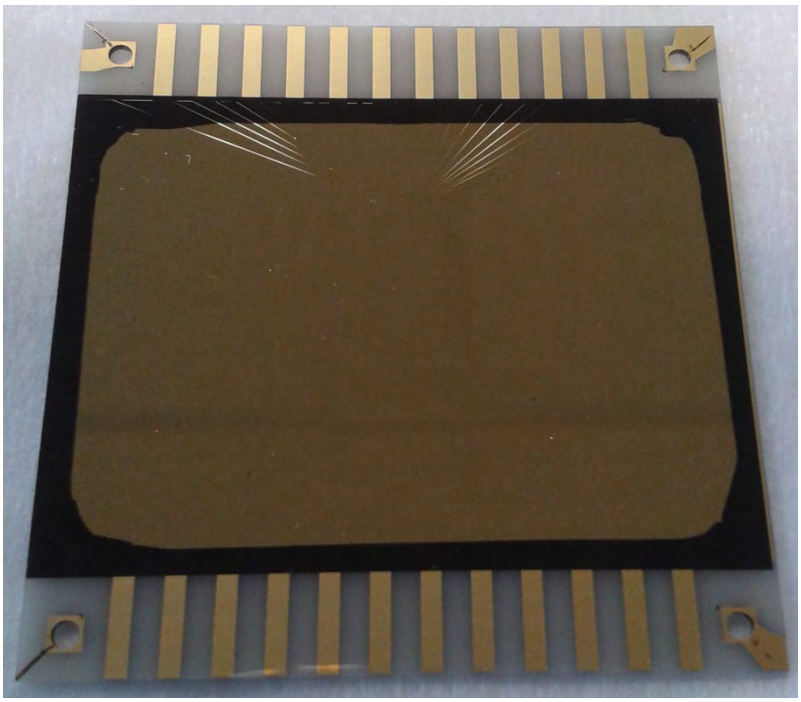

Figure 4.17: Picture of an atom-chip fabricated at l'Observatoire de Paris following the PVD processes developed in this thesis. This atom-chip is currently being used in the SYRTE GyrAChip experiment.

limit the wires roughness. This would then redirect the efforts to reduce technical noise to the current generators, as we will discuss in the next chapter.

Chapter 5

Floating current supplies and current noise

In Chapter 4 we have discussed the technical noise related to wire roughness, here we will discuss the technical noise related to current generators. Furthermore, it was shown that $\simeq$ 10 kHz current modulation can reduce the potential roughness related to wire roughness by at least a factor of five [37].

In this thesis, I worked on the characterisation and optimisation of current supplies (i.e. current generators) that will be used in the GyrAChip experiment. We need low noise floating current supplies as we have several wires making connection with each other (as you can see in Fig. 4.4). Floating current supplies are generators with a floating ground which help to eliminate ground loops, reducing the noise coupled to the system.

In Ref. [78], Friedemann Reinhard worked to develop the current supplies in use in the GyrAChip experiment. We can see the circuit of a prototype of these low noise current supply in Fig. 5.1 taken from Ref. [78], where Friedemann Reinhard helped in their development for l'Observatoire. They showed good noise performance in the past as they can achieve a relative noise level below 10^{-5} (relative to the current load). They are capable of delivering up to 3 A with a power capacity of 10 W. We will discuss these current supply in the first part of this chapter.

From Friedemann Reinhard's work we can access the current supply requirement for our experiment. We need to prevent fluctuating Zeeman shifts by controling magnetic fields on the 10 μG level: a noise level below 10^{-5} relatively to the current

output. We also need alternating current in order to reduce potential roughness [37]. This is a major issue for us since our current supplies are not designed to deliver alternating currents. Those current supplies can be driven by an external signal, but they can't inverse the current polarity, therefore they can only modulate current within one current polarity. There is several proposals to address this issue. One proposal is to use another current supply to give a negative offset.

Another concern for our experiment is the resistivity of the wires. We want to pass currents, within the 10^{-1} A order, through wires with a 3 μm width and a height varying from 3 μm to 2 μm. A resistivity of $\simeq 50\ \Omega$ was measured on 2 μm wires. However, the max power given by the supplies being $\simeq 10$ W, wires with a section of 3 μm $\times$ 2 μm can be driven only up to $\simeq 400$ mA. In Ref. [70], Jerome Esteve studied the maximal current one can put in a micro-sized wire (independently of the maximal power output of the supply), this study address the thermal dissipation of those wires. As one can easily imagine, too much current in a micro-sized wire and it will melt or evaporate.

These homemade low noise current supplies are grounded by default. However, our experiment requires the use of floating supplies for the atom-chip pattern that was build in Chapter 4. Indeed, in Chapter 4, we see that our U-wire and Z-wire [49] are in contact due to the '3-wires' going through them (see Fig. 4.4). These '3-wires' could be used, for example, to generate a RF-dressed linear waveguide, therefore, we would need to supply those wires with current while making sure that the AC current of each one of the '3-wire' does not interfere when those wires are in contact. Therefore, we need to modify the current supply so they can have a floating ground. The idea is to isolate the current generator circuit from any grounding. By doing so, we could cut the current generator circuit from other circuits, related to the control of the current supply or to the low noise generation. We identified two configurations which will isolate the core of the current generator from groundings, these configurations are called *Floating-1* and *Floating-2*. The configuration *Floating-1* correspond to the modifications done on the circuit of Fig. 5.1 by the black crosses while the modification done for *Floating-2* are shown in red in Fig. 5.1. Given that the position for *Floating-1* harms the low noise characteristic of the current supply, the second position, *Floating-2*, is then chosen to be in a position less harmful to the

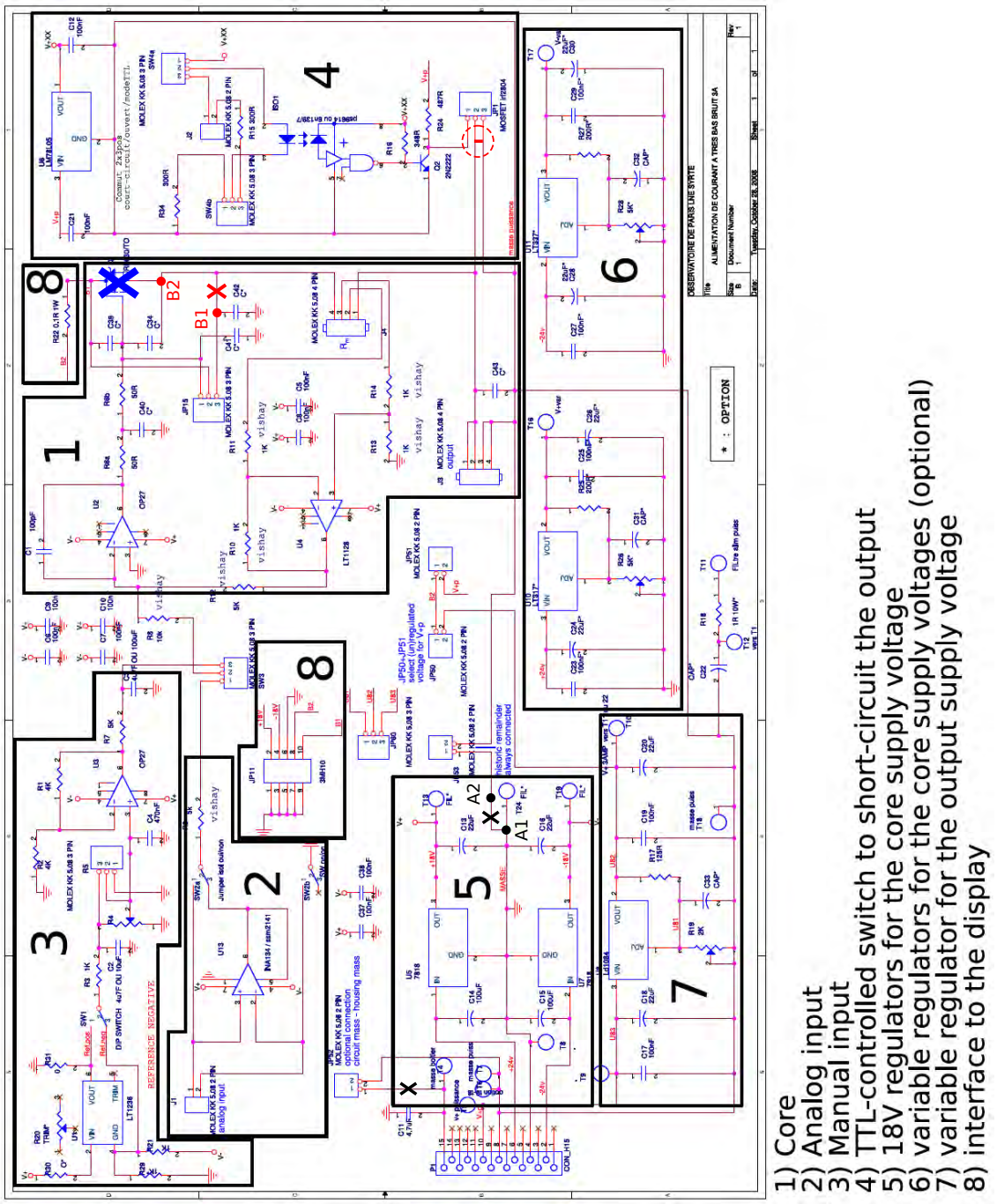

Figure 5.1: Circuit of a homemade low noise current supply from Ref. [78]. The blue cross represent a component which is not used anymore in those current (the circuit is let open at the blue cross). The black crosses are positions where the circuit is open only for the *Floating-1* configuration. The red cross is a position where the circuit is open only for the *Floating-2* configuration, the red dashed circle shows where a short-circuit is made for the *Floating-2* configuration and finally the output of the current supply in the *Floating-2* configuration are the position B1 and B2 (red dots) instead of the component J3.

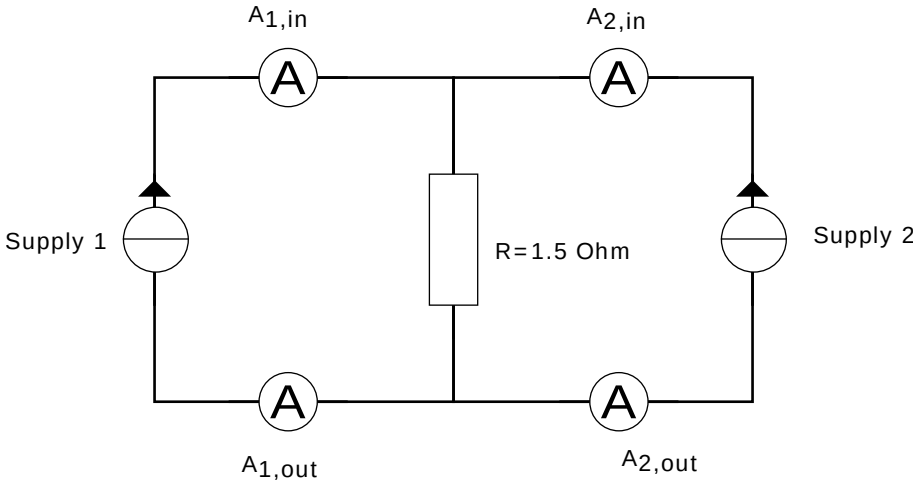

Figure 5.2: Electrical schematic for the 'simple test'. Four ammeter allow us to measure the current from the supply in and out of the resistor.

low noise. However, *Floating-2* isolates the current generator circuit from several control features of the current supply, like for instance an emergency Short-Circuit switch used to cut the current supply from the load.

We will then discuss of ways used to test the floating ground of these current supply.

5.1 Floating configurations

5.1.1 'Simple test'

Since we have the '3-wires' going through the U and Z wires (see Fig. 4.4), we implemented a test protocol called the 'simple test'. This test aim to see if two current supply have a floating ground. Two current supply are connected to the same load (a 1.5 Ω low noise resistor) while the current leaving and getting to each current supply is monitored. You can see in Fig. 5.2 the electrical circuit corresponding to the 'simple test'. We can see in Fig. 5.2 the load R, which was measured at 1.5 Ω. This resistor is equipped to dissipate heat and allow up to 25 W, it is therefore well suited for the 'simple test' as we will use two 10 W generator to run current through it. This test consist of measuring the current in ($A_{i,in}$) and out ($A_{i,out}$) of the resistor to the current supply i. In this test, if the two current supply have a floating ground, then the current measured by $A_{i,in}$ should be the same as

$A_{1,in}$ (A)	$A_{1,out}$ (A)	$A_{2,in}$ (A)	$A_{2,out}$ (A)
0.000	0.003	0.00	0.003
0.100	0.104	0.00	0.003
0.100	0.104	3.00	3.00
0.500	0.506	0.00	0.003
0.500	0.506	3.00	3.00
1.001	1.008	0.00	0.003
1.001	1.008	3.00	3.00
0.000	0.003	0.00	0.003
0.000	0.003	1.00	0.994
2.657	2.667	1.00	0.994
0.000	0.003	0.00	0.003
2.991	3.001	0.00	0.003

Table 5.1: 'Simple test' results for two current supplies in the *Floating-1* configuration. The first line is measured with the supplies unplugged, it gives an idea of the ammeters uncertainty, which is common for other tables. Data in blue are the maximum current output obtained without inducing changes in the readings of the other current supply.

$A_{i,out}$ independent of any current coming out of the other current supply ($A_{j,in}$ and $A_{j,out}$ for $i \neq j$).

You can see the measurements from this test in Tab. 5.1 using two current supplies in the *Floating-1* configuration, and in Tab. 5.2 using two current supplies in the *Floating-2* configuration. In Tab. 5.1 and Tab. 5.2 , the data shown in blue corresponds to the maximum output of the current supply (maximum either on the current output, or on the power output), this maximum is obtain starting from 0 A while taking care that the readings on the other current supply does not changes. Tab. 5.1 and Tab. 5.2 present data which are to be expected from current supplies with a floating ground.

For comparison, we can see in Tab. 5.3 that two grounded current supply do not show the same behavior of the current supplies in Tab. 5.1. Indeed, the readings of $A_{i,out}$ are different from the readings of $A_{i,in}$, furthermore, part of the current

$A_{1,in}$ (A)	$A_{1,out}$ (A)	$A_{2,in}$ (A)	$A_{2,out}$ (A)
0.00	0.003	0.00	0.003
2.96	2.918	0.10	0.102
2.83	2.798	0.50	0.500
2.60	2.576	1.00	1.000
2.45	2.427	1.50	1.495
2.28	2.261	2.00	1.993
2.09	2.072	2.50	2.492
1.92	1.911	3.00	2.985
0.10	0.119	3.32	3.306
0.50	0.509	3.32	3.306
1.00	1.003	3.32	3.306
1.50	1.491	3.32	3.306

Table 5.2: 'Simple test' results for two current supply in the *Floating-2* configuration. Data in blue are the maximum current output obtained without inducing changes in the readings of the other current supply.

$A_{1,in}$ (A)	$A_{1,out}$ (A)	$A_{2,in}$ (A)	$A_{2,out}$ (A)
0.003	0.003	0.00	0.00
0.500	0.440	0.00	0.04
1.004	0.883	0.00	0.11
1.003	0.931	0.50	0.56
1.003	0.978	1.00	1.02

Table 5.3: 'Simple test' of two grounded current supply.

coming from a supply i ($A_{i,in}$) can be seen following the path of $A_{j,out}$, to the supply j.

5.1.2 'Simple test': mixing the configurations

Out of curiosity, but also to see the reliability of the floating configuration, we ran the 'simple test' between current supplies in different configurations. Therefore, we can see in Tab. 5.4 the results of 'simple test' with one supply in the *Floating-1* configuration and the other in the *Floating-2* configuration. There is no different behavior from the experiments done for Tab. 5.1 and Tab. 5.2. This experiment increases our trust in the 'simple test' as it allows to see behavior of floating current supplies despite their differences.

Furthermore, we realised a 'simple test' between floating and grounded current supplies. One would expect that if one of the current supply is floating, then it would be enough to have a positive outcome to the 'simple test'. This actually is the case, as you can see in Tab. 5.5. However, it appears that fast output variation in the floating current supply induced instabilities in the grounded current supply as small ranges current variation could be seen in the grounded supply readings. This is shown in Tab. 5.5 by the data with a red color.

5.1.3 'Circuit Test'

We wanted to push further the 'simple test' and compare the floating configuration behavior in a circuit with asymmetric resistivity values. Therefore, in addition to the 'simple test', we established the 'circuit test'.

$A_{1,in}$ (A)	$A_{1,out}$ (A)	$A_{2,in}$ (A)	$A_{2,out}$ (A)
0.00	0.003	0.00	0.003
0.10	0.105	3.12	3.118
0.50	0.497	0.00	0.003
0.50	0.497	3.09	3.086
1.00	0.998	3.06	3.056
1.50	1.498	3.00	3.008
1.96	1.954	3.05	3.041
2.94	2.925	0.10	0.111
2.79	2.777	0.50	0.505
2.61	2.607	1.00	1.005
2.45	2.438	1.50	1.498
2.27	2.258	2.01	2.014
1.93	1.919	3.00	3.000

Table 5.4: Data result from the 'simple test' with a current supply in configuration *Floating-1* (supply 1) and a current supply in configuration *Floating-2* (supply 2). Data in blue are the maximum current output obtained without inducing changes in the readings of the other current supply.

$A_{1,in}$ (A)	$A_{1,out}$ (A)	$A_{2,in}$ (A)	$A_{2,out}$ (A)
0.00	0.003	0.00	0.003
0.10	0.105	3.01	3.009
0.50	0.502	3.06	3.052
1.00	0.997	3.05	3.050
1.50	1.495	3.15	3.146
2.86	2.856	0.10	0.108
2.73	2.856	0.49	0.500
2.55	2.537	0.99	0.999
2.39	2.378	1.50	1.499
2.21	2.201	2.00	1.999

Table 5.5: Data result from the 'simple test' between floating and grounded current supplies. Data in blue are the maximum current output obtained without inducing an important change in the readings of the other current supply. The data in red shows a mean value of current from variations that are observed when the other current supply (seen by $A_{1,\text{in}}$ and $A_{1,\text{out}}$) is being controlled and its current output is changing.

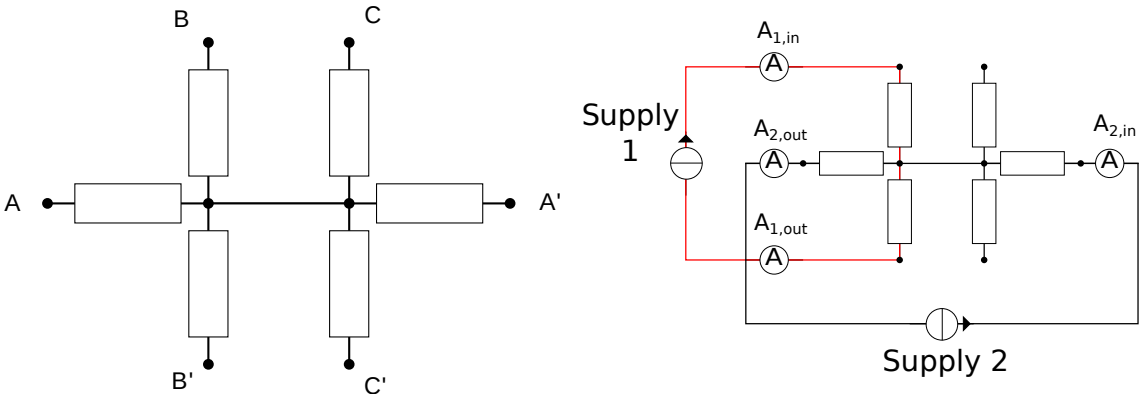

(a) The atom-chip equivalent circuit

(b) The circuit test

Figure 5.3: Electrical schematic for the 'circuit test'. In (a), a circuit equivalent to our '3-wires' going through the U-wire. BB' have 310 Ω measured resistivity and CC' have 303 Ω measured resistivity. Together they represent two of this '3-wires'. AA' have 7.2Ω measured resistivity and represent the U-wire. In (b), the circuit test.

The purpose of this test is to validate the floating behavior of the current supplies for an application closer to our experiment in terms of resistivity values. We considered that in our chip the resistivity of the '3-wires' is of the order of 100 Ω (for a height of 1 μm) and that the U and Z wires are in the order of 1 Ω. This is an important difference of resistivity and we want to be sure that our current supplies can work as intended in this condition with a floating ground.

To do so, we realised a macroscopic circuit equivalent to our chip pattern (see Fig 4.4). We can see the circuit in Fig. 5.3, the resistors used can support 7 W. This test showed no difference in results from our 'simple test'.

5.2 Noise measurement

5.2.1 Experimental setup

In the previous sections, we have presented our homemade current supply and its different configuration: *Floating-1*, *Floating-2* and grounded. We have shown that floating current supplies are capable to generate a specific current in a load which is in contact with other current supplies, without being affected by those other current supplies. However, we have not addressed the question of current noise yet, and more specifically, if our modifications to floating configuration have increased the current noise.

In order to measure the current noise we used a FFT spectrum analyzer (SRS SR-760). This spectrum analyzer was used to measure the Power Spectral Density (PSD) of a voltage signal. Therefore, we need to convert the current output of our supplies to a voltage signal. We then used a current sense resistor of 10 Ω, that you can see in the I/V electrical circuit Fig. 5.4.

5.2.2 FFT analyzer and PSD measurement

Something which is important to have in mind for this part is that we worked in AC mode (for the FFT analyzer), the current supplies are giving constant currents, the voltage we measure is V_{RMS}. This choice was made according to the fact that we want to measure the variations of a DC signal. This mean that we are applying to our signal a high pass filter, with a cutoff frequency below the lower limit of the frequency span (250 Hz), which mean that the results used here are not relevant for long term stability.

In order to see the quality of our I/V circuit and the noise measurement limitation of the FFT analyzer, we measured the PSD of the SR760 (before plugging any supply to it) in three configuration:

- **Open input**, which means that the input is open and nothing is plugged to it
- 50 Ω **terminator**, which means that the input is closed by a classic 50 Ω BNC terminator

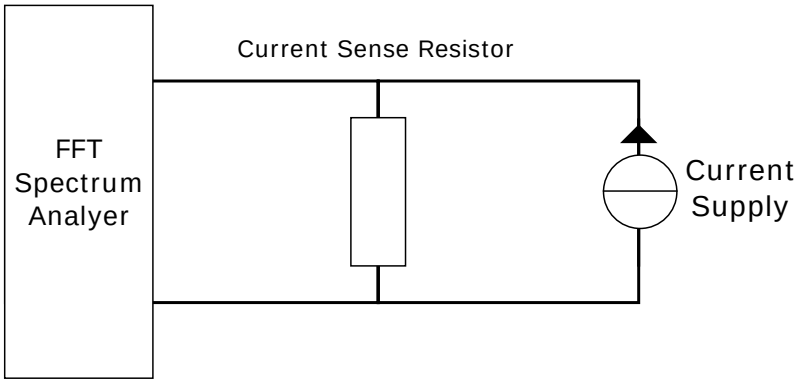

(a) I/V circuit

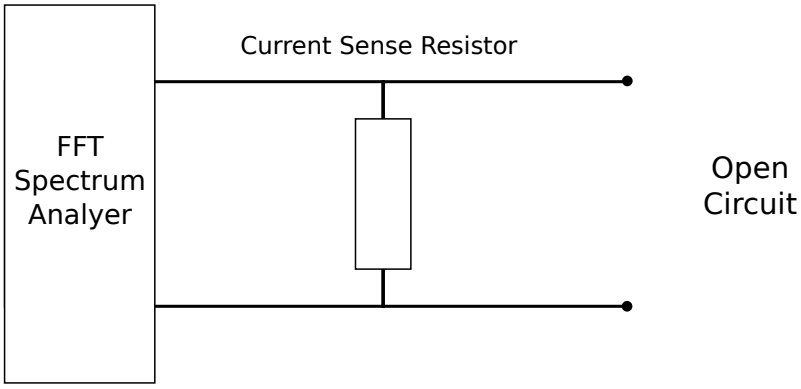

(b) I/V circuit without supply

Figure 5.4: In (a), electrical circuit used to connect the current supplies to the FFT spectrum analyzer. The Current Sense Resistor is a special resistance with no inductance ($R = 10\ \Omega$ here). In (b), I/V circuit configuration without current supply, used to characterise the noise related to the resistor. The resistor is in contact with the metal table as heat sink.

- **Open I/V circuit**, as you can see in Fig. 5.4b, the current sense resistor is plugged to the FFT without any current supply which give us the noise floor related to the sensing resistor

We can see in Fig. 5.5 data acquired from the FFT analyzer without supply (but with the I/V circuit) and a PSD measurement realized by Friedmann in Ref. [78]. The conversion in Fig 5.5a is done by dividing the raw data by $R = 10\ \Omega$. The PSD with 50 Ω terminator is almost identical to the PSD with I/V circuit (and better then the Open input) which should make us confident on the quality of the I/V circuit. However we can see an important Flicker noise on this PSD for all three configurations which can be a major issue since the first point is at 250 Hz. Flicker noise is usually visible below 10^2 Hz so either the white noise is really small, or the Flicker noise is too important.

We can see that despite the Flicker noise our measurements are at the same level as Friedmann's measurement (at least in the [250 Hz,10^5 Hz] range). This is in fact a bad news. Indeed in Fig. 5.5a the measurement is done without any current supply, it then represent the intrinsic noise of the setup which we would expect to be below Friedmann's measurement. It is most probable that the I/V circuit is not suitable for a proper measurement, it is also possible that the resistor (below ±1% uncertainty) used is the origin of the Flicker noise.

5.2.3 Current supplies PSD measurement

You can see in Fig. 5.6 the PSD measurement of a grounded homemade current supply and a current supply in the *Floating-1-capa* configuration, this measurements will be used to evaluate the increase in current noise by modifying current supplies to a floating configurations. The 'Unplugged' curve in Fig. 5.6 correspond to a measurement where the current supply was connected to the FFT spectrum analyzer by the I/V circuit, but was not plugged to a power socket. The 'Max Power' curve in Fig. 5.6 is the measurement where the current supply reach its maximum output power (here $\simeq 11\ W$). The first thing we can observe from Fig. 5.6 is that except for extreme values (0 A and 'Maximal Power') the PSD from the different current values are almost the same.

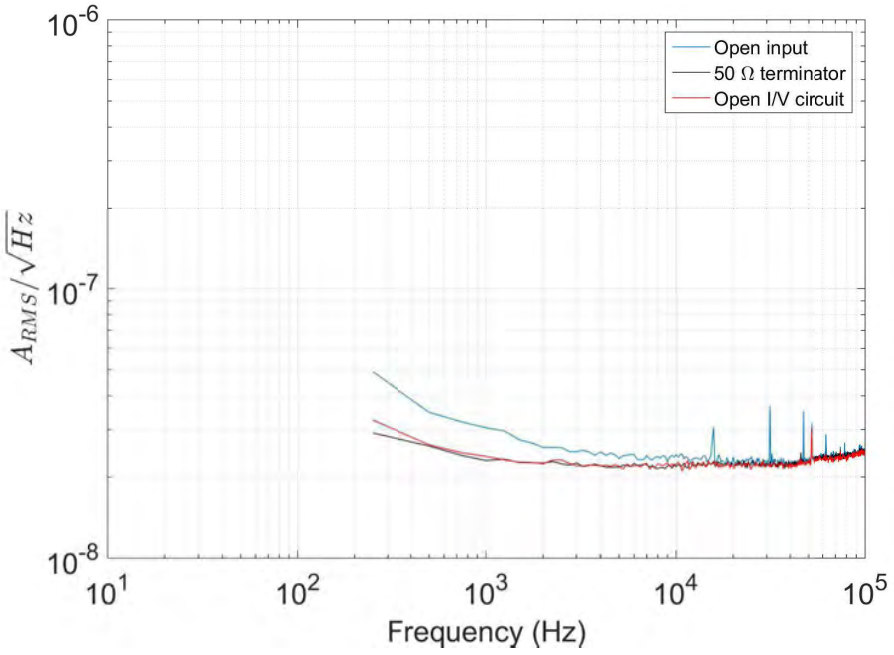

(a) PSD of **SR760**

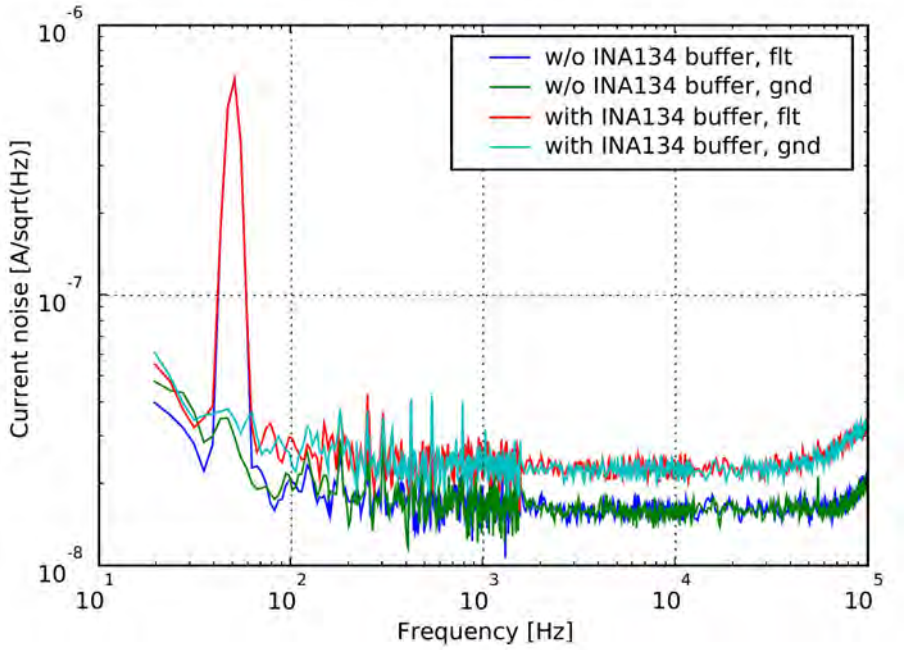

(b) Friedmann's noise measurement

Figure 5.5: In (a), PSD of the **SR760** in the three configurations discussed in text. The axes are chosen in order to coincide with Friedmann's noise measurement of the same current supply and on the same FFT spectrumm analyzer. In (b), Friedmann's noise measurement presented in Ref. [78].

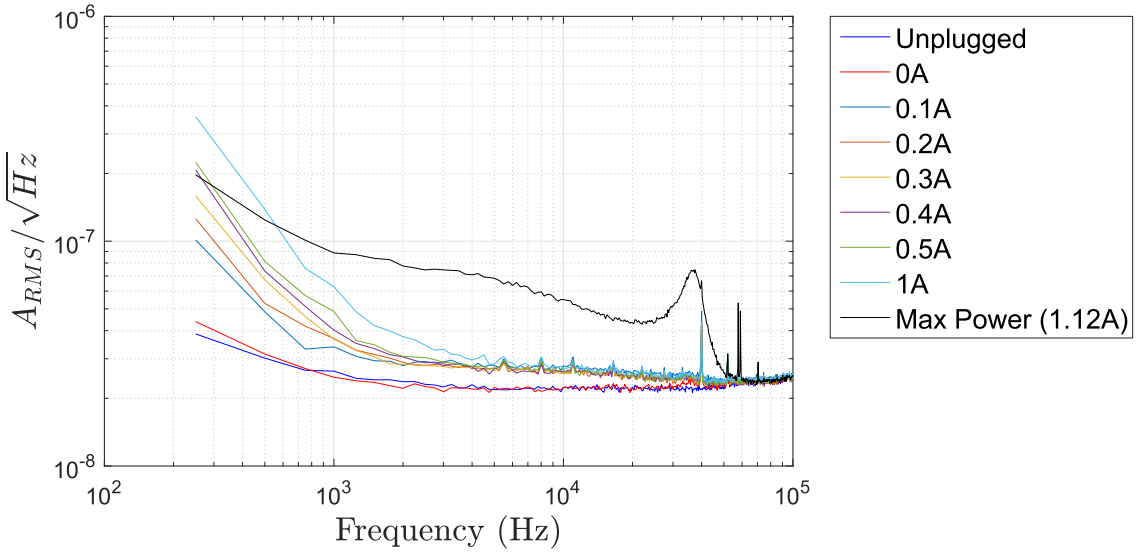

(a) PSD of a grounded current supply for different value of DC current output.

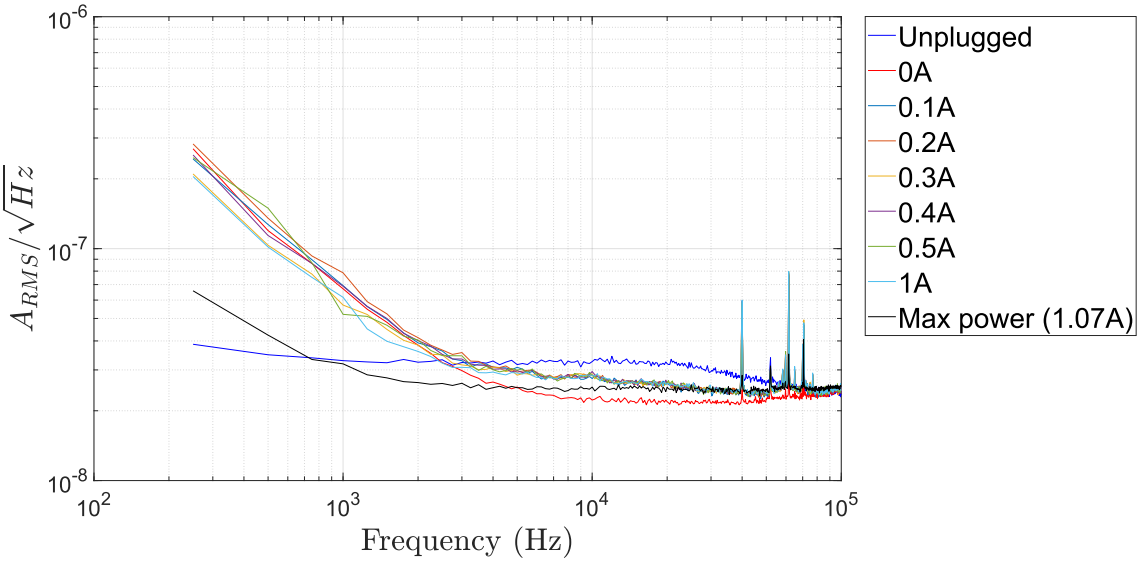

(b) PSD of a current supply in the *Floating-1-capa* configuration for different value of DC current output.

Figure 5.6: Comparison between the PSD of a grounded current supply and the PSD of a current supply in the configuration *Floating-1-capa* (which will be the configuration used in the experiment at l'Observatoire). We can see that the PSD of configuration *Floating-1-capa* is comparable to the PSD of the grounded configuration.

However, the Flicker noise is extremely important. If we compare Fig. 5.6 to Fig. 5.5b we can clearly see that the Flicker noise is responsible for the signal going above Friedmann's measurements at low frequencies. This is a clear issue for our low noise current supply, however despite the important Flicker noise, the current supply is still in agreement with the $< 10^{-5}$ relative noise requirement (at least in the $[250Hz, 10^5 Hz]$ range, as we will see in Tab. 5.6. Indeed, except for the 'Max Power' signal where we can see a strange resonance (the reason of it is unknown) the RMS noise is always below the 10^{-5} relative noise requirement. Anyway we should not need to reach the maximal power of those current supply.

5.2.4 RMS relative noise

The RMS noise is calculated according to this formula:

$$\mathrm{RMS} = \sqrt{\int \mathrm{PSD}^2 \, \mathrm{d}f}, \tag{5.1}$$

where f is the frequency parameter in the PSD. We then applied the trapeze integration method to the PSD measurement of current supplies in different configurations. We can see the RMS relative noises of each configuration in Tab. 5.6. The RMS relative noise of the current supplies in *Floating-1* and *Floating-2* configurations is too high. However, we can see a lower RMS relative noise for *Floating-2* configuration.

In Ref. [78], we can see that at some point the ground of the housing was connected to the ground of the circuit through capacitors in order to diminish noise in floating supplies. Following this idea we decided to add capacitors, from the *Floating-1* configuration we add two capacitor of 1 μF in parallel between the position A1 and A2 in Fig. 5.1, this is configuration *Floating-1-capa*. From configuration *Floating-1-capa* we apply the changes which are in red in Fig. 5.1, this is configuration *Floating-2-capa* (which is basically doing a configuration *Floating-2* added to a configuration *Floating-1-capa*). We also realised successful 'simple tests' in order to check if this modification still let the current supply with a floating ground. We then measured the PSD of *Floating-1-capa* and *Floating-2-capa* and calculated their RMS relative noise, which you can see in Tab. 5.6.

From the data present in Tab. 5.6, we can conclude that the best choice for our experiment is the *Floating-1-capa* configuration. *Floating-2-capa* may show RMS

relative noise values lower than *Floating-1-capa*, however, it still go beyond the $< 10^{-5}$ RMS relative noise requirement for 0 A and 'Max power', while *Floating-1-capa* is consistently below this $< 10^{-5}$ RMS relative noise requirement. Moreover *Floating-1-capa* even succeed to best the grounded configuration as the grounded configuration goes above the requirement for the 'Max Power'.

Output	Grounded	*Floating-1*	*Floating-1-capa*	*Floating-2*	*Floating-2-capa*
Unplugged	7.28×10^{-6}	7.63×10^{-6}	8.80×10^{-6}	7.21×10^{-6}	6.96×10^{-6}
$0A$	7.44×10^{-6}	2.63×10^{-5}	8.34×10^{-6}	2.64×10^{-5}	4.63×10^{-5}
$0.1A$	8.17×10^{-6}	3.57×10^{-3}	9.12×10^{-6}	2.39×10^{-4}	9.03×10^{-6}
$0.2A$	7.95×10^{-6}	3.99×10^{-3}	9.39×10^{-6}	2.58×10^{-4}	8.69×10^{-6}
$0.3A$	8.11×10^{-6}	4.19×10^{-3}	8.92×10^{-6}	2.82×10^{-4}	8.73×10^{-6}
$0.4A$	8.27×10^{-6}	4.27×10^{-3}	9.15×10^{-6}	3.44×10^{-4}	8.43×10^{-6}
$0.5A$	8.39×10^{-6}	4.28×10^{-3}	9.22×10^{-6}	3.63×10^{-4}	8.65×10^{-6}
$1A$	9.41×10^{-6}	3.07×10^{-3}	8.91×10^{-6}	**No Data**	8.68×10^{-6}
Max Power	1.36×10^{-5}	1.45×10^{-5}	7.98×10^{-6}	2.08×10^{-5}	2.49×10^{-5}

Table 5.6: RMS relative noise of the current supplies in different configurations. In blue, the RMS value that are under $10^{-5}A$. The unplugged line can be seen as a reference floor.

5.2.5 Conclusion on the homemade current supplies

We showed that the configuration *Floating-1-capa* is the best configuration for us. It is a floating ground configuration with a RMS relative noise below 10^{-5} in the $[250Hz, 10^5Hz]$ range. However the RMS relative noise measurement, even being below 10^{-5}, still approach dangerously this value. We suspect two major problems to address if one wants to improve the RMS relative noise:

1. The important flicker noise: we suspect it comes from the voltage reference (here being internal). Using the analogue input with a good low noise voltage source would probably solve this problem.

2. The too high white noise floor: even when the current supply is not plugged into the power socket. This show a limitation due to the measurement rather then to the current supply. The fact we are using the same instrument as Friedemann suggests that the origin of this issue is due to the I/V circuit. To have a better measurement of this RMS noise, we need a better circuit (i.e. a better current sense resistor for the conversion from current to voltage)

Still, we can use in our experiment homemade low noise current supplies in the *Floating-1-capa* configuration. Furthermore, depending on the way the magnetic potential is generated by the wire patterns, it is possible to relate the current noise, measured here, through the PSD to atom's phase noise by using the auto-correlation function and its relation to PSD. This relation would allow us to see the viability of generating ring traps for gyroscopes.

Chapter 6

Pumping dynamics and dead-time

So far we have discussed of the propagation of atoms in a waveguide (and their interference), of the fabrication of atom-chips and of the current noise. However, a key element for our quantum sensor to reach the required level of sensitivity is the preparation of a well-controlled state of the atoms in terms of their internal and external degrees of freedom. This requires laser cooling in a magneto-optical trap (MOT) to sub-Doppler temperatures (on the order of 1 μK and below), which unavoidably introduces a dead time in the measurement process. For atom interferometers, this translates into the well-known Dick effect that degrades the stability of these devices [79, 80, 81, 82]. To reduce the MOT loading time, a relatively high background partial pressure of the atoms to be cooled is required [83], for example, approximately 10^{-8} mbar for ^{87}Rb atoms. However, this high background pressure reduces the available lifetime to perform the desired experiments with the trapped atom clouds [84] and also, it degrades the contrast of the interference fringes leading to a reduction of the signal-to-noise ratio of the measurements.

In a typical cold-atom experiment the high background pressure problem is overcome, on the one hand, by using two chambers connected via a differential pumping stage. In this situation, one chamber (at high pressure) is used as a bright source of cold atoms and the other one (at low pressure) as a science chamber. However, this solution is hardly compatible with the realization of cold-atom-based compact and miniature sensors. So, on the other hand, when using a single vacuum chamber incorporating the atom source (i.e. an alkali metal dispenser) after the MOT loading stage the residual background atoms need to be pumped out quickly. This

is needed in order to preserve a useful level of lifetime of the trapped atoms and to avoid an important increase of the dead time. This latter situation implies the ability to switch from high (approximately 10^{-8} mbar) to low pressure (approximately 10^{-11} mbar) in a few tenths of ms [85]. A very promising solution has been recently found [86], which allows one to quickly and reversibly control the Rb background pressure in a cell. In this setup, a MOT with up to 10^6 atoms has been realized. However, no compatibility with a pressure level of approximately 10^{-11} mbar has been demonstrated yet with this technique.

Besides the investigations presented in Refs. [85, 86], other relevant studies on the optimized operation of compact UHV systems have been reported before. In Ref. [87], the authors present a detailed analysis on the use of light-induced atomic desorption to modulate the background pressure of ^{87}Rb atoms in a glass cell. They developed a model to find the number of atoms loaded in a MOT when the light is on, and demonstrated an order of magnitude increase under this condition. In the context of atom interferometry and atom sensors, an UHV system was designed and tested for operation in the highly vibrating environment of a rocket [88] (for the MAIUS project). In Ref. [89], the authors investigated the use of passive vacuum pumps (nonevaporable getter pumps) for the development of compact cold-atom sensors. Finally, in Ref. [90], microfabricated nonmagnetic ion pumps were demonstrated with the aim of maintaining UHV conditions in miniature vacuum chambers for atom interferometry.

The aim of the work presented in this Chapter is to understand from the physics point of view, the pressure dynamics of single vacuum chambers loaded with atoms via a dispenser and pumped out by a SIP (Sputter Ion Pump). So far, SIPs are commonly used in cold-atom experiments requiring UHV. Since they are an unavoidable component, which is at the same time able to provide pressure readings [91, 92], it is therefore relevant to have a physical model of the observed vacuum dynamics. This dynamics is not only determined by the pumping mechanism of the SIPs but also by conductance of the whole system and the dispenser sourcing effect. Understanding this dynamics would allow, for instance, the design of miniature SIPs [90] and avoid the use of pressure gauges improving the compactness of the experiments.

To reach a good fidelity in estimating the pressure at the vacuum chamber, we

develop an accurate calibration procedure to quantify the leakage current in the SIP. To achieve this goal, we first model the conductance of the vacuum system. Then, using the model and a protocol based on a pulsed dispenser current, we measure the temporal evolution of the pressure in the system. As we will see, the physical parameters describing the pressure dynamics extracted in this way, allow the reduction of the dead time in cold-atom experiments by combining a fast loading rate of cold-atom clouds (high partial ^{87}Rb pressure regime) and a fast removal of background atoms after the production of these clouds [90]. It is worth mentioning that the commonly used models [93, 94] for the SIP pumping speed do not explain the important pressure variations (more than 2 orders of magnitude) we observe. In fact, on measurement time scales of several minutes, the nature of the dominant pumping mechanism changes, and this effect needs to be taken into account.

6.1 Theoretical background

We consider a single-vacuum-chamber system, as represented in Fig. 6.1, which correspond to our experimental vacuum system. It is a simplified configuration containing a chamber of volume V_1 with the atom source (dispenser) that produces a flow $Q(t)$ that goes to a pump with a nominal pumping speed S. The pump and the chamber are connected through a pipe with a conductance C. With these definitions, we can then relate the pressure at the chamber $P_1(t)$ to the pressure at the pump $P_2(t)$. In a steady state ($t \to \infty$), neglecting leaks and in the free molecular regime, these quantities are related by the equation of the steady-state sourcing flux $Q(\infty)$:

$$Q(\infty) = C(P_1(\infty) - P_2(\infty)) = SP_2(\infty) = S_{\text{eff}}P_1(\infty), \tag{6.1}$$

where S_{eff} is the effective pumping speed seen by the chamber as determined by C. More generally, P_1 follows the gas balance equation [95]:

$$V_1 \frac{\mathrm{d}P_1(t)}{\mathrm{d}t} = Q(t) - S_{\text{eff}}P_1(t). \tag{6.2}$$

Since the characteristic pumping time $\tau_P \equiv V_1/S_{\text{eff}}$ controls the pressure transients in the vacuum system, S_{eff} needs to be properly determined. This is an important

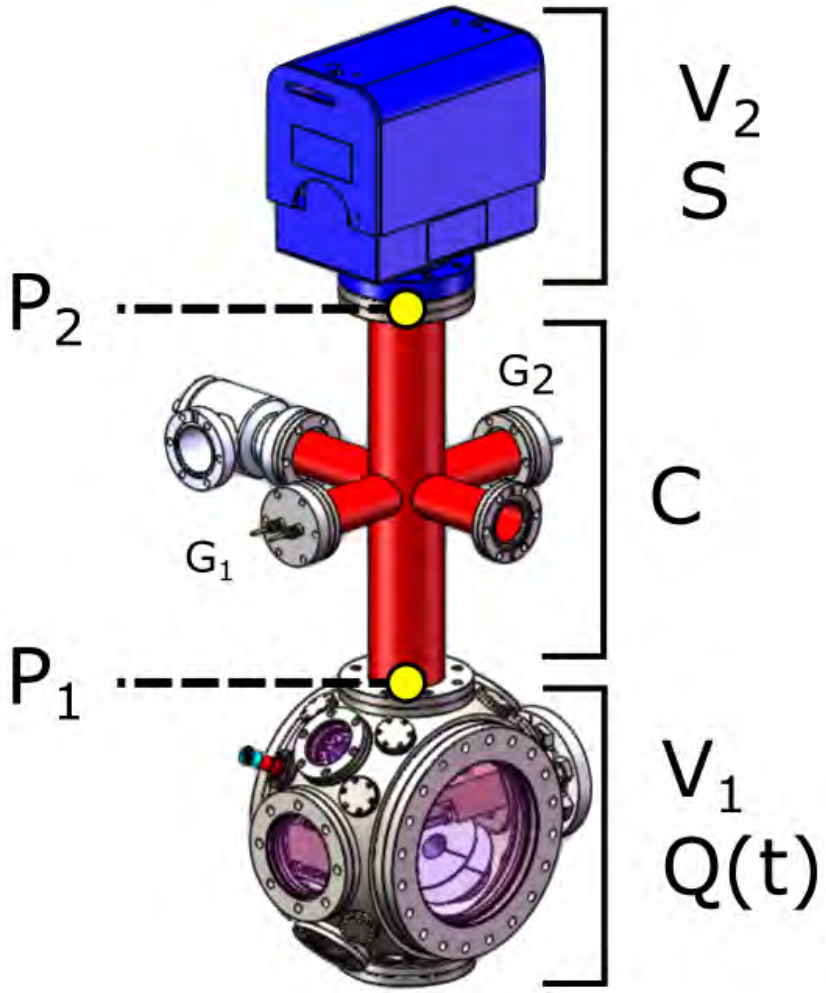

Figure 6.1: Sketch of the considered experimental setup. The vacuum chamber of volume V_1 contains the atom source producing a flow $Q(t)$. This gas at a pressure $P_1(t)$ in the chamber produces a pressure $P_2(t)$ at the pump through a pipe of conductance C. In the pump volume V_2, the atoms are pumped at a nominal speed S. Also represented in this figure are deactivated getter pumps G_1 and G_2.

question in particular for cold-atom experiments with time-dependent sources of alkali atoms.

6.1.1 The electrical analogy

One way to address the determination of S_{eff} is to use an analogy between a vacuum system and an electric circuit. The electrical analogy allows not only to calculate S_{eff} in a steady state, but also to evaluate our vacuum system as a low-pass filter [95]. This would not only allow us to model the response of our vacuum system to ^{87}Rb pressure pulse but also allow to model pressures modulations. With such a tool in our hands we can then consider dynamic regimes of molecule desorption from our alkali dispenser in order to see what would be the best strategy in order to reduce our experimental dead time. Following this idea we can give an electrical equivalent of our vacuum system in Fig. 6.2. In 6.2 a single science chamber con-

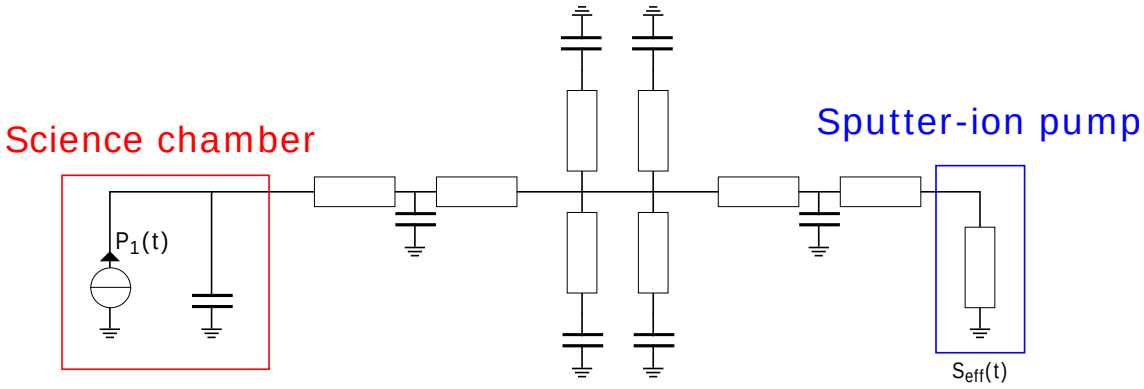

Figure 6.2: Electrical analogy of our single vacuum chamber system. The elements inside the red frame corresponds to the science chamber, the elements in the blue frame correspond to the ion pump. In this analogy, pressure act as voltage, volume act as a capacitance, and electrical and vacuum conductance are equivalent.

taining a dispenser is connected to an ion pump through a tube as you can see in Fig.6.1. Perpendicular to the principal tube are four small tubes connected to the feedthroughs for electrical connections including getter pumps that can be activated for further purpose of increasing pumping speed. According to the analogy, the dispenser would be a current generator, the tubes with certain volume would be an electrical conductance with capacitance, and the pump a conductance to ground. Furthermore, free software like Molflow+ [96] allow users to load 3D models of their

vacuum setup and model the conductivity and parameters of vacuum elements which could then be applied in an electrical analogy. Molflow+ is still under development, and the last versions implemented the possibility to see the pressure evolution (in time) through the vacuum setup. However, this software does not implement time dependent outgasing and pumping in the vacuum setup. Such feature in a software would make it essential to address any pressure related aspect of a cold atom experiment.

However, in order to use this analogy there are two major issues. Indeed, the time dependence of $P_1(t)$ as a current generator from the alkali dispenser is unknown, and more importantly, the time dependence of $S_{\text{eff}}(t)$ is also unknown. SIPs pumping speed are actually dependent on the pressures of the different species to pump. This work will then address the modeling of the SIP used in our vacuum system and study the pumping dynamics of our vacuum system.

6.2 Experimental Results

Another particular point that we need to take into consideration in our study of the pumpings dynamics, is the pressure readings. In our experimental setup the SIP, a TiTan$^{\text{TM}}$ 45S ion pump with a pumping rate of 40 L/s from Gamma Vacuum, is used itself as a ion gauge. This of course impose us to be cautious as the element we want to study (the SIP) is also the element which give us our pressure reading.

6.2.1 Leakage current of the Sputter Ion Pump

Normally, the pressure is translated into current readings by the pump controller. However, in the presence of alkali gases there exists a modification of the pump leakage current I_l [97]. This modification is responsible for an overestimation of the real pressure. It originates from a thin layer of alkali ions stuck to the pump walls. Together with I_l there is also an ion current I produced by the ionization of the gas flowing through the pump electrodes. These two currents contribute to the measured current I_m actually reported by the pump controller (the current reading).

The leakage current I_l is typically on the order of 100 nA and it is usually neglected in high vacuum regimes (it corresponds to an overestimation of $\simeq 10^{-9}$ mbar).

However, neglecting this current affects the use of the ion pump as a pressure gauge in the UHV regime [95] ($< 10^{-9}$ mbar). So, we include the effect of this current in the analysis below.

Following ion-pump manufacturers and taking into account that $I = I(P_2)$ is a function of the pressure at the pump, we have the following expression for I_m:

$$I_m(U) = I(P_2) + I_l = f(P_2) \times U + I_l \tag{6.3}$$

where U is the applied voltage between the pump electrodes. From this equation, we see that an accurate determination of the actual pressure (P_2 or I) requires a precise knowledge of the leakage current. The usual way of finding I_l is to measure I_m while the pump's magnets are removed. In this situation, there is no ionization process and we have $I = 0$ A. However, this method requires the pump to be stopped and does not allow a real-time monitoring of the pressure.

Here, we measure I_l by gradually decreasing U within the nominal working range of the pump [97]. Following Eq. (6.3), the leakage current is then determined by extrapolating the data to $U = 0$ V. The result of this measurement is presented in Fig. 6.3, where the observed linear behavior indicates that the pressure P_2 does not depend on the applied voltage U at the pressure levels we perform the experiment. The obtained value of the leakage current is $I_l = 119.0 \pm 0.4$ nA. As we will see in the following section, the accuracy in the pressure measurement obtained with this method allows us to model the pumping dynamics for pressures $< 10^{-9}$ mbar.

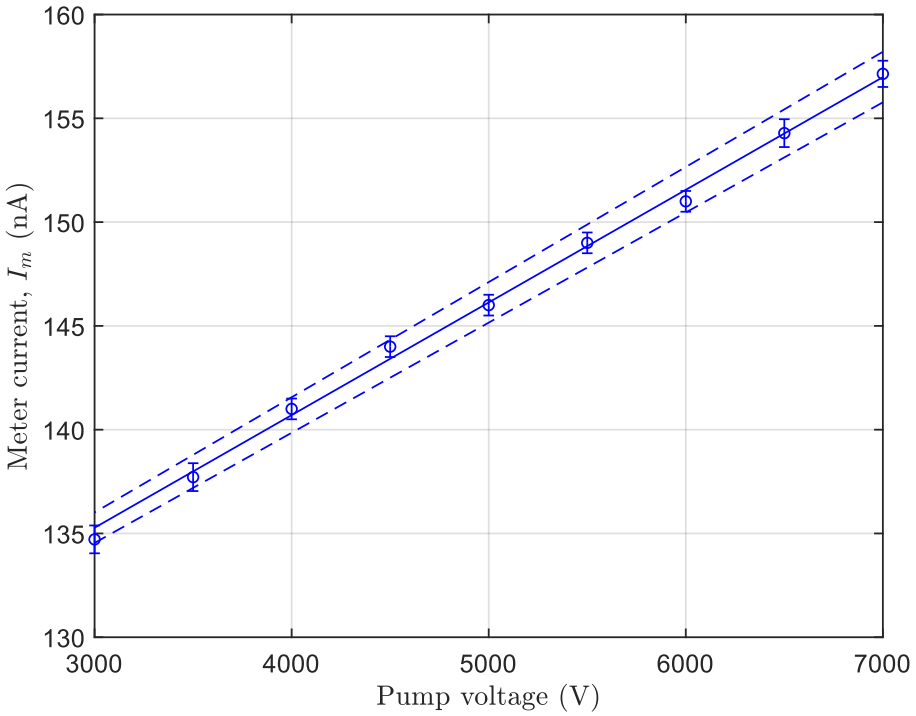

Figure 6.3: Current-voltage (I-V) characteristic of the pump. The leakage current $I_l = 119.0 \pm 0.4$ nA is obtained from a linear fit (solid line) of the measured current I_m. Dashed lines represent the confidence interval of the fitting parameters.

6.2.2 Determination of the pressure using an SIP

Once the leakage current is found, we can evaluate the ion current inside the pump $I(P_2)$ using Eq. 6.3 and the current reading I_m. The next problem is then to determine the explicit dependence of the ion current on the pressure at the pump, $f(P_2)$. Then we can invert the function $f(p_2)$ and, in the steady-state regime, compute the pressure at the chamber using Eq. 6.1, namely:

$$P_1 = \left(\frac{S}{C} + 1\right) P_2. \tag{6.4}$$

In the free molecular regime, the conductance C depends only on the geometry of the vacuum system for a given gas species and temperature. Using the Santeler equation [98] for the transmission probability through a cylindrical pipe of radius R and length L, we can calculate the conductance for a molecule of mass m at room temperature using the following relation [95]:

$$C \simeq 11.75\pi R^2 \sqrt{\frac{m_{N_2}}{m}} \left(1 + \frac{3L}{8R}\left[1 + \frac{1}{3(1 + L/7R)}\right]\right)^{-1}. \tag{6.5}$$

In Eq. (6.5) m_{N_2} is the mass of a nitrogen molecule, and R and L must be expressed in cm to get C in $\mathrm{L \cdot s^{-1}}$. Now, let us get an estimate of the value of S for our vacuum system. In a constant-flow regime, the conductance of our particular geometry (central pipe of $L = 35.2$ cm and $R = 3$ cm) evaluates to $C = 32\ \mathrm{L \cdot s^{-1}}$ for the ^{87}Rb monoatomic gas. This value is obtained neglecting contributions from the cross, which is a reasonable assumption in the constant flow regime. Finding S precisely is slightly more difficult when considering pumping of ^{87}Rb atoms. However, following the pump manufacturer's documentation [97] we can use the linear relation:

$$P_2 = \alpha k \frac{I}{U}, \tag{6.6}$$

in order to express the pressure at the pump in terms of the ion current. Here, $k = 10.9\ \mathrm{mbarVA^{-1}}$ at room temperature and α is a calibration factor. This factor is the ionization vacuum gauges' correction factor, which links the pressure measurement of specific gas species to calibration measurements using nitrogen. For Rb, $\alpha = 4.3$ [99]. As we see later, the empirical relation Eq. (6.6) does not take into account the fact that the actual relationship between the pressure P_2 and the ion current in the pump I is nonlinear.

With our MOT, we can realize an independent measurement of P_1 instead of computing it using Eq. (6.5). From the loading curve of the MOT, as shown in Fig. 6.4, we can find P_1 as indicated in Appendix C and Refs. [100, 101]. In fact, the loading dynamics of the MOT critically depends on the background pressure of the trapped species and other gases. As has been demonstrated in the past [83, 85, 100, 101], these curves produce reliable pressure measurements. In our experimental setup we use a mirror MOT obtained with an atom chip. The relevant experimental details are as follows: the red-detuned cooling lasers (-1.5Γ where $\Gamma = 2\pi \times 6$ MHz is the natural line width of ^{87}Rb D2 line) have a maximum power of $\simeq$ 40 mW shared by four independent MOT beams of about 2.5 cm of $1/e^2$ diameter. The magnetic field gradient is 11 G $\cdot$ cm^{-1}. During 100 s of loading, the fluorescence emitted by the atoms is collected on a photodiode with a solid angle of 1.3×10^{-2} srad. This signal is used to compute the atom number. In order to vary the pressure P_1, we change the dispenser current to produce different stationary gas flows Q.

In analogy to Eq. (6.6), we assume that the ion current I is proportional to the pressure at the vacuum chamber P_1, measured with the MOT. That is $I = \beta P_1$, where β is a parameter to be experimentally determined. Then, we can write the following equation for the ion current reading as a function of the pressure I_m:

$$I_m = I_l + \beta P_1 \tag{6.7}$$

In Fig. 6.5 we plot the dependence of I_m on the pressure P_1 measured from MOT loading curves at steady state. This result offers one independent method to validate the assumption leading to Eq. (6.7). This method consists in finding the leakage current from MOT measurements and comparing the obtained value with the one extracted from the I-V characterization. Fitting the data in Fig. 6.5 using Eq. (6.7), we find for I_l a value of 130 ± 20 nA, in good agreement with the result given by the I-V characterization presented in Fig. 6.3. This agreement supports the use of β to compute the pressure in the vacuum chamber by the relation $P_1 = I/\beta$. For the parameter β we obtain the value of $(9.2 \pm 0.6) \times 10^{10}$ nA $\cdot$ mbar^{-1}.

Let us note, however, that the MOT being loaded when the pressure reaches a steady-state regime, we have no guarantee that the relation $P_1 = I/\beta$ stays valid in a dynamic regime. It would also be tempting to use the information from Eq. (6.5),

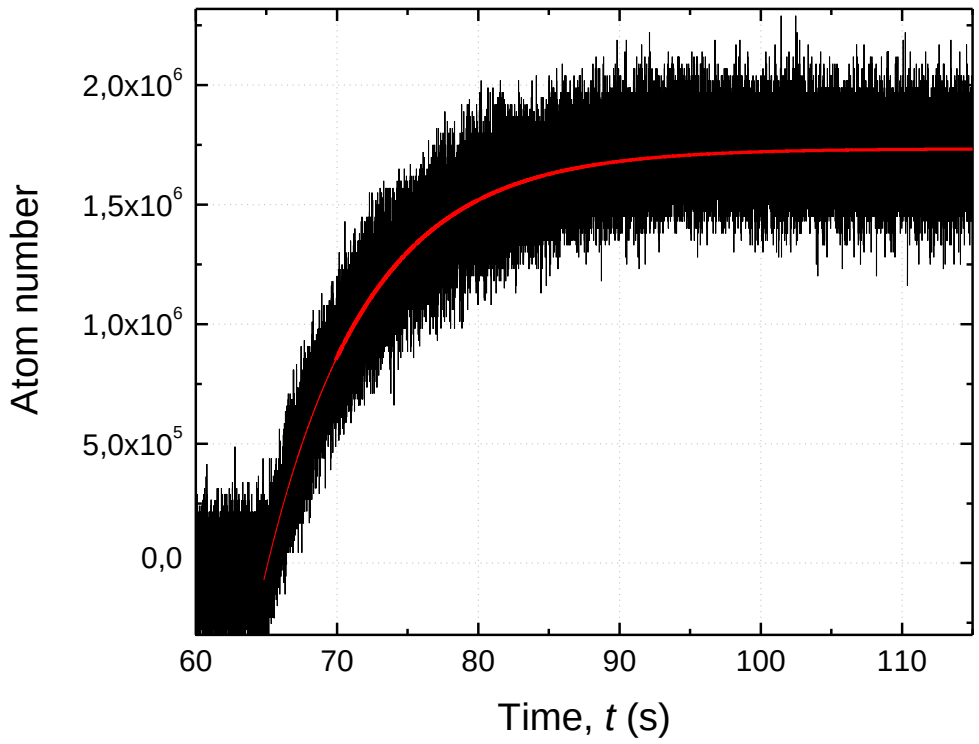

Figure 6.4: Number of ^{87}Rb atoms loaded in the MOT (black) for a dispenser current of 4.75 A. The fit (red solid line) to the experimental data gives a characteristic loading time of 7.13 ± 0.02 s.

Eq. (6.6) and Eq. (6.7) to find the pumping speed S. As determining β is equivalent to determining S_{eff} in a steady state. However, as we will see in the next section, constant pumping speeds do not properly describe the transient behavior of the pressure when switching on and off the dispenser current.

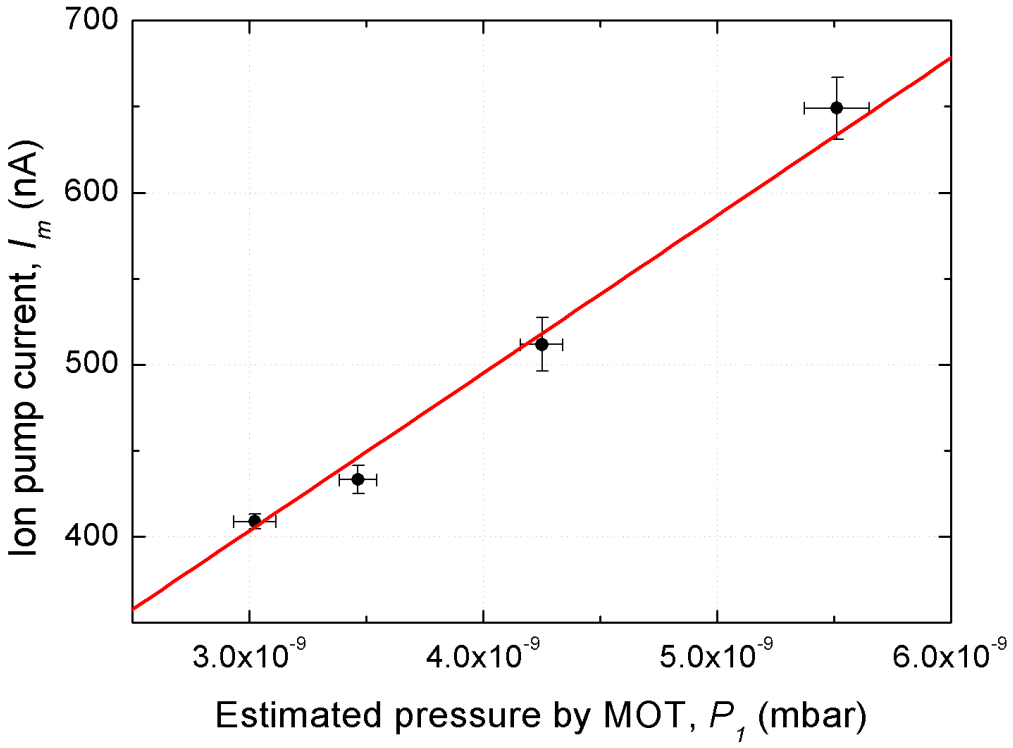

Figure 6.5: Meter current versus measured pressure P_1 from MOT loading curves (points). The leakage current I_l and the parameter β extracted from the fit (solid line), using Eq. (6.7), are respectively equal to 130 $\pm$ 20 nA and (9.2 $\pm$ 0.6) $\times$ 10^{10} nA.mbar^{-1}.

6.3 Analysis of the nonlinear pumping dynamics

6.3.1 Derivation of the dynamics

When searching for the reduction of the vacuum-system contribution to the dead time between interferometric measurements, we need to focus on the pump-down dynamics that is triggered after loading the MOT and switching off the atom source (dispenser). To achieve this goal, we devise a pressure measurement protocol, which is as follows: first, we switch on the dispenser at a given current and monitor the pressure rise until it reaches the steady state [101]. The current ranges from 3.75 to 5 A, with a step of 0.25 A. Then, we switch off the dispenser and record the pressure decay (pump-down curve) until it goes back to the steady state. We allow both of the transient processes to last for about 1000 s.

In the following, we develop a mathematical formalism to describe the main physical processes taking place during the pump-down dynamics. Firstly, we assume that the dispenser is no longer sourcing atoms into the chamber after being switched off. In this case, we can consider that the pressure evolution is mainly due to the pumping by the SIP in the presence of a residual outgassing flow $Q(t)$ coming from the vacuum chamber. In steady state, $Q(t)$ is solely given by the thermal outgassing in the system. Secondly, we suppose that the pump contains an ensemble of Penning cells with the geometry sketched in Fig. 6.6. Thirdly, let us assume that at the time instant t:

1. there already exists some sputtered pumping material (e.g. Ti) that pumps the gas, reducing the pressure by an amount $-aP_2(t)\,\mathrm{d}t$ (process ⓐ in Fig. 6.6);

2. some trapped molecules are released by the incident ion flux increasing the pressure by $cI(t)\,\mathrm{d}t$ (process ⓓ in Fig. 6.6);

3. some pumping material sputtered by the ion flux pumps the gas, reducing the pressure by $-aP_2(t) \times bI(t)\,\mathrm{d}t$ (process ⓔ in Fig. 6.6).

In point 1 above, the coefficient a represents the probability rate at which a particle reaching the cathode (made out of a pumping material) sticks to it. Furthermore, when the gas molecules gets ionized inside the pump (ⓑ in Fig. 6.6), the applied voltage accelerates the ions (ⓒ in Fig. 6.6) towards the cathode. If the

ions have sufficient energy they can release previously trapped particles (when they collide with the walls) with a desorption rate proportional to c (point 2) and also, they can sputter pumping material with a yield characterized by the coefficient b (point 3).

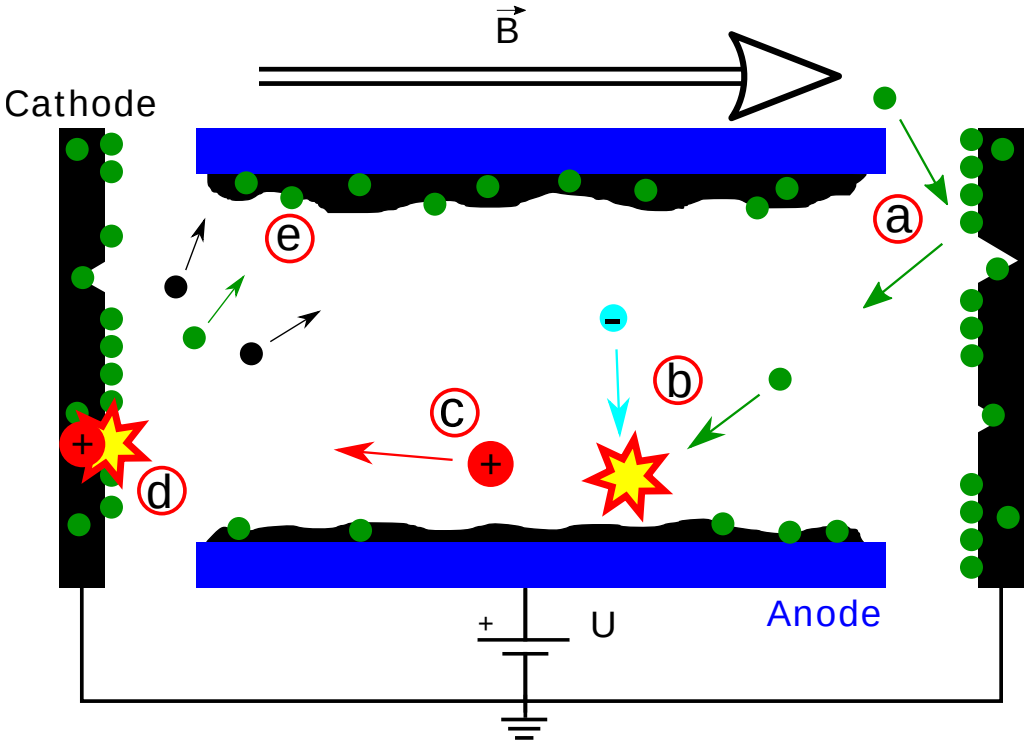

Figure 6.6: Cross-section of a Penning cell (a pumping unit cell). A high voltage U is applied between the cylindrical anode (blue), covered by some getter material (black), and the cathode (black). A gas particle (green) enters the pumping cell and hits the cathode (ⓐ) where it is stuck or deflected towards the anode. On its way to this electrode, the particle collides with an electron (ⓑ) and gets ionized. The ion is then accelerated towards the cathode (ⓒ) with eventually enough energy to be buried and sputter pumping material (ⓓ). The freshly sputtered material covers the internal walls of the cylindrical anode (ⓔ), which is then ready to pump more particles.

The physical processes we just described are in agreement with the fact that the pumping speed of the SIP decreases when the pressure decreases. The reason is the decrease of the discharge intensity (current per unit pressure) in this situation. This reduction of the pumping speed depends strongly on the pump parameters such as the applied anode voltage, the magnetic field, and the geometry of the pumping cell.

Collecting together the above-mentioned processes, we arrive at the following differential equation for the pressure evolution at the pump:

$$\frac{\mathrm{d}P_2(t)}{\mathrm{d}t} = -aP_2(t) - aP_2(t) \times bI(t) + cI(t) + \frac{Q(t)}{V_2}, \tag{6.8}$$

where V_2 is the pump volume. In the next section we use this model to fit the experimental data and determine the physical parameters defining the nonlinear dynamics.

6.3.2 Practical fitting model

Instead of working directly with the pressure Eq. (6.8), here we derive a practical model that allows a fitting of the experimental data. Our meter outputs current values and therefore, it would be more natural to work with the ion current I(t) rather than the pressure $P_2(t)$. However, the physical processes we just discussed indicate that we cannot use Eq. (6.6) to relate these quantities. Indeed, $I(t)$ has a nontrivial dependence on the pressure governed by the pressure regime the pump is working in. This fact is encoded by the empirical equation [91]:

$$I = hP_2^n \tag{6.9}$$

where the exponent n is a real number used to identify the different pressure regimes. It depends on the gas species and the geometry of the pump, and is determined from the fitting procedure. In Eq. (6.9), h is a time-independent calibration parameter defined by the type and size of the pump.

Inserting Eq. (6.9) into Eq. (6.8) we obtain the following equation in terms of the ion current:

$$\frac{\mathrm{d}I(t)}{\mathrm{d}t} = -\alpha_1 I(t) - \alpha_2 I(t)^2 + [\alpha_3 I(t) + q] \times I(t)^{1-(1/n)}, \tag{6.10}$$

with $\alpha_1 \equiv na$, $\alpha_2 \equiv nab$, $\alpha_3 \equiv nc\sqrt[n]{h}$, $q \equiv n\sqrt[n]{h}\,Q_{\mathrm{th}}/V_2$. These parameters are treated as independent and used in the fitting procedure. When writing Eq. (6.10) we consider that after switching off the dispenser, $Q(t)$ reaches the constant thermal outgassing flux Q_{th} in a time scale shorter than the time frame required to reach the steady state. As we will see later, such an approximation is compatible with our observations. We measure the pump-down curves presented in Fig. 6.7. The points

are the experimental data and the solid lines are fits obtained with Eq. (6.10). As can be seen in this figure, there is a very good agreement between the theory and the experimental data.

To validate the model beyond the criteria set by the fit quality, we study the dependence of the fitting parameters on the pressure P_2 looking at their behavior in different pressure regimes. The measurement protocol used is as follows: we change the dispenser current and wait until the pressure reaches an equilibrium state. Next, we measure the ion current at this equilibrium situation, before switching off the dispenser. Finally, we start the measurement of the pump-down dynamics. The results obtained with this protocol are presented in Fig. 6.8. It shows the dependence of the fitting parameters on the initial ion current.

As expected, the value of n increases when the pressure goes down [102] as can be seen in Fig. 6.8e. Moreover, it reaches unity at the highest measured pressure. The obtained value in this latter case is actually compatible with pump manufacturers' reported values for air. At low pressures it goes beyond 1.5, a value never reported before to our knowledge and that might be in agreement with the fact that we are pumping an alkali gas.

The parameter a, according to our model, depends on the pump's cathode geometry (the getter area) and the sticking factor, this latter being a function of the temperature and the gas species. From the measurement in Fig. 6.8a we see that at low initial ion currents (pressures) a is relatively constant. This is expected since in this case the sticking probability should correspond to a linear process given the gas density in the pump. However, when the initial ion current is increased, a, which seemed constant, eventually increases (up to a factor 5), suggesting either a modification of the sticking probability or an increase of the getter area. Both would seem unlikely as the pump geometry does not change and neither does the the species, nevertheless, this is coherent with the fact that in this situation the behavior of n also indicates a change in the pressure regime, a higher pressure leading to a higher bombardment rate of the cathode (from the ion). This could lead to induce an important surface roughness to the cathode, therefore, increasing the effective area of the getter. Furthermore, a higher bombardement rate would lead to heat dissipation in the cathode, therefore, an increase of the sticking factor as sticking factors

have been showed to be temperature dependent [103]. It is likely that we have an accumulation of both phenomena explaining such an increase. Let us note that this is also coherent with n getting close to 1, leaving therefore α_1 and α_3 multiplied by the same power of $I(t)$. It is therefore not impossible that the fitting algorithm is not capable to make the difference between α_1 and α_3 in this pressure regime.

From Fig. 6.8b we see that the parameter b tends to zero when the initial ion current is increased. This is also an expected behavior since this parameter is related to the discharge current, which is depressed by the space-charge effect when the pressure rises. As a consequence, the sputtering rate becomes reduced [91]. In fact, what happens is that at relatively high initial ion currents or pressures, the energy of the ions hitting the cathode is no longer exclusively defined by the applied voltage U.

In order to interpret the behavior of the parameters c and Q_{th} we need to isolate them from the calibration factor h. This requires us to perform independent measurements. However, it is fair to consider h as a scaling factor in Fig. 6.8c and Fig. 6.8d. In this situation, the increase of c with the initial ion current might be a consequence of the bombardment boost in the presence of a significant number of gas particles in the pump volume. This process naturally leads to a relatively higher desorption rate of buried molecules. Increasing the initial ion current also leads to an increase in the thermal outgassing flux Q_{th} in the time scale we record the data (approximately 1000 s). This effect is already observable in Fig. 6.7 where the steady-state ion-current value depends on the dispenser current.

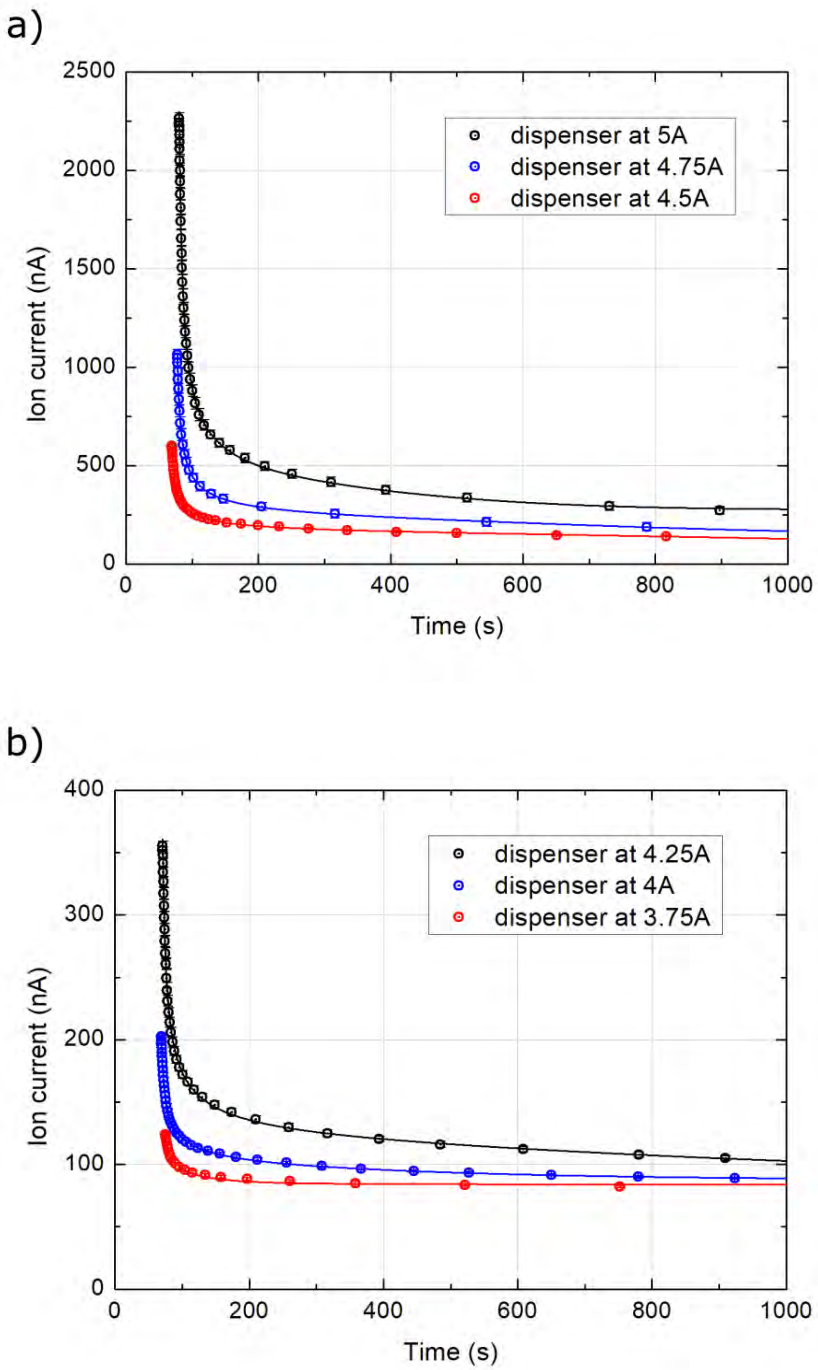

Figure 6.7: We record the pump-down curves (data points) after switching off the dispenser currents, initially at levels given in captions (a),(b). In each case, the measured ion current $I(t)$ is fitted (solid lines) by numerical integration of Eq. (6.10)). (a) Dispenser currents are 5 A (black circles), 4.75 A A (blue diamonds), and 4.5 A (red squares). (b) Dispenser currents are 4.25 A (black circles), 4 A (blue diamonds), and 3.75 A (red squares).

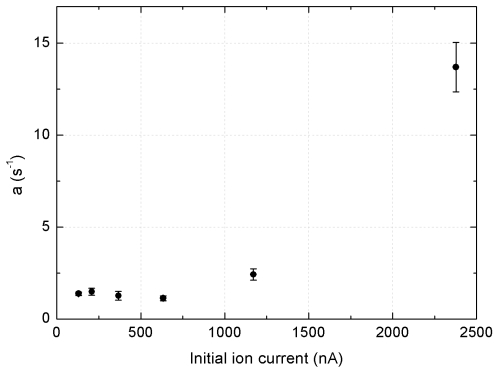

(a) Former sputtered-material pumping-rate parameter.

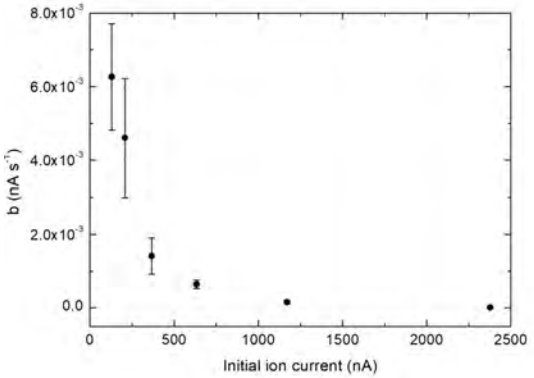

(b) Instantaneous ion flux induced sputtering pumping rate parameter.

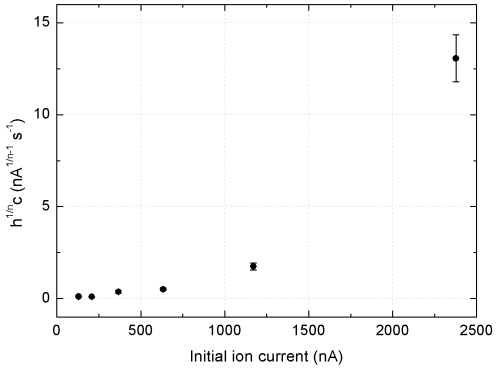

(c) Ion-flux desorption parameter.

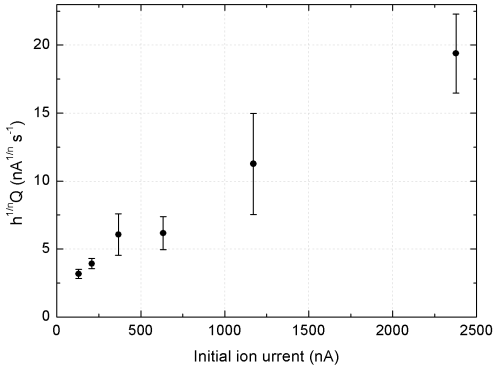

(d) Thermal outgassing source parameter.

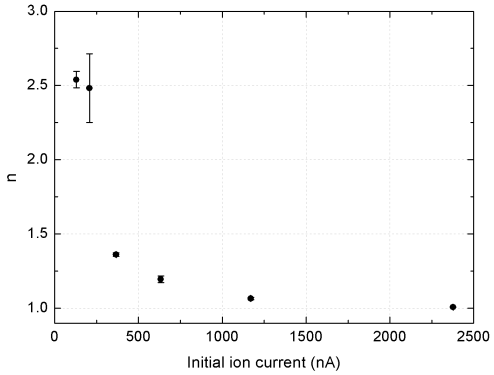

(e) Pumping regime parameter.

Figure 6.8: Dependence to initial ion current (when dispenser is switched-off) of the parameters describing the pumping physical processes. These parameters result from the fitting in Fig. 6.7 using the numerical solution of the differential Eq. (6.10).

6.4 Conclusion

In this work, we developed a detailed physical model of the nonlinear pressure dynamics in sputter ion pumps as well as a calibration method to determine the systematic error which is I_l without stopping the pumping. The model developed is experimentally corroborated by the measured data. It includes parameters describing the complex physical processes taking place inside the vacuum pump. Moreover, we characterize the system conductance and use pressure measurements with a MOT to establish a link between the pressure in the vacuum chamber and the ion current provided by the pump, at a steady state regime. From a practical point of view, this relationship allows the pump current to be used as a good indicator of the pressure in the science chamber even in a dynamic regime as it give us a magnitude for our pressure in the science chamber. From the observed dynamics, we can tailor the effective pumping speed and optimize the MOT loading time with respect to the contradictory requirements of having high repetition rates and high number of atoms in a single chamber. Furthermore, it is still possible to calibrate the relation between $P_1(t)$ and $P_2(t)$ by determining h. The calibration of h, our model and software as Molflow+ [96] would open the possibility to numerically simulate the the pressure dynamics inside our vacuum chamber. This would then open the possibilities to address numerically a huge variety alkali dispenser desorption pulse, in terms of time and intensity, in order to minimize the dead time of the experiment. We hope that the physics investigated in this work will be useful in the future to engineer miniature and microscopic scale ion pumps [90] for cold-atom-based compact quantum sensors.

Chapter 7

Summary, conclusion and outlook

In this thesis we have addressed the work done towards the realisation of an atom-chip gyro. We have looked at the key physical aspects as well as the technical requirements needed to realise such device.

The effect of temperature on the propagation and the interferences of a wavepacket (Chapter 2 and Chapter 3)

We studied the propagation and interference of a 1D wavepacket using density matrix formalism from quantum optics. We extended this representation using the Glauber-Sudarshan P-function to introduce the temperature as a superposition of coherent states wavepackets, then see the effect of the temperature on the spreading and interference fringes. As a result, we have developed and presented a new formalism and canonical form which highlights physical behavior and creates an intuitive picture of the integration of the P-function over the coherent space. It also opened the question of entropy aspects with a possible relation between the temperature and the linear entropy of mixed states that we hope could be addressed in the future. This formalism was extended further when addressing the interference of thermal wavepackets in simple and näive configurations. It opens a perspective on the application of this formalism to experimental interferometers where the interference signature is measured through cloud population after a $\pi/2$-pulse, with a discussion

on the effect of temperature on the contrast of the interferometer.

The fabrication of atom-chips with thick metal deposition with the smallest possible roughness of wires (Chapter 4)

For the fabrication, we characterised a PVD process to grow wires by a negative photolithography lift-off. This process was used to fabricate an atom-chip being currently used in the GyrAChip experiment at SYRTE. Moreover, we showed how we could push the electrodeposition processes to obtain even thicker metal deposition, thicker than those achievable through PVD, capable of achieving a surface roughness limited only by the choice of the substrate and the quality of the photolithography. We also discussed how electrodeposition processes could still be pushed further to achieve even lower surface roughness. This pushing of the process will soon become a technical necessity as progresses are being made in the production of mono-crystal AlN substrates. This mono-crystal AlN should achieve surface roughness comparable to what can be achieved with Si substrate. Such technological progress will not only improve the technical noise related to the roughness of the wires, but would also, thanks to improved heat dissipation, allow us to increase the power going through the wires, without destroying them.

The noise characterisation of floating current generator to be used on the atom-chip in order to trap and control atoms (Chapter 5)

The possibility to produce thick wires is also important when we consider the use of low noise current generators. Indeed the resistivity of the wires is a function of their thickness, thicker wires would allow us to increase the value of the current used which was before limited by the power of the current supply. We have characterised homemade current supplies through PSD measurement and showed that they have

a RMS relative noise $< 10^{-5}$. Depending on the way the magnetic potential is generated by the wire patterns, it is possible to relate the current noise measured through the PSD to atom's phase noise by using the auto-correlation function and its relation to PSD. This relation would allow us to see the viability of generating ring traps for gyroscopes.

The pumping dynamics of a single chamber cold atom experiment in order to reduce the experiment dead-time (Chapter 6)

Finally, we presented a study of the pumping dynamics of an ion pump in a single chamber cold-atom experiment. This study characterised the capacity of the pump to restore a High Vacuum level after a burst of atom vapour is produced in the science chamber. This study was undertaken to explore the possibility of reducing the loading time for MOT. We showed, in this study, new techniques to improve the pressure reading of ion pumps by increasing its accuracy, measuring leakage current without having to turn off the pumps and disassemble its magnets. We also presented a pumping model which perfectly fits a pressure decay during a pumping phase within time scale of several minutes. This study could be used by in the future by those who want to design quantum sensors with reduced dead time as this study helps in the understanding of pump dynamics.

There is still a lot of work needed in order to achieve this project, but we were able, in this thesis, to contribute to several characterisations of individual elements used in the experimental setup. Furthermore, this thesis was able to propose new contributions to the scientific community through a published pumping model for ion pumps, a new formalism for thermal wavepackets, and possibilities to improve the quality of atom-chip fabrication through the study of involved processes.

Appendix A

P-representation

Here I will focus on the known demonstration of the P-function for a thermal distribution of coherent states. For this calculation we will define:

- $\mathcal{P}(\alpha)$ the P-function of the coherent state $|\alpha\rangle$, defined as:

$$\hat{\rho} = \iint \mathcal{P}(\alpha) \, |\alpha\rangle \, \langle\alpha| \, d^2\alpha, \tag{A.1}$$

- The density matrix defined as:

$$\hat{\rho} = \sum_i \mathsf{p}_i \, |\Psi_i\rangle \, \langle\Psi_i| \, , \tag{A.2}$$

- $\mathsf{P}(n)$ the probability of $|n\rangle$ via any of the $|\Psi_i\rangle$ such as:

$$P(n) = \sum_i \mathsf{p}_i |\langle n|\Psi_i\rangle|^2. \tag{A.3}$$

A.1 The characteristic function and the P-function

We define the characteristic function of P-representation by:

$$(\lambda) = \mathrm{Tr}\Big[\hat{\rho} e^{\lambda \hat{a}^\dagger} e^{-\lambda^* \hat{a}}\Big]. \tag{A.4}$$

By substituting $\hat{\rho}$ by its definition with the P-function we can calculate the relation between the P-function and the characteristic function:

$$\begin{aligned}
\chi_p(\lambda) &= \mathrm{Tr}\left[\hat{\rho}e^{\lambda\hat{a}^\dagger}e^{-\lambda^*\hat{a}}\right] \\
&= \mathrm{Tr}\left[\left(\iint \mathcal{P}(\alpha)\,|\alpha\rangle\,\langle\alpha|\;d^2\alpha\right)e^{\lambda\hat{a}^\dagger}e^{-\lambda^*\hat{a}}\right] \\
&= \iint \mathrm{Tr}\left[\mathcal{P}(\alpha)\,|\alpha\rangle\,\langle\alpha|\,e^{\lambda\hat{a}^\dagger}e^{-\lambda^*\hat{a}}\right]d^2\alpha \\
&= \iint \mathrm{Tr}\left[\langle\alpha|\,e^{\lambda\hat{a}^\dagger}e^{-\lambda^*\hat{a}}\mathcal{P}(\alpha)\,|\alpha\rangle\right]d^2\alpha \\
&= \iint \mathcal{P}(\alpha)\,\mathrm{Tr}\left[\langle\alpha|\,e^{\lambda\hat{a}^\dagger}e^{-\lambda^*\hat{a}}\,|\alpha\rangle\right]d^2\alpha \\
&= \iint \mathcal{P}(\alpha)\,\mathrm{Tr}\left[\langle\alpha|\left(\sum_k \frac{(\lambda\hat{a}^\dagger)^k}{k\,!}\right)\left(\sum_j \frac{(-\lambda^*\hat{a})^j}{j\,!}\right)|\alpha\rangle\right]d^2\alpha \\
&= \iint \mathcal{P}(\alpha)\,\mathrm{Tr}\left[\sum_{k,j}\left(\frac{\langle\alpha|\,(\lambda\hat{a}^\dagger)^k}{k\,!}\right)\left(\frac{(-\lambda^*\hat{a})^j\,|\alpha\rangle}{j\,!}\right)\right]d^2\alpha \\
&= \iint \mathcal{P}(\alpha)\,\mathrm{Tr}\left[\sum_{k,j}\left(\frac{\langle\alpha|\,(\lambda\alpha^*)^k}{k\,!}\right)\left(\frac{(-\lambda^*\alpha)^j\,|\alpha\rangle}{j\,!}\right)\right]d^2\alpha \\
&= \iint \mathcal{P}(\alpha)\,\mathrm{Tr}\left[\langle\alpha|\left(\sum_k \frac{(\lambda\alpha^*)^k}{k\,!}\right)\left(\sum_j \frac{(-\lambda^*\alpha)^j}{j\,!}\right)|\alpha\rangle\right]d^2\alpha \\
&= \iint \mathcal{P}(\alpha)\,\mathrm{Tr}\left[\langle\alpha|\,e^{\lambda\alpha^*}e^{-\lambda^*\alpha}\,|\alpha\rangle\right]d^2\alpha \\
&= \iint \mathcal{P}(\alpha)e^{\lambda\alpha^*}e^{-\lambda^*\alpha}\,\mathrm{Tr}[\langle\alpha|\alpha\rangle]\,d^2\alpha \\
&= \iint \mathcal{P}(\alpha)e^{\lambda\alpha^*}e^{-\lambda^*\alpha}\times 1\,d^2\alpha \\
&= \iint \mathcal{P}(\alpha)e^{\lambda\alpha^*-\lambda^*\alpha}\,d^2\alpha. \qquad \text{(A.5)}
\end{aligned}$$

However, $e^{\lambda^*\alpha-\lambda^*} = e^{2i(\alpha_R\lambda_I-\alpha_I\lambda_R)}$ and $d^2\alpha = d\alpha_R d\alpha_I$ therefore we can say that $\mathcal{P}(\alpha)$ is the 2D Fourier transform of $\chi_p(\lambda)$, then:

$$\mathcal{P}(\alpha) = \frac{1}{\pi^2}\iint \chi_p(\lambda)e^{\lambda^*\alpha-\lambda\alpha^*}\,d^2\lambda. \qquad \text{(A.6)}$$

A.2 P-function for thermal state

In order to calculate the $\mathcal{P}(\alpha)$ for a thermal state we need to write $\chi_p(\lambda)$ with the density matrix of the thermal state. Therefore we write the known density matrix

for thermal states as:

$$\hat{\rho} = \sum_{j=0}^{\infty} \frac{\bar{n}^j}{(\bar{n}+1)^{j+1}} \left|j\right\rangle \left\langle j\right| . \tag{A.7}$$

Therefore we can calculate:

$$\begin{aligned}
\chi_p(\lambda) &= \mathrm{Tr}\left[\hat{\rho} e^{\lambda \hat{a}^\dagger} e^{-\lambda^* \hat{a}}\right] \\
&= \sum_{k=0}^{\infty} \left\langle k\right| \hat{\rho} e^{\lambda \hat{a}^\dagger} e^{-\lambda^* \hat{a}} \left|k\right\rangle \\
&= \sum_{k=0}^{\infty} \left\langle k\right| \left(\sum_{j=0}^{\infty} \frac{\bar{n}^j}{(\bar{n}+1)^{j+1}} \left|j\right\rangle \left\langle j\right| \right) e^{\lambda \hat{a}^\dagger} e^{-\lambda^* \hat{a}} \left|k\right\rangle \\
&= \sum_{k=0}^{\infty} \sum_{j=0}^{\infty} \frac{\bar{n}^j}{(\bar{n}+1)^{j+1}} \left\langle k|j\right\rangle \left\langle j\right| e^{\lambda \hat{a}^\dagger} e^{-\lambda^* \hat{a}} \left|k\right\rangle \\
&= \sum_{k=0}^{\infty} \sum_{j=0}^{\infty} \frac{\bar{n}^j}{(\bar{n}+1)^{j+1}} \delta_{kj} \left\langle j\right| e^{\lambda \hat{a}^\dagger} e^{-\lambda^* \hat{a}} \left|k\right\rangle \\
&= \sum_{k=0}^{\infty} \frac{\bar{n}^k}{(\bar{n}+1)^{k+1}} \left\langle k\right| e^{\lambda \hat{a}^\dagger} e^{-\lambda^* \hat{a}} \left|k\right\rangle \\
&= \sum_{k=0}^{\infty} \frac{\bar{n}^k}{(\bar{n}+1)^{k+1}} \left\langle k\right| \left(\sum_{j=0}^{\infty} \frac{(\lambda \hat{a}^\dagger)^j}{j\,!} \right) \left(\sum_{l=0}^{\infty} \frac{(-\lambda^* \hat{a})^l}{l\,!} \right) \left|k\right\rangle .
\end{aligned} \tag{A.8}$$

Since $\hat{a}\left|n\right\rangle = \sqrt{n}\left|n-1\right\rangle$ and $\left\langle n\right| \hat{a}^\dagger = \left\langle n-\right| \sqrt{n}$ we can therefore write:

If $j > k \Rightarrow \hat{a}^j \left|k\right\rangle = 0$ and $\left\langle k\right| (\hat{a}^\dagger)^j = 0$,

If $j \leq k \Rightarrow \hat{a}^j \left|k\right\rangle = \dfrac{\sqrt{k\,!}}{\sqrt{(k-j)\,!}} \left|k-j\right\rangle$ and $\left\langle k\right| (\hat{a}^\dagger)^j = \left\langle k-j\right| \dfrac{\sqrt{k\,!}}{\sqrt{(k-j)\,!}}$.

So we can now go back on our calculus:

$$\begin{aligned}
\chi_p(\lambda) &= \sum_{k=0}^{\infty} \frac{\bar{n}^k}{(\bar{n}+1)^{k+1}} \left\langle k\right| \left(\sum_{j=0}^{\infty} \frac{(\lambda \hat{a}^\dagger)^j}{j\,!} \right) \left(\sum_{l=0}^{\infty} \frac{(-\lambda^* \hat{a})^l}{l\,!} \right) \left|k\right\rangle \\
&= \sum_{k=0}^{\infty} \frac{\bar{n}^k}{(\bar{n}+1)^{k+1}} \sum_{j=0}^{k} \sum_{l=0}^{k} \left\langle k-j\right| \frac{\lambda^j}{j\,!} \frac{\sqrt{k\,!}}{\sqrt{(k-j)\,!}} \times \frac{\sqrt{k\,!}}{\sqrt{(k-l)\,!}} \frac{(-\lambda^*)^l}{l\,!} \left|k-l\right\rangle \\
&= \sum_{k=0}^{\infty} \frac{\bar{n}^k}{(\bar{n}+1)^{k+1}} \sum_{j=0}^{k} \sum_{l=0}^{k} \frac{\lambda^j}{j\,!} \frac{\sqrt{k\,!}}{\sqrt{(k-j)\,!}} \times \frac{\sqrt{k\,!}}{\sqrt{(k-l)\,!}} \frac{(-\lambda^*)^l}{l\,!} \left\langle k-j|k-l\right\rangle \\
&= \sum_{k=0}^{\infty} \frac{\bar{n}^k}{(\bar{n}+1)^{k+1}} \sum_{j=0}^{k} \frac{\lambda^j}{j\,!} \frac{\sqrt{k\,!}}{\sqrt{(k-j)\,!}} \times \frac{\sqrt{k\,!}}{\sqrt{(k-j)\,!}} \frac{(-\lambda^*)^j}{j\,!} \\
&= \sum_{k=0}^{\infty} \frac{\bar{n}^k}{(\bar{n}+1)^{k+1}} \sum_{j=0}^{k} \frac{(-1)^j}{j\,!} \frac{k\,!}{(k-j)\,!j\,!} (\lambda\lambda^*)^j \\
&= \sum_{k=0}^{\infty} \frac{\bar{n}^k}{(\bar{n}+1)^{k+1}} \sum_{j=0}^{k} \frac{(-1)^j}{j\,!} \binom{k}{j} (\lambda\lambda^*)^j .
\end{aligned} \tag{A.9}$$

Let's now introduce the Laguerre polynomials defined as:

$$L_n(x) = \sum_{k=0}^{n} \binom{n}{k} \frac{(-1)^k}{k!} x^k. \tag{A.10}$$

We can therefore write:

$$\begin{aligned}\chi_p(\lambda) &= \sum_{k=0}^{\infty} \frac{\bar{n}^k}{(\bar{n}+1)^{k+1}} \sum_{j=0}^{k} \frac{(-1)^j}{j\,!} \binom{k}{j} (\lambda\lambda^*)^j \\ &= \sum_{k=0}^{\infty} \frac{\bar{n}^k}{(\bar{n}+1)^{k+1}} L_k(\lambda\lambda^*).\end{aligned} \tag{A.11}$$

In order to go further, let's now introduce the generator function of the Laguerre polynomials:

$$\sum_{n=0}^{\infty} t^n L_n(x) = \frac{1}{1-t} \exp\left(-\frac{tx}{1-t}\right). \tag{A.12}$$

Therefore by writing $t = \bar{n}/(\bar{n}+1)$ we can keep the calculus as:

$$\begin{aligned}\chi_p(\lambda) &= \sum_{k=0}^{\infty} \frac{\bar{n}^k}{(\bar{n}+1)^{k+1}} L_k(\lambda\lambda^*) \\ &= \frac{1}{(\bar{n}+1)} \sum_{k=0}^{\infty} \frac{\bar{n}^k}{(\bar{n}+1)^{k}} L_k(\lambda\lambda^*) \\ &= \frac{1}{(\bar{n}+1)} \times \frac{1}{1-\frac{\bar{n}}{(\bar{n}+1)}} \exp\left(-\frac{\frac{\bar{n}}{(\bar{n}+1)} \times \lambda\lambda^*}{1-\frac{\bar{n}}{(\bar{n}+1)}}\right).\end{aligned} \tag{A.13}$$

However $\frac{1}{1-\frac{\bar{n}}{\bar{n}+1}} = \frac{\bar{n}+1}{\bar{n}+1-\bar{n}} = \bar{n}+1$, therefore we have:

$$\begin{aligned}\chi_p(\lambda) &= \frac{1}{(\bar{n}+1)} \times \frac{1}{1-\frac{\bar{n}}{(\bar{n}+1)}} \exp\left(-\frac{\frac{\bar{n}}{(\bar{n}+1)} \times \lambda\lambda^*}{1-\frac{\bar{n}}{(\bar{n}+1)}}\right) \\ &= \frac{1}{(\bar{n}+1)} \times (\bar{n}+1) \exp\left(-\frac{\bar{n}}{\bar{n}+1} \times \lambda\lambda^* \times (\bar{n}+1)\right),\end{aligned} \tag{A.14}$$

And finally,

$$\chi_p(\lambda) = \exp(-\bar{n} \times \lambda\lambda^*). \tag{A.15}$$

We can now finally substitute $\chi_p(\lambda)$ in Eq. (A.6):

$$\begin{aligned}\mathcal{P}(\alpha) &= \frac{1}{\pi^2} \iint \chi_p(\lambda) e^{\lambda^*\alpha - \lambda\alpha^*}\, d^2\lambda \\ &= \frac{1}{\pi^2} \iint \exp(-\bar{n} \times \lambda\lambda^*) \times e^{\lambda^*\alpha - \lambda\alpha^*}\, d^2\lambda \\ &= \frac{1}{\pi^2} \iint \exp\big(-\bar{n} \times (\lambda_I^2 + \lambda_R^2)\big) \times e^{2i(\alpha_R\lambda_I - \alpha_I\lambda_R)}\, d\lambda_R\, d\lambda_I \\ &= \frac{1}{\pi^2} \left(\int e^{2i\alpha_R\lambda_I} e^{-\bar{n}\lambda_I^2}\, d\lambda_I\right) \left(\int e^{-2i\alpha_I\lambda_R} e^{-\bar{n}\lambda_R^2}\, d\lambda_R\right) \\ &= \frac{1}{\pi^2} \left(\int e^{-2i\pi(\frac{-\alpha_R}{\pi})\lambda_I} e^{-\bar{n}\lambda_I^2}\, d\lambda_I\right) \left(\int e^{-2i\pi\frac{\alpha_I}{\pi}\lambda_R} e^{-\bar{n}\lambda_R^2}\, d\lambda_R\right).\end{aligned} \tag{A.16}$$

Now taking the definition of Fourier transform which is:

$$\mathcal{FT}\left[f(x)\right](k) = \int f(x)e^{-2i\pi\times kx}\,dx$$

, And therefore for a Gaussian function (where $f(x) = e^{-ax^2}$) we have:

$$\mathcal{FT}\left[e^{-ax^2}\right](k) = \sqrt{\frac{\pi}{a}}e^{-k^2\frac{\pi^2}{a}}$$

.

And so going back to $\mathcal{P}(\alpha)$ we have:

$$\begin{aligned}
\mathcal{P}(\alpha) &= \frac{1}{\pi^2}\left(\int e^{-2i\pi(\frac{-\alpha_R}{\pi})\lambda_I}e^{-\bar{n}\lambda_I^2}\,d\lambda_I\right)\left(\int e^{-2i\pi\frac{\alpha_I}{\pi}\lambda_R}e^{-\bar{n}\lambda_R^2}\,d\lambda_R\right)\\
&= \frac{1}{\pi^2}\times\mathcal{FT}\left[e^{-\bar{n}\lambda_I^2}\right]\left(\frac{-\alpha_R}{\pi}\right)\times\mathcal{FT}\left[e^{-\bar{n}\lambda_R^2}\right]\left(\frac{\alpha_I}{\pi}\right)\\
&= \frac{1}{\pi^2}\times\sqrt{\frac{\pi}{\bar{n}}}e^{-\left(\frac{-\alpha_R}{\pi}\right)^2\times\frac{\pi^2}{\bar{n}}}\times\sqrt{\frac{\pi}{\bar{n}}}e^{-\left(\frac{\alpha_I}{\pi}\right)^2\times\frac{\pi^2}{\bar{n}}}\\
&= \frac{1}{\bar{n}\pi}e^{-\frac{\alpha_R^2+\alpha_I^2}{\bar{n}}}.
\end{aligned} \tag{A.17}$$

And finally we can conclude for a thermal state as:

$$\boxed{\mathcal{P}(\alpha) = \frac{1}{\bar{n}\pi}e^{-|\alpha|^2/\bar{n}}}. \tag{A.18}$$

Appendix B

Gaussian wavepacket solution of the 1D free space Schrödinger equation

Colours in this appendix equations are here to help the eye.

We will consider here the propagation of a 1D wave-packet $\psi(x,t)$ in a free space as we make the approximation that a wave-packet propagation in a waveguide is equivalent to a free particle moving along the waveguide axis. This result is obviously known, however we will present an unusual representation of $\psi(x,t)$ such as $|\psi(x,t)|\exp(i\arg[\psi(x,t)])$ so we can directly see the probability density and the phase.

The Hamiltonian is then $\hat{\mathcal{H}} = \frac{-\hbar^2}{2m} \times \frac{\partial^2}{\partial x^2}$, therefore, we have the Schrödinger equation:

$$i\hbar\frac{\partial}{\partial t}\psi = \hat{\mathcal{H}}\psi, \tag{B.1}$$

therefore,

$$i\hbar\frac{\partial\psi(x,t)}{\partial t} = -\frac{\hbar^2}{2m}\frac{\partial^2\psi(x,t)}{\partial x^2}. \tag{B.2}$$

Let's write the general solution of Eq. (B.2) according to the Plancherel theorem:

$$\psi(x,t) = \frac{1}{\sqrt{2\pi}}\int e^{i(kx-\omega t)}\phi(k)\,dk, \tag{B.3}$$

where $\phi(k)$ is the momentum distribution of the wave-packet.

B.1 Normalization criteria

The criteria of normalization for ψ is:

$$\int_{-\infty}^{+\infty} \psi^* \psi \, dx = 1,$$

and we can show that:

$$\int_{-\infty}^{+\infty} |\phi(k)|^2 \, dk = 1. \tag{B.4}$$

Following the central limit theorem, if we chose a Gaussian distribution of the momentum in the wave-packet ψ then I have:

$$\phi(k) = \text{Const.} \times \exp\left(- \left(\frac{k - k_0}{2\Delta k} \right)^2 \right). \tag{B.5}$$

Where $k_0 = \langle k \rangle$, Const. is a normalization factor and the operator Δ defined by $\Delta\square^2 = \langle \square^2 \rangle - \langle \square \rangle^2$ such as Δk is the standard deviation in the momentum space. We then have the Heisenberg's incertitude principle:

$$\Delta k \Delta x \geq 1/2. \tag{B.6}$$

Therefore we can set our physical problem as a single atom of momentum $\hbar k_0$ (the recoil velocity for our experiment) with a standard deviation Δk.

Let's now calculate the value of Const.:

$$\int_{-\infty}^{+\infty} |\phi(k)|^2 \, dk = 1$$

$$= \int_{-\infty}^{+\infty} \left| \text{Const.} \times \exp\left(- \left(\frac{k - k_0}{2\Delta k} \right)^2 \right) \right|^2 dk$$

Therefore, if we assume Const. $\in \mathbb{R}^+$ and the fact that $\exp(\square) > 0$ for $\forall \square \in \mathbb{R}$, we can write:

$$\int_{-\infty}^{+\infty} \left| \text{Const.} \times \exp\left(- \left(\frac{k - k_0}{2\Delta k} \right)^2 \right) \right|^2 dk = \text{Const}^2 \times \int_{-\infty}^{+\infty} \exp\left(-2 \times \left(\frac{k - k_0}{2\Delta k} \right)^2 \right) dk = 1.$$

Therefore we can calculate Const. with:

$$\frac{1}{\text{Const.}^2} = \int_{-\infty}^{+\infty} \exp\left(-2 \times \left(\frac{k - k_0}{2\Delta k} \right)^2 \right) dk.$$

Therefore by using the Gaussian integral formula(with $a \in \mathbb{C}$ and $b \in \mathbb{C}$):

$$\int_{-\infty}^{+\infty} \exp\left(-a(x+b)^2\right) dx = \sqrt{\frac{\pi}{a}}, \tag{B.7}$$

we can then write:

$$\begin{aligned}\frac{1}{\text{Const.}^2} &= \int_{-\infty}^{+\infty} \exp\left(-\frac{2}{4\Delta k^2} \times (k-k_0)^2\right) dk \\ &= \sqrt{\pi \times \frac{4\Delta k^2}{2}} = \sqrt{2\pi}\Delta k\end{aligned}$$

So,

$$\text{Const.} = \left(\sqrt{2\pi}\Delta k\right)^{-1/2}. \tag{B.8}$$

Finally Eq. (B.5) become:

$$\boxed{\phi(k) = \left(\sqrt{2\pi}\Delta k\right)^{-1/2} \times \exp\left(-\frac{(k-k_0)^2}{4\Delta k^2}\right)}. \tag{B.9}$$

And therefore Eq. (B.3) become:

$$\psi(x,t) = \frac{1}{\sqrt{2\pi}} \int_{-\infty}^{+\infty} e^{i(kx-\omega t)} \times \left(\sqrt{2\pi}\Delta k\right)^{-1/2} \exp\left(-\frac{(k-k_0)^2}{4\Delta k^2}\right) dk. \tag{B.10}$$

B.2 Equation dependant of x

From Eq. (B.10) using $\omega = \frac{\hbar k^2}{2m}$ we can write:

$$\begin{aligned}\psi(x,t) &= \left((2\pi)^{3/2}\Delta k\right)^{-1/2} \int_{-\infty}^{+\infty} e^{i\left(kx - \frac{\hbar k^2}{2m}t\right)} \exp\left(-\frac{k^2 - 2kk_0 + k_0^2}{4\Delta k^2}\right) dk \\ &= \left((2\pi)^{3/2}\Delta k\right)^{-1/2} \times e^{-k_0^2/4\Delta k^2} \\ &\quad \times \int_{-\infty}^{+\infty} \exp\left[-k^2\left(\frac{i\hbar t}{2m} + \frac{1}{4\Delta k^2}\right) + k\left(\frac{2k_0}{4\Delta k^2} + ix\right)\right] dk.\end{aligned} \tag{B.11}$$

Let's name $A(t) = \frac{i\hbar t}{2m} + \frac{1}{4\Delta k^2} = \frac{2i\hbar t\Delta k^2 + m}{4m\Delta k^2}$ and $B(x) = \frac{2k_0}{4\Delta k^2} + ix = \frac{2ix\Delta k^2 + k_0}{2\Delta k^2}$ and we will construct a constant $C \in \mathbb{C}$ such as we can complete the square, therefore:

$$\begin{aligned}&-A(t) \times k^2 + B(x) \times k + C = -\text{Const.}(k - k_{eq})^2 \\ &\Rightarrow A(t)k^2 - B(x)k - C = \text{Const.}k^2 - 2\text{Const.}kk_{eq} + k_{eq}^2.\end{aligned}$$

Therefore by identification we have :

$$\text{Const.} = A(t), \qquad k_{eq}(x,t) = \frac{B}{2A}, \qquad C(x,t) = -Ak_{eq}^2 = -\frac{B^2}{4A}. \tag{B.12}$$

We have now a Gaussian integral with complex coefficients, therefore we can rewrite Eq. (B.11) as:

$$\begin{aligned}
\psi(x,t) &= \left((2\pi)^{3/2}\Delta k\right)^{-1/2} e^{-k_0^2/4\Delta k^2} e^{-C(x,t)} \int_{-\infty}^{+\infty} \exp\left(-A(t)k^2 + B(x)k + C(x,t)\right) dk \\
&= \left((2\pi)^{3/2}\Delta k\right)^{-1/2} \times e^{-k_0^2/4\Delta k^2} \times e^{-C(x,t)} \int_{-\infty}^{+\infty} \exp\left(-A(t)(k - k_{eq}(x,t))^2\right) dk \\
&= \left((2\pi)^{3/2}\Delta k\right)^{-1/2} \times e^{-k_0^2/4\Delta k^2} \times e^{-C(x,t)} \times \sqrt{\frac{\pi}{A(t)}}.
\end{aligned} \tag{B.13}$$

B.3 Harmonization of the mathematical formula

We still need to write this result with a meaningful notation knowing that the probability $P(x,t) = |\psi(x,t)|^2$ is the known propagating Gaussian wavepacket. Therefore we want to write $\psi(x,t) = |\psi(x,t)| \times e^{i\phi}$. For that let's first write $C(x,t)$ as $C_{Re}(x,t) + iC_{Im}(x,t)$ using Eq. (B.12).

$$\begin{aligned}
C(x,t) &= -\frac{B^2}{4A} \\
&= -\left(\frac{k_0 + i2x\Delta k^2}{2\Delta k^2}\right)^2 \times \frac{1}{4} \frac{4m\Delta k^2}{m + i2\hbar t\Delta k^2} \\
&= -\frac{k_0^2 - 4x^2\Delta k^4 + i4xk_0\Delta k^2}{4\Delta k^2} \times \frac{m}{m + i2\hbar t\Delta k^2} \times \frac{m - i2\hbar t\Delta k^2}{m - i2\hbar t\Delta k^2} \\
&= -\frac{m}{4\Delta k^2} \times \frac{k_0^2 - 4x^2\Delta k^4 + i4xk_0\Delta k^2}{m + i2\hbar t\Delta k^2} \times \frac{m - i2\hbar t\Delta k^2}{m - i2\hbar t\Delta k^2} \\
&= -\frac{m}{4\Delta k^2(m^2 + 4(\hbar t)^2\Delta k^4)} \times \left(k_0^2 - 4x^2\Delta k^4 + i4xk_0\Delta k^2\right)\left(m - i2\hbar t\Delta k^2\right),
\end{aligned}$$

we can now separate the real and imaginary terms,

$$\begin{aligned}
&= -\frac{m}{4\Delta k^2\left(m^2 + 4(\hbar t)^2\Delta k^4\right)} \\
&\times \left(mk_0^2 - 4mx^2\Delta k^4 + 8(\hbar t)xk_0\Delta k^4 + i\left[4mxk_0\Delta k^2 - 2(\hbar t)\Delta k^2(k_0^2 - 4x^2\Delta k^4)\right]\right).
\end{aligned} \tag{B.14}$$

Therefore we can write:

$$C_{Re}(x,t) = -\frac{m}{4\Delta k^2\left(m^2+4(\hbar t)^2\Delta k^4\right)} \times \left(mk_0^2 - 4mx^2\Delta k^4 + 8(\hbar t)xk_0\Delta k^4\right)$$
$$= -\frac{m^2k_0^2}{4\Delta k^2\left(m^2+4(\hbar t)^2\Delta k^4\right)} - \frac{\cancel{4}m^2\Delta k^{\cancel{4}}}{\cancel{4\Delta k^2}\left(m^2+4(\hbar t)^2\Delta k^4\right)} \times \left(-x^2 + \frac{2(\hbar t)xk_0}{m}\right), \tag{B.15}$$

and:

$$C_{Im}(x,t) = -\frac{m}{\cancel{4\Delta k^2}\left(m^2+4(\hbar t)^2\Delta k^4\right)} \times \left[4mxk_0\cancel{\Delta k^2} - 2(\hbar t)\cancel{\Delta k^2}(k_0^2 - 4x^2\Delta k^4)\right]. \tag{B.16}$$

B.3.1 The wavepacket norm

Let's now focus on $C_{Re}(x,t)$, since we want to see a meaningful equation of $P(x,t)$, we know that $e^{-C_{Re}(x,t)}$ must be written into the form of a Gaussian. Therefore we should write $C_{Re}(x,t) = \text{Const.} + \left(\frac{x-x_0(t)}{\sigma(t)}\right)^2$, for that we will complete the square in (B.15).

$$C_{Re}(x,t) = \frac{-m^2k_0^2}{4\Delta k^2\left(m^2+4(\hbar t)^2\Delta k^4\right)} - \frac{m^2\Delta k^2}{\left(m^2+4(\hbar t)^2\Delta k^4\right)} \times \left(-x^2 + \frac{2(\hbar t)xk_0}{m}\right).$$

To facilitate the calculation let's write the first fraction as Frac.

$$= \text{Frac.} + \frac{m^2\Delta k^2}{\left(m^2+4(\hbar t)^2\Delta k^4\right)} \times \left(+x^2 - \frac{2(\hbar t)xk_0}{m} + \left[\frac{(\hbar t)k_0}{m}\right]^2 - \left[\frac{(\hbar t)k_0}{m}\right]^2\right)$$
$$= \text{Frac.} - \frac{\cancel{m^2}\Delta k^2 \times (\hbar t)^2k_0^2}{\cancel{m^2}\left(m^2+(\hbar t)^2\Delta k^4\right)} + \frac{m^2\Delta k^2}{\left(m^2+4(\hbar t)^2\Delta k^4\right)}\left(x - \frac{\hbar k_0}{m}t\right)^2. \tag{B.17}$$

Let's now focus on wrinting in a same fraction Frac. and the second fraction with blue:

$$\frac{-m^2k_0^2}{4\Delta k^2\left(m^2+4(\hbar t)^2\Delta k^4\right)} - \frac{(\hbar t)^2k_0^2\Delta k^2}{\left(m^2+(\hbar t)^2\Delta k^4\right)} \times \frac{4\Delta k^2}{4\Delta k^2}$$
$$= \frac{-m^2k_0^2 - 4\Delta k^4(\hbar t)^2k_0^2}{4\Delta k^2\left(m^2+4(\hbar t)^2\Delta k^4\right)}$$
$$= \frac{-k_0^2\cancel{(m^2+4(\hbar t)^2\Delta k^4)}}{4\Delta k^2\cancel{(m^2+4(\hbar t)^2\Delta k^4)}} = \frac{-k_0^2}{4\Delta k^2}, \tag{B.18}$$

We can now introduce Eq. (B.18) in Eq. (B.17) and obtain:

$$C_{Re}(x,t) = \frac{-k_0^2}{4\Delta k^2} + \frac{m^2\Delta k^2}{\left(m^2+4(\hbar t)^2\Delta k^4\right)}\left(x - \frac{\hbar k_0}{m}t\right)^2. \tag{B.19}$$

Let us define:

$$\boxed{\Delta x(t) = \frac{\sqrt{m^2 + 4(\hbar t)^2 \Delta k^4}}{2m\Delta k}}. \tag{B.20}$$

Therefore by substituting $C_{Re}(x,t)$ from Eq. (B.18) in Eq. (B.13) and using $\Delta x(t)$ we can write $|\psi(x,t)|$ as:

$$\begin{aligned} |\psi(x,t)| &= \left((2\pi)^{3/2}\Delta k\right)^{-1/2} e^{-k_0^2/4\Delta k^2} e^{-C_{Re}(x,t)} \sqrt{\frac{\pi}{|A(t)|}} \\ &= \left((2\pi)^{3/2}\Delta k\right)^{-1/2} \cancel{e^{-k_0^2/4\Delta k^2} e^{+k_0^2/4\Delta k^2}} \sqrt{\frac{\pi}{|A|}} \times \exp\left(-\left(\frac{x - v_g t}{2\Delta x(t)}\right)^2\right), \end{aligned} \tag{B.21}$$

with,

$$v_g = \frac{\partial \omega}{\partial k}|_{k=k_0} = \frac{\hbar k_0}{m}, \tag{B.22}$$

and $\Delta x(t)$ such as for $t \geq 0$ we have $\Delta x(t)\Delta k \geq \frac{1}{2}$ in agreement with Heisenberg's incertitude principle.

Now we will calculate $|A(t)|$:

$$\begin{aligned} |A(t)| &= \left|\frac{m + i2\hbar t\Delta k^2}{4m\Delta k^2}\right| \\ &= \frac{\sqrt{m^2 + 4(\hbar t)^2\Delta k^4}}{4m\Delta k^2} \\ &= \frac{\cancel{2}\Delta x(t)}{\cancel{4}\Delta k} \\ |A| &= \frac{\Delta x(t)}{2\Delta k}. \end{aligned} \tag{B.23}$$

So we can write Eq. (B.21) using $|A(t)|$ as:

$$\begin{aligned} |\psi(x,t)| &= \left((2\pi)^{3/2}\cancel{\Delta k}\right)^{-1/2} \left(\frac{\pi \cancel{2}\cancel{\Delta k}}{\Delta x(t)}\right)^{1/2} \times \exp\left(-\left(\frac{x - v_g t}{2\Delta x(t)}\right)^2\right) \\ &= \left(\frac{\cancel{2\pi}}{\cancel{2\pi} \times \sqrt{2\pi}\Delta x(t)}\right)^{1/2} \times \exp\left(\frac{-(x - v_g t)^2}{4\Delta x(t)^2}\right) \\ &= \left(\sqrt{2\pi}\Delta x(t)\right)^{-1/2} \exp\left(\frac{-(x - v_g t)^2}{4\Delta x(t)^2}\right). \end{aligned} \tag{B.24}$$

We now have a meaningful equation of $|\psi(x,t)|$ where we can the probability $P(x,t) = |\psi(x,t)|$ of an atom in a free space as a Gaussian wavepacket moving with a speed v_g and spreading through time according to the standard deviation $\Delta x(t)$.

Let's however check that the normalization criteria is still verified:

$$\int_{-\infty}^{+\infty} |\psi(x,t)|^2 \, dx = \left(\frac{1}{\sqrt{2\pi}\Delta x(t)}\right) \times \int_{-\infty}^{+\infty} \exp\left(\frac{-\cancel{2}(x - v_g t)^2}{\cancel{4}\Delta x(t)^2}\right) dx.$$

Terefore by using the gaussian integral B.7:

$$= \left(\frac{1}{\sqrt{2\pi}\Delta x(t)}\right) \times \sqrt{\pi 2\Delta x(t)^2} = 1. \tag{B.25}$$

The normalization criteria is then verified.

B.3.2 The wavepacket phase

For the phase we want to write $\psi(x,t) = |\psi(x,t)|e^{i\theta(x,t)}$ where $e^{i\theta(x,t)} = e^{-iC_{Im}(x,t)} \times \left(e^{i\theta_A(t)}\right)^{-1/2}$. With $e^{i\theta_A(t)}$ the phase of $A(t)$ such as:

$$\theta_A(t) = \cos^{-1}\left(\frac{\mathrm{Re}(A(t))}{|A(t)|}\right) = \cos^{-1}\left(\frac{2\Delta k}{\Delta x(t)}\frac{1}{4\Delta k^2}\right) = \cos^{-1}\left(\frac{1}{2\Delta x(t)\Delta k}\right). \tag{B.26}$$

Let's now rewrite $C_{Im}(x,t)$ from Eq. (B.16):

$$\begin{aligned} C_{Im}(x,t) &= -\frac{m}{4\cancel{\Delta k^2}\,(m^2 + 4(\hbar t)^2\Delta k^4)} \\ &\times \left[4mxk_0\cancel{\Delta k^2} - 2(\hbar t)\cancel{\Delta k^2}(k_0^2 \times \frac{4m}{4m} - 4x^2\Delta k^4 \times \frac{m}{m})\right] \\ &= -\frac{\cancel{4}m^2}{\cancel{4}\,(m^2 + 4(\hbar t)^2\Delta k^4)} \times \left[xk_0 - \frac{\cancel{2}\hbar k_0^2}{\cancel{4}m}t + \frac{2x^2\Delta k^4\hbar t}{m}\right]. \end{aligned}$$

We define $\omega_0 = \omega(k = k_0) = \hbar k_0^2/2m$ such as:

$$= -\frac{m^2}{(m^2 + 4(\hbar t)^2\Delta k^4)} \times \left[(k_0 x - \omega_0 t) + \frac{2(x\Delta k^2)^2\hbar t}{m}\right],$$

by using Eq. (B.20) we can rewrite the factor as:

$$= -\frac{1}{(2\Delta x(t)\Delta k)^2} \times \left[(k_0 x - \omega_0 t) + \frac{2(x\Delta k^2)^2\hbar t}{m}\right]. \tag{B.27}$$

Therefore:

$$\theta(x,t) = \frac{1}{(2\Delta x(t)\Delta k)^2} \times \left[(k_0 x - \omega_0 t) + \frac{2(x\Delta k^2)^2\hbar t}{m}\right] - \frac{1}{2}\cos^{-1}\left(\frac{1}{2\Delta x(t)\Delta k}\right). \tag{B.28}$$

Let's finally write:

$$\begin{aligned} \psi(x,t) &= \left(\sqrt{2\pi}\Delta x(t)\right)^{-1/2} \exp\left(\frac{-(x - v_g t)^2}{4\Delta x(t)^2}\right) \\ &\times \exp\left[\frac{i}{(2\Delta x(t)\Delta k)^2} \times \left[(k_0 x - \omega_0 t) + \frac{2(x\Delta k^2)^2\hbar t}{m}\right] - \frac{i}{2}\cos^{-1}\left(\frac{1}{2\Delta x(t)\Delta k}\right)\right]. \end{aligned} \tag{B.29}$$

We can also write:

$$\psi(x,t) = \left(\sqrt{2\pi}\Delta x(t)\right) \exp\left[-\frac{(x-v_0t)^2}{4\Delta x(t)^2}\right] \times \exp\left[i\frac{k_0x-\omega_0t}{(2\Delta x(t)\Delta k)^2} + i\frac{v_\Delta t}{\Delta x(0)}\frac{x^2}{4\Delta x(t)^2} - \frac{i}{2}\cos^{-1}\left(\frac{1}{2\Delta x(t)\Delta k}\right)\right]. \tag{B.30}$$

Using $v_\Delta = (\hbar\Delta k)/m$ such that $\Delta x(t)^2 = \Delta x(0)^2 + (v_\Delta t)^2$ and $x^2 = (x-v_0t)^2 + 2xv_0t - v_0^2t^2$ we have:

$$\begin{aligned}
\psi(x,t) =& \left(\sqrt{2\pi}\Delta x(t)\right)^{-1/2} \exp\left[-\frac{(x-v_0t)^2}{4\Delta x(t)^2}\right] \\
&\times \exp\left[i\frac{k_0x-\omega_0t}{(2\Delta x(t)\Delta k)^2} + i\left(2xv_0t - v_0^2t^2\right)\frac{v_\Delta t}{4\Delta x(t)^2\Delta x(0)}\right] \\
&\times \exp\left[i\frac{v_\Delta t}{\Delta x(0)}\frac{(x-v_0t)^2}{4\Delta x(t)^2} - \frac{i}{2}\cos^{-1}\left(\frac{1}{2\Delta x(t)\Delta k}\right)\right] \qquad \text{(B.31)} \\
=& \left(\sqrt{2\pi}\Delta x(t)\right)^{-1/2} \exp\left[-\frac{(x-v_0t)^2}{4\Delta x(t)^2}\right] \\
&\times \exp\left[i\frac{k_0x-\omega_0t}{(2\Delta x(t)\Delta k)^2} + i\left(2x\frac{\hbar k_0}{m}t - \left[\frac{\hbar k_0}{m}\right]^2t^2\right)\frac{v_\Delta t}{4\Delta x(t)^2\Delta x(0)}\right] \\
&\times \exp\left[i\frac{v_\Delta t}{\Delta x(0)}\frac{(x-v_0t)^2}{4\Delta x(t)^2} - \frac{i}{2}\cos^{-1}\left(\frac{1}{2\Delta x(t)\Delta k}\right)\right] \qquad \text{(B.32)} \\
=& \left(\sqrt{2\pi}\Delta x(t)\right)^{-1/2} \exp\left[-\frac{(x-v_0t)^2}{4\Delta x(t)^2}\right] \\
&\times \exp\left[i(k_0x-\omega_0t)\left(\frac{1}{(2\Delta x(t)\Delta k)^2} + \frac{2\hbar t}{m}\frac{v_\Delta t}{4\Delta x(t)^2\Delta x(0)}\right)\right] \\
&\times \exp\left[i\frac{v_\Delta t}{\Delta x(0)}\frac{(x-v_0t)^2}{4\Delta x(t)^2} - \frac{i}{2}\cos^{-1}\left(\frac{1}{2\Delta x(t)\Delta k}\right)\right] \qquad \text{(B.33)}
\end{aligned}$$

$$\boxed{\psi(x,t) = \left(\sqrt{2\pi}\Delta x(t)\right)^{-1/2} \exp\left[-\frac{(x-v_0t)^2}{4\Delta x(t)^2}\right]} \boxed{\times \exp[i(k_0x-\omega_0t)]} \boxed{\times \exp\left[i\frac{v_\Delta t}{\Delta x(0)}\frac{(x-v_0t)^2}{4\Delta x(t)^2} - \frac{i}{2}\cos^{-1}\left(\frac{1}{2\Delta x(t)\Delta k}\right)\right]}. \tag{B.34}$$

B.3.3 Expected values of $\hat{x}$ and $\hat{p}$

The way $\psi(x,t)$ is presented in Eq. (B.29) is not usual, however the momentum should be conserved as there is no potential in the Shrödinger Eq. (B.2). Therefore

we need several checks. We have already checked the normalization of $\psi(x,t)$ in Eq. (B.25). But an other quick check we can do is for example if $t=0$, then we have:

$$\Delta x(t=0) = \frac{1}{2\Delta k},$$

Therefore we have the known result :

$$\psi(x,t=0) = \left(\frac{\sqrt{2\pi}}{2\Delta k}\right)^{-1/2} \exp\left(-(x\Delta k)^2\right) \exp[ik_0 x] \tag{B.35}$$

Let's also note that $\psi(x,t)$, as it is, is only one possible solution of the Schrödinger Eq. (B.2). Here we are only interested in the solutions of a form of a moving Gaussian, this is why we choose $\phi(k)$ as it is in Eq. (B.9).

Let us now talk about the expected values. For the expected value $\langle\hat{x}\rangle$, this is trivial:

$$\begin{aligned}\langle\hat{x}\rangle &= \int x|\psi(x,t)|^2\,\mathrm{d}x \\ &= \int (\mu+v_g t)|\psi(\mu+v_g t,t)|^2\,\mathrm{d}\mu\Big|_{\mu=x-v_g t} \\ \boxed{\langle\hat{x}\rangle = v_g t}&.\end{aligned} \tag{B.36}$$

If we look at Eq. (B.9) then the expected value of $\hat{p}$ is: $\langle\hat{p}\rangle = \hbar k_0 = p_0$. Let us test that on $\psi(x,t)$ from Eq. (B.29).

$$\begin{aligned}\langle\hat{p}\rangle &= \langle\psi|\,\hat{p}\,|\psi\rangle \\ &= -i\hbar\left\langle\psi\middle|\frac{\partial\psi}{\partial x}\right\rangle \\ &= -i\hbar\int\psi(x,t)^*\frac{\partial\psi}{\partial x}\,\mathrm{d}x \\ &= -i\hbar\int\psi(x,t)^*\times\psi(x,t)\left[\frac{-2(x-v_g t)}{2\times 2\Delta x(t)^2}+\frac{ik_0}{(2\Delta x(t)\Delta k)^2}+\frac{i4x\Delta k^4\hbar t}{m(2\Delta x(t)\Delta k)^2}\right]\mathrm{d}x\,,\end{aligned}$$

knowing that $\psi^*\psi = |\psi|^2$ and using Eq. (B.24), we have:

$$\begin{aligned}\langle\hat{p}\rangle = &-i\hbar\int\frac{-(x-v_g t)}{2\Delta x(t)^2}|\psi(x,t)|^2\,\mathrm{d}x \\ &-i\hbar\int\frac{ik_0}{(2\Delta x(t)\Delta k)^2}|\psi(x,t)|^2\,\mathrm{d}x \\ &-i\hbar\frac{i4\hbar t\Delta k^4}{4m\Delta x(t)^2\Delta k^2}\int(\mu+v_g t)|\psi(\mu+v_g t,t)|^2\,\mathrm{d}\mu\Big|_{\mu=x-v_g t} \\ = &-i\hbar\left[0+\frac{ik_0}{(2\Delta x(t)\Delta k)^2}+\frac{i4\hbar t\Delta k^4 v_g t}{4m\Delta x(t)^2\Delta k^2}\right].\end{aligned} \tag{B.37}$$

We have $v_g = \frac{\hbar k_0}{m}$ therefore we have:

$$\begin{aligned}\langle \hat{p} \rangle &= -i\hbar \left[\frac{ik_0}{\left(2\Delta x(t)\Delta k\right)^2} + \frac{i4\hbar t \Delta k^4 \hbar k_0 t}{4m^2 \Delta x(t)^2 \Delta k^2} \right] \\ &= (+1) \times \hbar k_0 \left[\frac{1}{4\Delta x(t)^2 \Delta k^2} \times \frac{m^2}{m^2} + \frac{4(\hbar t)^2 \Delta k^4}{4m^2 \Delta x(t)^2 \Delta k^2} \right], \end{aligned} \tag{B.38}$$

from Eq. (B.20) we have $\Delta x(t)^2 = \frac{m^2 + 4(\hbar t)^2 \Delta k^4}{4m^2 \Delta k^2}$ therefore we have:

$$\langle \hat{p} \rangle = \hbar k_0 \left[\frac{m^2 + 4(\hbar t)^2 \Delta k^4}{4m^2 \Delta k^2} \times \frac{4m^2 \Delta k^2}{m^2 + 4(\hbar t)^2 \Delta k^4} \right]$$

$$\boxed{\langle \hat{p} \rangle = \hbar k_0 = p_0}. \tag{B.39}$$

Therefore our $\psi(x,t)$ verify the momentum conservation.

We have to take into account here that in all our calculation the initial wave-packet is centred in $x = 0$. Therefore by changing our referential origin i.e. substituting x by $x - x_0$ in Eq. (B.29) we would have $\langle \hat{x} \rangle = x_0 + v_g t$.

Appendix C

Pressure measurement using the MOT loading

The loading dynamic of a MOT (Magneto-Optical Trap) is critically dependent of the background pressure of the trapped species and other gases. Indeed the loading rate of atoms in the trap is dependent of the trapped species pressure, while the maximum number of atoms in the trap is related to the general background pressure[100, 101]. We can therefore use a MOT, more precisely a MOT loading, as a reliable pressure sensor as long as the pressure is constant during the time of the MOT loading.

C.1 The fluorescence imaging system

The atom number N_{at} in the MOT is measured through the MOT fluorescence light converted as a voltage signal on a photodiode. The photodiode converts the photon counts (which is itself proportional to N_{at}) to an electrical current acquired as a voltage signal U_{MOT}.

The fluorescence imaging system used in the Observatoire's experiment is discussed in detail in reference [38] and can be seen in Fig. C.2. In this experimental setup, the collection efficiency η of the fluorescence light is estimated to be $\eta = 0.012$, with the reflection of the MOT through the atomchip's mirror and the shadow of the MOT coil (see Fig. C.2) being taken into account. While the response in voltage

U_{pd} of the photodiode to an optical power $\mathcal{P}$ is given by:

$$U_{\text{pd}} = \rho_R \mathcal{P}, \tag{C.1}$$

with $\rho_R \simeq 6 \times 10^5$ V/W. Moreover, the photon scattering rate r_{sc} of the MOT is

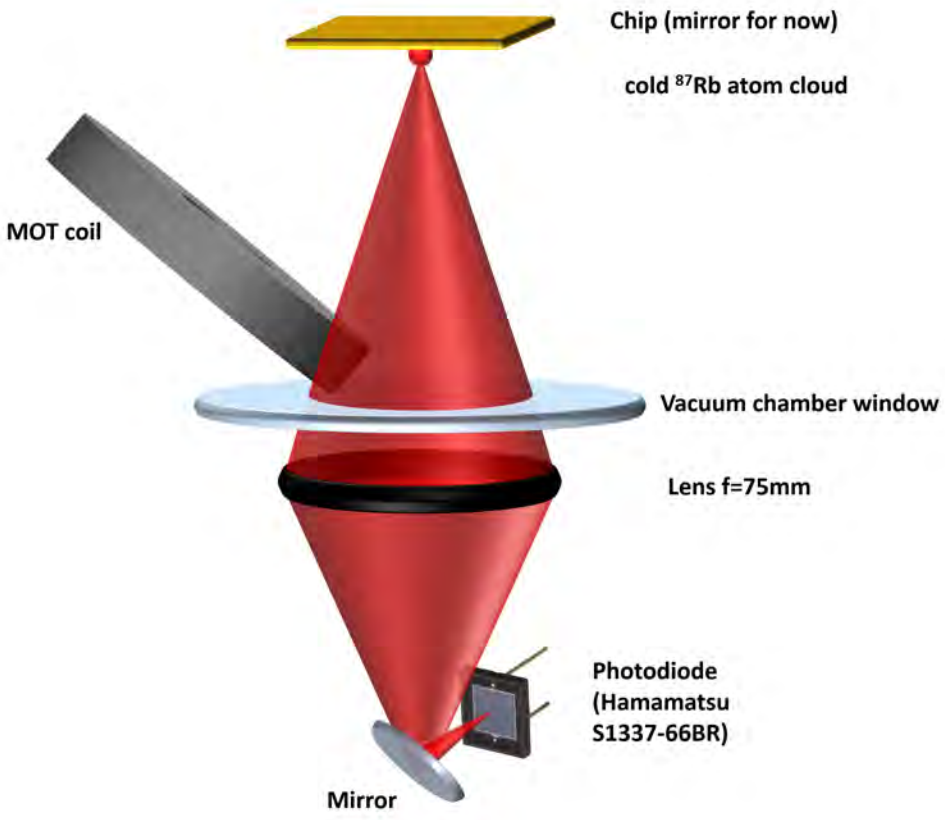

Figure C.1: Experimental setup for the fluorescence imaging system taken from reference [38]. We can see that one of the MOT coil, present in the vacuum chamber, is on the path of the fluorescence light and need to be taken into account.

given as[40]

$$r_{\text{sc}} = \frac{1}{2} \frac{\Gamma s}{1 + s + 4\frac{\delta^2}{\Gamma}}, \tag{C.2}$$

with, Γ the natural line width (of the ^{87}Rb D_2 optical transition), δ is the laser detunning and $s = I/I_{\text{sat}}$, where I is the MOT's laser intensity and I_{sat} the saturation intensity.

We can then write the relation between N_{at} and V_{MOT} given as[38]:

$$N_{\text{at}} = \frac{U_{\text{MOT}} \lambda}{hc\rho_R \eta r_{\text{sc}}}, \tag{C.3}$$

with λ the wavelength of the ^{87}Rb D_2 optical transition, h the Planck's constant and c the speed of light.

C.2 The measurement

For the measurement we switch ON a the dispenser (with a constant current) while monitoring the ion pump current I_m and the photodiode voltage U_{pd}. The monitoring of I_m allow us know the evolution in the vacuum chamber as I_m is used by the ion pump to measure pressure, therefore, when the pressure stabilise we switch ON the MOT lasers. However, independently from the MOT fluorescence U_{MOT}, the photodiode measure the signal the stray light from the MOT lasers U_{sl}. Therefore, as you can see in Fig. C.2, we acquire the photodiode voltage U_{pd} for two cases. One case (red curve in Fig. C.2) where we switch ON the MOT lasers without switching ON the MOT's magnetic field, therefore, there is no MOT, such that $U_{\text{pd}} = U_{\text{sl}}$. In the other case (black curve in Fig. C.2) where we switch ON the MOT lasers then we switch ON the MOT's magnetic field, such that there is a MOT and $U_{\text{pd}} = U_{\text{sl}} + U_{\text{MOT}}$. We can then extract U_{MOT} by subtracting the red curve to the black curve in Fig. C.2.

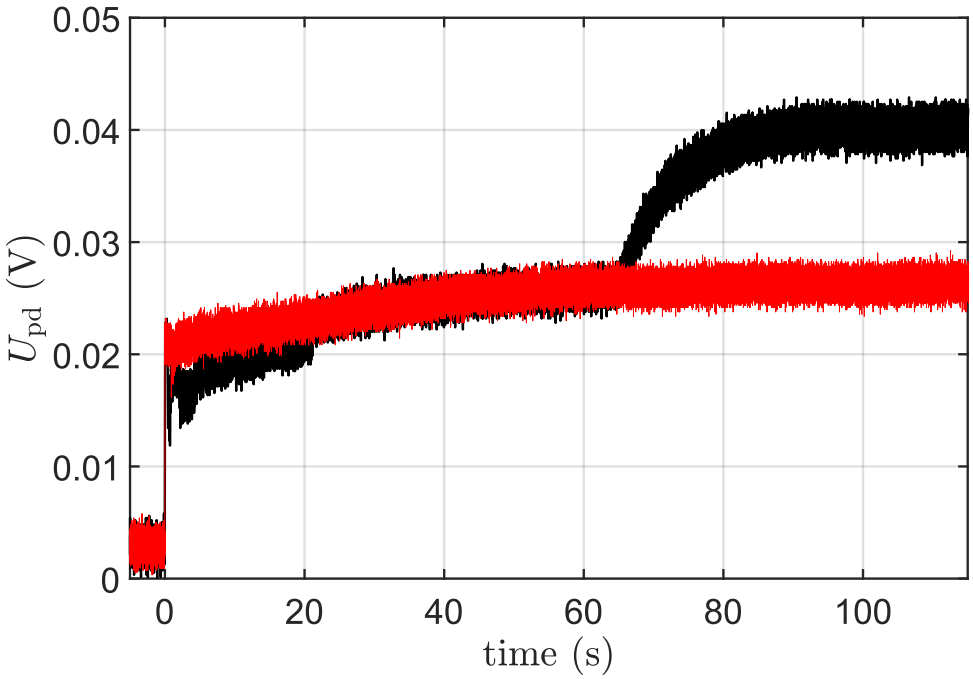

Figure C.2: Photodiode voltage from a fluorescence measurement. The dispenser is switched ON with a constant current of 4.75 A until pressure stabilise, then the MOT lasers are switched ON at 0 s. In red, measurement of the fluorescence without switching ON the MOT's magnetic field. In black, the MOT's magnetic field is switched ON at 65 s.

C.3 Data treatment

After extracting U_{MOT} from the difference of the black and red curve in Fig. C.2, we can apply Eq. (C.3) in order to extract the number of atoms in the MOT. However, the dynamics of a MOT loading are determined by the background pressure as follow [100, 101]

$$N_{\mathrm{at}} = \frac{r_{\mathrm{at}}}{\gamma}(1 - \exp(-\gamma t)), \tag{C.4}$$

where r_{at} is rate at which atoms are trapped in the MOT and γ the loss rate due to collisions with background gases. Both r_{at} and γ are pressure dependent, however, r_{at} also depends of the trap parameters while γ is only pressure dependent. Therefore, by fitting the MOT loading (as you can see in Fig. C.3), we can know the pressure P_1 in the science chamber of the MOT through the following relation[100] (with γ expressed in s^{-1}):

$$P_1 = \frac{1.33322 \times \gamma}{4.4 \times 10^7}. \tag{C.5}$$

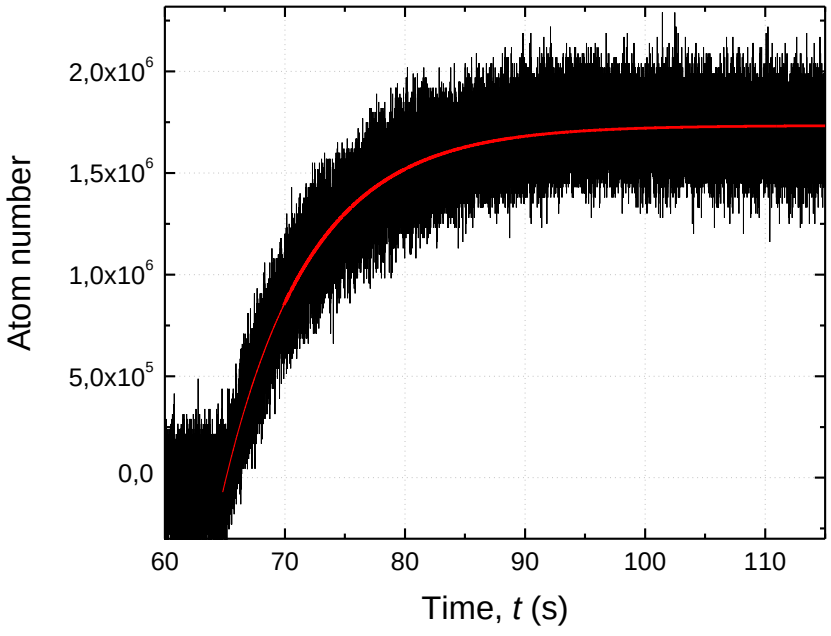

Figure C.3: Number of ^{87}Rb atoms loaded in the MOT (black) for a dispenser current of 4.75 A. The fit (red solid line) to the experimental data gives a characteristic loading time $(1/\gamma)$ of 7.13 ± 0.02 s.

Bibliography

[1] A. G. J. MacFarlane, J. P. Dowling, and G. J. Milburn, "Quantum technology: the second quantum revolution," *Philosophical Transactions of the Royal Society of London. Series A: Mathematical, Physical and Engineering Sciences*, vol. 361, no. 1809, pp. 1655–1674, 2003. 1

[2] A. De Touzalin, C. Marcus, F. Heijman, I. Cirac, R. Murray, and T. Calarco, "Quantum manifesto. a new era of technology," *European Comission*, 2016. 1

[3] C. L. Degen, F. Reinhard, and P. Cappellaro, "Quantum sensing," *Reviews of modern physics*, vol. 89, p. 035002, July 2017. 1

[4] *The Anschutz Gyro-Compass and Gyroscope Engineering.* Wexford College Press, 2003. 1

[5] D. Holleville, *conception et réalisation d'un gyromètre à atomes froids fondé sur l'effet Sagnac pour les ondes de matière.* Theses, Université Paris Sud - Paris XI, Sept. 2001. 2

[6] V. Apostolyuk and F. Tay, "Dynamics of micromechanical coriolis vibratory gyroscopes," *Sensor Letters*, vol. 2, pp. 252–259, 09 2004. 2

[7] E. J. POST, "Sagnac effect," *Rev. Mod. Phys.*, vol. 39, pp. 475–493, Apr 1967. 2

[8] H. C. Lefèvre, "The fiber-optic gyroscope, a century after sagnac's experiment: The ultimate rotation-sensing technology?," *Comptes Rendus Physique*, vol. 15, no. 10, pp. 851 – 858, 2014. The Sagnac effect: 100 years later / L'effet Sagnac : 100 ans après. 2

[9] O. Carnal and J. Mlynek, "Young's double-slit experiment with atoms: A simple atom interferometer," *Phys. Rev. Lett.*, vol. 66, pp. 2689–2692, May 1991. 2

[10] D. W. Keith, C. R. Ekstrom, Q. A. Turchette, and D. E. Pritchard, "An interferometer for atoms," *Phys. Rev. Lett.*, vol. 66, pp. 2693–2696, May 1991. 2

[11] M. Kasevich and S. Chu, "Atomic interferometry using stimulated raman transitions," *Phys. Rev. Lett.*, vol. 67, pp. 181–184, Jul 1991. 2

[12] F. Riehle, T. Kisters, A. Witte, J. Helmcke, and C. J. Bordé, "Optical ramsey spectroscopy in a rotating frame: Sagnac effect in a matter-wave interferometer," *Phys. Rev. Lett.*, vol. 67, pp. 177–180, Jul 1991. 2

[13] B. Barrett, R. Geiger, I. Dutta, M. Meunier, B. Canuel, A. Gauguet, P. Bouyer, and A. Landragin, "The sagnac effect: 20 years of development in matter-wave interferometry," *Comptes Rendus Physique*, vol. 15, no. 10, pp. 875 – 883, 2014. The Sagnac effect: 100 years later / L'effet Sagnac : 100 ans après. 2, 3

[14] D. Savoie, M. Altorio, B. Fang, L. A. Sidorenkov, R. Geiger, and A. Landragin, "Interleaved atom interferometry for high-sensitivity inertial measurements," *Science Advances*, vol. 4, no. 12, 2018. 3, 4

[15] B. Culshaw, "The optical fibre sagnac interferometer: an overview of its principles and applications," *Measurement Science and Technology*, vol. 17, pp. R1–R16, nov 2005. 4

[16] J. A. Sauer, M. D. Barrett, and M. S. Chapman, "Storage ring for neutral atoms," *Phys. Rev. Lett.*, vol. 87, p. 270401, Dec 2001. 4

[17] S. Gupta, K. W. Murch, K. L. Moore, T. P. Purdy, and D. M. Stamper-Kurn, "Bose-einstein condensation in a circular waveguide," *Phys. Rev. Lett.*, vol. 95, p. 143201, Sep 2005. 4, 8

[18] A. S. Arnold, C. S. Garvie, and E. Riis, "Large magnetic storage ring for bose-einstein condensates," *Phys. Rev. A*, vol. 73, p. 041606, Apr 2006. 4

[19] K. Henderson, C. Ryu, C. MacCormick, and M. G. Boshier, "Experimental demonstration of painting arbitrary and dynamic potentials for bose–einstein condensates," *New Journal of Physics*, vol. 11, p. 043030, apr 2009. 4

[20] N. R. Cooper and Z. Hadzibabic, "Measuring the superfluid fraction of an ultracold atomic gas," *Phys. Rev. Lett.*, vol. 104, p. 030401, Jan 2010. 4

[21] A. Turpin, J. Polo, Y. V. Loiko, J. Küber, F. Schmaltz, T. K. Kalkandjiev, V. Ahufinger, G. Birkl, and J. Mompart, "Blue-detuned optical ring trap for bose-einstein condensates based on conical refraction," *Opt. Express*, vol. 23, pp. 1638–1650, Jan 2015. 4

[22] T. A. Bell, J. A. P. Glidden, L. Humbert, M. W. J. Bromley, S. A. Haine, M. J. Davis, T. W. Neely, M. A. Baker, and H. Rubinsztein-Dunlop, "Bose–einstein condensation in large time-averaged optical ring potentials," *New Journal of Physics*, vol. 18, p. 035003, mar 2016. 4, 8, 28, 29, 38, 39

[23] O. Morizot, Y. Colombe, V. Lorent, H. Perrin, and B. M. Garraway, "Ring trap for ultracold atoms," *Phys. Rev. A*, vol. 74, p. 023617, Aug 2006. 4

[24] M. Gildemeister, E. Nugent, B. E. Sherlock, M. Kubasik, B. T. Sheard, and C. J. Foot, "Trapping ultracold atoms in a time-averaged adiabatic potential," *Phys. Rev. A*, vol. 81, p. 031402, Mar 2010. 4

[25] G. A. Sinuco-León, K. A. Burrows, A. S. Arnold, and B. M. Garraway, "Inductively guided circuits for ultracold dressed atoms," *Nature Communications*, vol. 5, p. 5289, Oct. 2014. 4

[26] P. Navez, S. Pandey, H. Mas, K. Poulios, T. Fernholz, and W. von Klitzing, "Matter-wave interferometers using TAAP rings," *New Journal of Physics*, vol. 18, p. 075014, jul 2016. 4, 28

[27] B. M. Garraway and H. Perrin, "Recent developments in trapping and manipulation of atoms with adiabatic potentials," *Journal of Physics B: Atomic, Molecular and Optical Physics*, vol. 49, p. 172001, aug 2016. 4

[28] S. Pandey, H. Mas, G. Drougakis, P. Thekkeppatt, V. Bolpasi, G. Vasilakis, K. Poulios, and W. von Klitzing, "Hypersonic bose-einstein condensates in accelerator rings," *Nature*, vol. 570, pp. 205–209, June 2019. 4, 8

[29] J. Reichel, W. Hänsel, and T. W. Hänsch, "Atomic micromanipulation with magnetic surface traps," *Phys. Rev. Lett.*, vol. 83, pp. 3398–3401, Oct 1999. 5

[30] M. Keil, O. Amit, S. Zhou, D. Groswasser, Y. Japha, and R. Folman, "Fifteen years of cold matter on the atom chip: promise, realizations, and prospects," *Journal of Modern Optics*, vol. 63, no. 18, pp. 1840–1885, 2016. PMID: 27499585. 5

[31] E. R. Elliott, M. C. Krutzik, J. R. Williams, R. J. Thompson, and D. C. Aveline, "Nasa's cold atom lab (cal): system development and ground test status," *npj Microgravity*, vol. 4, p. 16, Aug. 2018. 5

[32] T. Schuldt, C. Schubert, M. Krutzik, L. G. Bote, N. Gaaloul, J. Hartwig, H. Ahlers, W. Herr, K. Posso-Trujillo, J. Rudolph, S. Seidel, T. Wendrich, W. Ertmer, S. Herrmann, A. Kubelka-Lange, A. Milke, B. Rievers, E. Rocco, A. Hinton, K. Bongs, M. Oswald, M. Franz, M. Hauth, A. Peters, A. Bawamia, A. Wicht, B. Battelier, A. Bertoldi, P. Bouyer, A. Landragin, D. Massonnet, T. Lévèque, A. Wenzlawski, O. Hellmig, P. Windpassinger, K. Sengstock, W. von Klitzing, C. Chaloner, D. Summers, P. Ireland, I. Mateos, C. F. Sopuerta, F. Sorrentino, G. M. Tino, M. Williams, C. Trenkel, D. Gerardi, M. Chwalla, J. Burkhardt, U. Johann, A. Heske, E. Wille, M. Gehler, L. Cacciapuoti, N. Gürlebeck, C. Braxmaier, and E. Rasel, "Design of a dual species atom interferometer for space," *Experimental Astronomy*, vol. 39, pp. 167–206, June 2015. 5

[33] S. Wu, E. Su, and M. Prentiss, "Demonstration of an area-enclosing guided-atom interferometer for rotation sensing," *Phys. Rev. Lett.*, vol. 99, p. 173201, Oct 2007. 5, 48

[34] S. Jöllenbeck, J. Mahnke, R. Randoll, W. Ertmer, J. Arlt, and C. Klempt, "Hexapole-compensated magneto-optical trap on a mesoscopic atom chip," *Phys. Rev. A*, vol. 83, p. 043406, Apr 2011. 5

[35] C. L. G. Alzar, W. Yan, and A. Landragin, "Towards high sensitivity rotation sensing using an atom chip," in *Research in Optical Sciences*, p. JT2A.10, Optical Society of America, 2012. 5, 51

[36] W. Yan, *Design of a magnetic guide for rotation sensing by on chip atom interferometry*. PhD thesis, 2014. Thèse de doctorat dirigée par Garrido Alzar, Carlos et Landragin, Arnaud Physique Paris 6 2014. 5, 6

[37] J.-B. Trebbia, C. L. Garrido Alzar, R. Cornelussen, C. I. Westbrook, and I. Bouchoule, "Roughness suppression via rapid current modulation on an atom chip," *Phys. Rev. Lett.*, vol. 98, p. 263201, Jun 2007. 6, 78, 79

[38] S. Bade, *Propagation of atoms in a magnetic waveguide on a chip*. PhD thesis, 2016. Thèse de doctorat dirigée par Garrido Alzar, Carlos et Landragin, Arnaud Physique Paris 6 2016. 7, 8, 48, 135, 136

[39] J.-M. Martin, S. Bade, W. Dubosclard, M. A. Khan, S. Kim, B. M. Garraway, and C. L. G. Alzar, "Pumping dynamics of cold-atom experiments in a single vacuum chamber," *Phys. Rev. Applied*, vol. 12, p. 014033, Jul 2019. 7

[40] D. Steck, "Rubidium 87 d line data," 01 2003. 10, 12, 38, 136

[41] B. M. Garraway and K. A. Suominen, "Wave-packet dynamics: new physics and chemistry in femto-time," *Reports on Progress in Physics*, vol. 58, pp. 365–419, apr 1995. 13

[42] J. D. Pritchard, A. N. Dinkelaker, A. S. Arnold, P. F. Griffin, and E. Riis, "Demonstration of an inductively coupled ring trap for cold atoms," *New Journal of Physics*, vol. 14, p. 103047, oct 2012. 28

[43] A. Chakraborty, S. R. Mishra, S. P. Ram, S. K. Tiwari, and H. S. Rawat, "A toroidal trap for cold ${}ˆ{87}{rb}$ atoms using an rf-dressed quadrupole trap," *Journal of Physics B: Atomic, Molecular and Optical Physics*, vol. 49, p. 075304, mar 2016. 29

[44] A. Chakraborty, S. R. Mishra, S. P. Ram, S. K. Tiwari, and H. S. Rawat, "A study on evolution of a cold atom cloud in a time dependent radio frequency dressed potential," 2016. 29

[45] D. M. Giltner, R. W. McGowan, and S. A. Lee, "Atom interferometer based on bragg scattering from standing light waves," *Phys. Rev. Lett.*, vol. 75, pp. 2638–2641, Oct 1995. 48

[46] E. Giese, A. Roura, G. Tackmann, E. M. Rasel, and W. P. Schleich, "Double bragg diffraction: A tool for atom optics," *Phys. Rev. A*, vol. 88, p. 053608, Nov 2013. 48

[47] C. I. Sukenik, M. G. Boshier, D. Cho, V. Sandoghdar, and E. A. Hinds, "Measurement of the casimir-polder force," *Phys. Rev. Lett.*, vol. 70, pp. 560–563, Feb 1993. 51

[48] Y.-j. Lin, I. Teper, C. Chin, and V. Vuletić, "Impact of the casimir-polder potential and johnson noise on bose-einstein condensate stability near surfaces," *Phys. Rev. Lett.*, vol. 92, p. 050404, Feb 2004. 51

[49] J. Reichel, *Trapping and Manipulating Atoms on Chips*, ch. 2, pp. 33–60. John Wiley & Sons, Ltd, 2011. 51, 52, 54, 79

[50] J. Armijo, C. L. Garrido Alzar, and I. Bouchoule, "Thermal properties of aln-based atom chips," *European Physical Journal D*, vol. 56, pp. 33–39, Jan. 2010. 52

[51] W. M. Haynes, *CRC Handbook of Chemistry and Physics*. June 2014. 52

[52] M. A. Angadi, T. Watanabe, A. Bodapati, X. Xiao, O. Auciello, J. A. Carlisle, J. A. Eastman, P. Keblinski, P. K. Schelling, and S. R. Phillpot, "Thermal transport and grain boundary conductance in ultrananocrystalline diamond thin films," *Journal of Applied Physics*, vol. 99, no. 11, p. 114301, 2006. 52

[53] A. D. Technologies, "Uncd wafers data sheet & technical knowledge bank," techreport, 2012. 53

[54] H. Yamada, A. Chayahara, Y. Mokuno, N. Tsubouchi, and S. ichi Shikata, "Uniform growth and repeatable fabrication of inch-sized wafers of a single-crystal diamond," *Diamond and Related Materials*, vol. 33, pp. 27 – 31, 2013. 54

[55] M. Muehle, M. Becker, T. Schuelke, and J. Asmussen, "Substrate crystal recovery for homoepitaxial diamond synthesis," *Diamond and Related Materials*, vol. 42, pp. 8 – 14, 2014. 54

[56] I. Satoh, S. Arakawa, K. Tanizaki, M. Miyanaga, T. Sakurada, Y. Yamamoto, and H. Nakahata, "Development of aluminum nitride single-crystal substrates," *SEI Technical Review*, pp. 78–82, 10 2010. 54

[57] R. R. Sumathi, "Bulk aln single crystal growth on foreign substrate and preparation of free-standing native seeds," *CrystEngComm*, vol. 15, pp. 2232–2240, 2013. 54

[58] M. J. Madou, *Manufacturing Techniques for Microfabrication and Nanotechnology*. CRC Press, 2011. 54, 56

[59] J. Estève, C. Aussibal, T. Schumm, C. Figl, D. Mailly, I. Bouchoule, C. I. Westbrook, and A. Aspect, "Role of wire imperfections in micromagnetic traps for atoms," *Phys. Rev. A*, vol. 70, p. 043629, Oct 2004. 54

[60] T. Schumm, J. Estève, C. Figl, J.-B. Trebbia, C. Aussibal, H. Nguyen, D. Mailly, I. Bouchoule, C. I. Westbrook, and A. Aspect, "Atom chips in the real world: the effects of wire corrugation," *European Physical Journal D*, vol. 32, pp. 171–180, Feb. 2005. 54

[61] L. P. Bicelli, B. Bozzini, C. Mele, and L. D'Urzo, "A review of nanostructural aspects of metal electrodeposition," *Int. J. Electrochem. Sci*, vol. 3, no. 4, pp. 356–408, 2008. 59

[62] G. F. McGuire, *Semiconductor Materials and Process Technology Handbook (VLSI and ULSI)*. Noyes Publications, 1989. 59

[63] B. Hammer and J. K. Norskov, "Why gold is the noblest of all the metals," *Nature*, vol. 376, pp. 238–240, July 1995. 60

[64] T. Karabacak and T.-M. Lu, "Enhanced step coverage by oblique angle physical vapor deposition," *Journal of Applied Physics*, vol. 97, no. 12, p. 124504, 2005. 61

[65] J. K. Lan, Y.-L. Wang, C. G. Chao, K.-y. Lo, and Y. L. Cheng, "Effect of substrate on the step coverage of plasma-enhanced chemical-vapor deposited tetraethylorthosilicate films," *Journal of Vacuum Science & Technology B: Microelectronics and Nanometer Structures Processing, Measurement, and Phenomena*, vol. 21, no. 4, pp. 1224–1229, 2003. 61

[66] P. Treutlein, *Coherent manipulation of ultracold atoms on atom chips*. PhD thesis, Ludwig-Maximilians-Universität München, Apr. 2008. 65, 66, 67, 73

[67] R. J. Sewell, J. Dingjan, F. Baumgärtner, I. Llorente-García, S. Eriksson, E. A. Hinds, G. Lewis, P. Srinivasan, Z. Moktadir, C. O. Gollasch, and M. Kraft, "Atom chip for BEC interferometry," *Journal of Physics B: Atomic, Molecular and Optical Physics*, vol. 43, p. 051003, feb 2010. 65, 66

[68] K. Ott, *Towards a squeezing-enhanced atomic clock on a chip*. Theses, Université Pierre et Marie Curie - Paris VI, Sept. 2016. 65, 66, 76

[69] E. Koukharenko, Z. Moktadir, M. Kraft, M. Abdelsalam, D. Bagnall, C. Vale, M. Jones, and E. Hinds, "Microfabrication of gold wires for atom guides," *Sensors and Actuators A: Physical*, vol. 115, no. 2, pp. 600 – 607, 2004. The 17th European Conference on Solid-State Transducers. 66

[70] J. Estève, *From atom mirror to atom waveguide: effects of roughness*. Theses, Université Pierre et Marie Curie - Paris VI, Nov. 2004. 66, 79

[71] T. A. Green, "Gold electrodeposition for microelectronic, optoelectronic and microsystem applications," *Gold Bulletin*, vol. 40, p. 105–114, June 2007. 66

[72] M. E. Z. M. e. a. Kołodziejczyk, K., "Influence of constant magnetic field on electrodeposition of metals, alloys, conductive polymers, and organic reactions," *Journal of Solid State Electrochemistry*, vol. 22, pp. 1629–1647, June 2018. 67, 68

[73] A. Krause, M. Uhlemann, A. Gebert, and L. Schultz, "The effect of magnetic fields on the electrodeposition of cobalt," *Electrochimica Acta*, vol. 49, no. 24, pp. 4127 – 4134, 2004. 68

[74] S. Nekrasov, "Ion transport in electrolyte flux under magnetic field," *Russian Journal of Electrochemistry*, 2013. 68

[75] T. Pasanen, G. von Gastrow, I. Heikkinen, V. Vähänissi, H. Savin, and J. Pearce, "Compatibility of 3-d printed devices in cleanroom environments for semiconductor processing," *Materials Science in Semiconductor Processing*, vol. 89, pp. 59 – 67, 2019. 69

[76] Metakem, "M-gold-sf-bath-e datasheet," tech. rep. 71

[77] MichroChemicals, "Basics of microstructuring," tech. rep. 74

[78] F. Reinhard, *Design and construction of an atomic clock on an atom chip*. Theses, Université Pierre et Marie Curie - Paris VI, Feb. 2009. 78, 80, 90, 91, 93

[79] C. A. G. G. J. Dick, J. D. Prestage and L. Ma, "Local oscillator induced degradation of medium–term stability in passive atomic frequency standards," in *Proceedings of the 22nd Annual Precise Time and TimeInterval (PTTI) Applications and Planning Meeting* (V. . R. L. Sydnor (NASA, Hampton, ed.), pp. 487–508, 1990. 97

[80] G. Santarelli, C. Audoin, A. Makdissi, P. Laurent, G. J. Dick, and A. Clairon, "Frequency stability degradation of an oscillator slaved to a periodically interrogated atomic resonator," *IEEE Transactions on Ultrasonics, Ferroelectrics, and Frequency Control*, vol. 45, pp. 887–894, July 1998. 97

[81] A. Quessada, R. P. Kovacich, I. ne Courtillot, A. Clairon, G. Santarelli, and P. Lemonde, "The dick effect for an optical frequency standard," *Journal of Optics B: Quantum and Semiclassical Optics*, vol. 5, pp. S150–S154, apr 2003. 97

[82] M. Schioppo, R. C. Brown, W. F. McGrew, N. Hinkley, R. J. Fasano, K. Beloy, T. H. Yoon, G. Milani, D. Nicolodi, J. A. Sherman, N. B. Phillips, C. W. Oates, and A. D. Ludlow, "Ultrastable optical clock with two cold-atom ensembles," *nature photonics*, vol. 11, pp. 48–52, Jan. 2017. 97

[83] C. Monroe, W. Swann, H. Robinson, and C. Wieman, "Very cold trapped atoms in a vapor cell," *Phys. Rev. Lett.*, vol. 65, pp. 1571–1574, Sep 1990. 97, 106

[84] J. E. Bjorkholm, "Collision-limited lifetimes of atom traps," *Phys. Rev. A*, vol. 38, pp. 1599–1600, Aug 1988. 97

[85] V. Dugrain, P. Rosenbusch, and J. Reichel, "Alkali vapor pressure modulation on the 100 ms scale in a single-cell vacuum system for cold atom experiments," *Review of Scientific Instruments*, vol. 85, no. 8, p. 083112, 2014. 98, 106

[86] S. Kang, K. R. Moore, J. P. McGilligan, R. Mott, A. Mis, C. Roper, E. A. Donley, and J. Kitching, "Magneto-optic trap using a reversible, solid-state alkali-metal source," *Opt. Lett.*, vol. 44, pp. 3002–3005, Jun 2019. 98

[87] L. Torralbo-Campo, G. D. Bruce, G. Smirne, and D. Cassettari, "Light-induced atomic desorption in a compact system for ultracold atoms," *Scientific Reports*, vol. 5, p. 14729, Oct. 2015. 98

[88] J. Grosse, S. T. Seidel, D. Becker, M. D. Lachmann, M. Scharringhausen, C. Braxmaier, and E. M. Rasel, "Design and qualification of an uhv system for operation on sounding rockets," *Journal of Vacuum Science & Technology A*, vol. 34, no. 3, p. 031606, 2016. 98

[89] D. R. Scherer, D. B. Fenner, and J. M. Hensley, "Characterization of alkali metal dispensers and non-evaporable getter pumps in ultrahigh vacuum systems for cold atomic sensors," *Journal of Vacuum Science & Technology A*, vol. 30, no. 6, p. 061602, 2012. 98

[90] A. Basu and L. F. Velásquez-García, "An electrostatic ion pump with nanostructured si field emission electron source and ti particle collectors for supporting an ultra-high vacuum in miniaturized atom interferometry systems," *Journal of Micromechanics and Microengineering*, vol. 26, p. 124003, sep 2016. 98, 99, 116

[91] M. Audi and M. de Simon, "Ion pumps," *Vacuum*, vol. 37, no. 8, pp. 629 – 636, 1987. Special Issue Modern Vacuum Practice. 98, 111, 113

[92] G. Coppa, A. D'Angola, and R. Mulas, "Analysis of electron dynamics in non-ideal penning traps," *Physics of Plasmas*, vol. 19, no. 6, p. 062507, 2012. 98

[93] Y. Suetsugu, "Numerical calculation of an ion pumpś pumping speed," *Vacuum*, vol. 46, no. 2, pp. 105 – 111, 1995. 99

[94] W. Ho, R. K. Wang, T. P. Keng, and K. H. Hu, "Calculation of sputtering ion pump speed," *Journal of Vacuum Science and Technology*, vol. 20, no. 4, pp. 1010–1013, 1982. 99

[95] P. Chiggiato, "Vacuum Technology for Ion Sources," p. 40 p, Apr 2014. Comments: 40 pages, contribution to the CAS-CERN Accelerator School: Ion Sources, Senec, Slovakia, 29 May - 8 June 2012, edited by R. Bailey, CERN-2013-007. 99, 101, 103, 105

[96] R. Kersevan and J.-L. Pons, "Introduction to molflow+: New graphical processing unit-based monte carlo code for simulating molecular flows and for calculating angular coefficients in the compute unified device architecture environment," *Journal of Vacuum Science & Technology A*, vol. 27, no. 4, pp. 1017–1023, 2009. 101, 116

[97] G. Vacuum, "Ion pump titan^{tm} 45s-cv technical bulletin 00.003.971," tech. rep. 102, 103, 105

[98] D. J. Santeler, "Exit loss in viscous tube flow," *Journal of Vacuum Science & Technology A*, vol. 4, no. 3, pp. 348–352, 1986. 105

[99] R. L. Summers, "Empirical observations on the sensitivity of hot cathode ionization type vacuum gages," tech. rep., NASA Technical Note D-5285 (1969). 105

[100] T. Arpornthip, C. A. Sackett, and K. J. Hughes, "Vacuum-pressure measurement using a magneto-optical trap," *Phys. Rev. A*, vol. 85, p. 033420, Mar 2012. 106, 135, 138

[101] R. W. G. Moore, L. A. Lee, E. A. Findlay, L. Torralbo-Campo, G. D. Bruce, and D. Cassettari, "Measurement of vacuum pressure with a magneto-optical

trap: A pressure-rise method," *Review of Scientific Instruments*, vol. 86, no. 9, p. 093108, 2015. 106, 109, 135, 138

[102] A. Dallos and F. Steinrisser, "Pumping speeds of getter-ion pumps at low pressures," *Journal of Vacuum Science and Technology*, vol. 4, no. 1, pp. 6–9, 1967. 112

[103] M. Rose, J. Bartha, and I. Endler, "Temperature dependence of the sticking coefficient in atomic layer deposition," *Applied Surface Science*, vol. 256, no. 12, pp. 3778 – 3782, 2010. 113